Low-Cost Time-Domain UWB Radar System: Analysis of Electrical Components

Douglas Wesley Kendall

Department of Electrical & Computer Engineering
McGill University
Montreal, Canada

November 2020

A thesis submitted to McGill University in partial fulfillment of the requirements for the degree of Master of Science.

2020/11/13

Abstract

Early detection of breast cancer is vital for improved survival rates. X-ray mammography is the conventional imaging approach to screen for breast cancer. While shown to be effective at reducing breast-cancer mortality, mammography exposes the patient to ionizing radiation, requires uncomfortable breast compression, and has poor sensitivity in dense tissue. Studies of breast tissue have noted dielectric contrast between malignant and benign tissue in the microwave range, leading to investigation of microwave-based screening and diagnosis systems. These microwave systems promise to be lower in cost and non-invasive.

The current system developed by McGill University operates by transmitting a narrow pulse into the tissue and measuring the response. It relies on the use of expensive lab equipment to generate and measure the pulses. This thesis studies the electrical instrumentation, with the aim of reducing both cost and form factor. Commercially available electronic components with standard printed circuit board manufacturing are investigated toward this goal.

Three components of the system are evaluated: (i) the microwave pulse generator, (ii) the time-domain receiver, and (iii) the switching and antenna matrix. First, a number of pulse generator circuits are measured and new discrete designs are presented. This is followed by a literature review of time-domain receivers, concluding with recommendations for low-cost designs. Finally, system integration and testing of a flexible multi-layer circuit board are presented. These contributions are a step towards the cost-reduction needed to make microwave systems an attractive screening tool.

Sommaire

Pour améliorer les résultats pour les patientes, la détection précoce du cancer du sein est vitale. La mammographie aux rayons X est l'approche d'imagerie conventionnelle pour dépister le cancer du sein. Bien qu'elle se soit avérée efficace pour réduire la mortalité par cancer du sein, la mammographie expose la patiente aux rayonnements ionisants, nécessite une compression mammaire inconfortable, a une faible sensibilité dans les tissus denses et a un coût élevé à implémenter et à opérer. Des études sur les tissus mammaires ont noté un contraste entre les tissus malins et bénins dans la gamme des micro-ondes, conduisant à une étude des systèmes de dépistage et de diagnostic basés sur les micro-ondes. Ces systèmes micro-ondes ont potentiellement un coût moindre et un mode de détection moins invasif.

Le système actuel fonctionne en mesurant la reponse d'une impulsion étroite transmise dans le tissu mammaire.. Il repose sur l'utilisation d'un équipement de laboratoire coûteux pour générer et mesurer ces impulses. Cette thèse étudie l'instrumentation électrique dans le but de réduire à la fois le coût et le facteur de forme. Dans ce but, des composants électroniques disponibles dans le commerce avec une fabrication standard de circuit imprimé sont étudiés.

Trois composantes du système sont évaluées: (i) le générateur d'impulsions micro-ondes, (ii) le récepteur du domaine temporel, et (iii) la matrice de commutation d'antennes. Tout d'abord, un certain nombre de circuits générateurs d'impulsions sont mesurés et de nouvelles conceptions discrètes sont présentées. Ceci est suivi d'une revue de la littérature des récepteurs du domaine temporel, concluant avec des recommandations pour des conceptions à faible coût. Enfin, le test et l'intégration dans le system d'une carte de circuit ayant multiple couches flexibles est présenté. Ces contributions sont une étape vers la réduction des coûts nécessaire pour faire des systèmes à micro-ondes un outil de dépistage attrayant.

Acknowledgments

Foremost I would like to thank my supervisor, Dr. Milica Popović. She has been very accommodating of my research interests and career goals, while giving me encouragement and constructive feedback throughout. She has helped me expand my abilities as a researcher and engineer. I have had an excellent experience under her guidance at McGill University.

I would also like to thank other the professors and researchers who have provided insight and guidance on the way. Dr. Joshua Schwartz has laid groundwork and provided a great opportunity for me to develop hardware for the project. Dr. Mark Coates has provided a wealth of insight to myself and the group on the data analysis portions of the project.

Ms. Lena Kranold (PhD Candidate) has helped me immensely in my endeavors by introducing me to the system, answering questions, and providing advice and mentorship. Mr. Leonardo Fortaleza has been great source of conversation and insight on hardware development. I would like to thank my other peers from the Breast Cancer Detection research group for creating a welcoming environment. It has been a pleasure working with such a great group of people.

Contents

List of Figures

List of Tables

List of Acronyms

ADC	Analog-to-Digital Converter
BJT	Bipolar Junction Transistor
CMOS	Complementary Metal-Oxide-Semiconductor
COTS	Commercial Off-the-Shelf
DMAS	Delay-Multiply-And-Sum
ETS	Equivalent-Time Sampling
FET	Field-Effect Transistor
FWHM	Full Width at Half-Maximum
GSPS	Gigasamples Per Second
LNA	Low-Noise Amplifier
MIC	Microwave Integrated Circuit
MMIC	Monolithic Microwave Integrated Circuit
MSPS	Megasamples Per Second
NF	Noise Figure
NLTL	Non-linear Transmission Line
PLL	Phase-Locked Loop
S&H	Sample-and-Hold
SNR	Signal-to-Noise Ratio

SRD	Step Recovery Diode
TDR	Time-domain Radar
THA	Track-and-Hold Amplifier
UWB	Ultra-Wideband
VNA	Vector-network Analyzer

Chapter 1

Introduction

1.1 Motivation

Breast cancer is a prevalent cancer among women. Early detection is vital, as it can drastically reduce the chance of mortality. For such reasons, screening programs are used to facilitate detection. Existing imaging and detection modalities have various drawbacks in terms of cost and ability to detect malignancy. Microwave imaging has been proposed as a way of complementing existing diagnosis and screening techniques. It offers a number of improvements, such as the lack of ionizing radiation and the absence of breast compression improving patient comfort. It may also offer lower costs. In order to make microwave approaches a viable option, a low-cost implementation of the electrical components is needed.

Breast cancer is the second most common cancer in women. In the United States in particular, it is expected that 279,100 new cases will occur in 2020, and 42,690 deaths as a result [13]. Rates of breast cancer have increased as the life expectancy of women has increased. This is because with age, the risk of developing cancer grows, with women 60 years or older at highest risk.

Like with most cancers, detecting the malignancy early offers possibility of treatment before the cancer has metastasized, and reduces the risk of mortality [13]. For this reason, researchers target methods of detection that can determine if a growth is malignant at an early stage. The gold standard of early detection technology is mammography [14]. Mammography has been shown effective to reduce deaths due to breast cancer when applied in a screening environment, but presents a number of drawbacks. These include the use of ionizing radiation, pain caused by breast compression, and a lack of sensitivity in dense tissue.

Microwave imaging has been proposed as an alternative imaging and detection modality for breast cancer detection. Studies of dielectric permittivity of malignant and non-malignant breast tissue has indicated a contrast suitable for detecting cancerous tissues [15]. Microwave frequencies offer a unique view of tissues, and have been proposed as a complementary screening and detection technology. One current drawback is the need for high-frequency instrumentation, which is often expensive.

There are generally two modes of acquiring high-frequency measurements from antenna arrays targeting breast tissues: frequency-domain and time-domain measurement. Frequency-domain measurements can be made reliably using a vector-network analyzer (VNA). It is common to convert acquired frequency domain VNA data to the time-domain to facilitate beamforming algorithms. The second approach is to measure directly in the time-domain, in a modality commonly known as time-domain radar (TDR). Currently, both approaches require expensive components. The goal of this work is to develop a time-domain radar system which is low-cost, using widely available components and accessible manufacturing.

Implementing time-domain radar poses a number of challenges. As frequencies increase to the GHz range and beyond, low-frequency design techniques and components are no longer applicable, and components must be designed as distributed microwave integrated circuits

(MICs). Circuit layout presents parasitics; this degrades speed, introduces cross-talk, reflections, RF interference, and attenuation. To reach similar performance to commercially available hardware, hybrid MICs, realized with commonly available components using standard PCB fabrication are proposed and tested.

1.2 Thesis Contributions

This thesis presents contributions towards implementing a low-cost time-domain radar system suitable for manufacturing on standard PCBs with emphasis on the pulse generator, and time-domain receiver subsystem. In each domain, a review of high-frequency circuit elements, circuit topologies, and manufacturing is presented. Additionally, evaluation of a flexible integrated switching matrix prototype is presented. The main contributions are as follows:

- A review of ultra-wideband pulse generators that can be implemented using low-cost components, and supporting measurements;
- A review of time-domain receiver implementations and components which offer an order of magnitude reduction in costs;
- Measurements and experimental results of a flexible antenna array prototype.

1.3 Thesis Outline

Chapter 2 presents the background information on the project, and on development of ultra-wideband time-domain radar. The mechanism of breast cancer detection using microwave frequencies is presented, as well as the current state of microwave breast cancer detection systems. The mathematics and realization of time-domain radar in the microwave frequency range is presented. Microwave design and manufacturing are discussed.

Chapter 3 discusses ultra-wideband pulse generators in the context of a low-cost breast-cancer detection system. The required performance is addressed, and a review of potential solutions is presented, as well as the components and manufacturing details, with emphasis on cost and performance. Measurements with currently available ultra-wideband circuits are presented. Simulations of proposed designs and future testing are proposed.

Chapter 4 discusses ultra-wideband time-domain receivers for low-cost breast cancer detection. Relevant components needed for receiving such as delay-lines, PLLs, sampling mechanisms, and passive microwave devices are discussed. Several topologies are analyzed and proposed.

Chapter 5 presents evaluation of a flexible switching matrix with embedded antennas. The circuit is tested in simple tumor detection scenarios. The work demonstrates successful isolation of a tumor response signal. Further testing with the flexible circuit demonstrates inability to form images using beamforming, due to poor signal integrity.

Chapter 6 concludes the thesis. Circuits to evaluate and test to reduce system cost of the breast-cancer detection prototype are reiterated. Future work and research directions are suggested.

1.4 Contributors

The flexible antenna array prototype under evaluation was designed and manufactured by students Conner Hahn and Sam Studebaker with supervision by Dr. Josh Schwartz. Conner Hahn, Sam Studebaker, and Dr. Joshua Schwartz are associated with Trinity University in San Antonio, Texas, USA. Dr. Joshua Schwartz is also an adjunct professor at McGill

University in Montreal, Quebec, Canada. This thesis presents only system-level evaluation, with credit for the design and manufacturing given to the above individuals. The original flexible board concept was developed by Dr. Adam Santorelli and alumni in [16], also under supervision of Dr. Joshua Schwartz.

Chapter 2

Background

In this chapter, we first describe where microwave-based detection systems fit into the problem of screening for breast cancer. What follows is a description of our clinical time-domain system, the components currently needed to implement the system, and our current data analysis methods. Finally, the manufacturing technology required and available to implement an UWB system, able to transmit and receive in the time-domain, is discussed.

2.1 Breast Cancer and Screening

Breast cancer is a disease characterized by the formation of cancerous lesions in breast tissues. The most common breast cancer is invasive ductal carcinoma, and invasive lobular carcinoma, representing 70-80% and 10-20% of all cases, respectively [13]. As with most cancers, the mortality rates are lower if the cancer is detected early. To facilitate early detection, screening programs have been implemented in many countries, typically using mammography, followed by biopsies and other follow-up examinations.

Mammography is the dominant modality used to screen for breast cancer on a large scale.

It uses X-ray radiation on compressed breast tissue to fine variation in contrast which may be due to a cancerous lesion. Mammography can lead to false-positives, as non-cancerous glands, calcifications, and other objects can appear as tumors as they attenuate the X-rays. A biopsy is typically required to classify the results of a mammography. This biopsy may also prove inconclusive. In addition to the inconclusive nature of mammography, patients often find the procedure uncomfortable. It can also be expensive to implement screening programs, limiting access in remote areas and low-income areas. Because of the cost and risk of false-positives, screening will not always lead to better outcomes across the population [17]. The foremost factor is the age range and risk of the group being screened. Only females over 40 have a high enough risk of breast cancer to justify regular screening. As the patients become older, surgical intervention becomes risky, and may cause a decreased quality of life even if the cancer is successfully detected and treated. For this reason, screening programs have been under scrutiny and health researchers have been actively searching for more accurate cost-effective approaches to breast-cancer detection.

In the absence of screening programs, breast cancer is investigated on a per patient basis by general practitioners in clinics. Patients with a family history or showing indicators will have a physical exam and/or mammogram. This may be followed by a biopsy. An ultrasound or MRI may be used for additional follow-up. Biomarkers have also been investigated in combination with the above imaging techniques. Diagnosis of breast cancer currently is a challenge, and combining multiple approaches can be enormously beneficial. In this clinical domain, a new imaging technique, such a microwave detection, may also be applicable to reduce false positives and improve the outcome for the patient.

2.2 UWB Radar Breast Cancer Detection

Considering the limitations in the current state-of-the-art breast cancer screening and diagnosis, microwave-based breast cancer imaging systems have been proposed. These systems offer a unique detection and imaging modality based on tissue dielectric properties in the microwave range (1 and 100 GHz). This information, combined with existing detection techniques, promises to complement current clinical screening and diagnosis procedures at a low cost.

Studies of dielectric properties (relative permittivity, ϵ_r, and conductivity, σ in S/m) in breast tissue across the microwave frequency range have indicated a discernible difference between malignant tissue and adipose tissue [15]. Understanding dielectric properties of breast tissue and surrounding tissue is still actively researched. An MRI-derived reconstruction of the dielectric properties of breast tissue is shown in Fig. 2.1. This profile demonstrates that glandular tissues and cancerous lesions have a high relative dielectric contrast, ϵ_r, of 40.0 or more compared to the fat tissues which have an approximate relative dielectric of 8.0.

The dynamics of tissue imaging is a challenge. The tissue properties vary within a patient over time with the menstrual cycle. The breast is a heterogeneous structures with varying density, which makes the assumptions for imaging and detection unreliable. There is further variation between patients, and variation depending on the type of cancerous lesion. Furthermore, glandular structures and benign lesions can present a variation in dielectric properties similar to a cancerous lesion, which leads to false-positives.

This difference in dielectric properties has motivated a variety of breast-cancer detection systems. By measuring the tissue properties in the microwave range, researchers try to determine if malignancy is present. Some systems are designed to detect reflections caused by dielectric boundaries, while others attempt to reconstruct the entire dielectric profile.

This emerging technology aims to offer a complementary view into the tissues that may support or refute diagnosis. If demonstrated to detect small tumors through clinical testing, this modality would make a promising, low-cost screening tool.

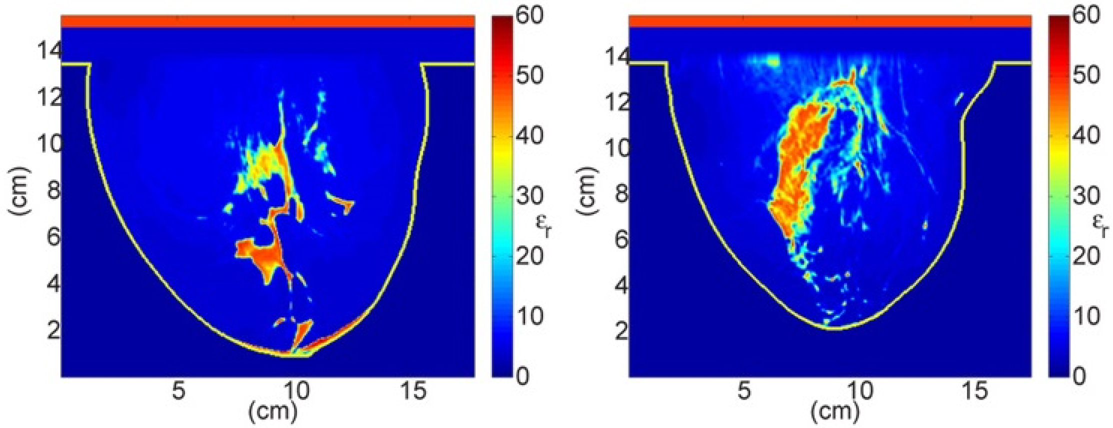

Fig. 2.1 Two MRI-derived dielectric profiles for two healthy patients, adapted from [1].

2.3 UWB Radar

Ultra-wideband (UWB) systems have been actively investigated for the purposes of telecommunication, object and position tracking, as well medical imaging. UWB development history stems from military applications [18]. An UWB system refers to any system using information spread over at least a 500 MHz bandwidth, or more than 20% of the center frequency. In general, the resolution of targets detectable by an UWB system are inversely proportional to the bandwidth of the pulse, which corresponds to the pulse-width in time. Higher frequencies however propagate with more attenuation though lossy materials, and there is a trade-off between range and resolution. System design is a challenge for microwave breast cancer detection as the components are not mass-produced. Detecting variation in dielectric tissue requires reliable high performance electronics, but for microwave imaging envisioned as a mass-screening modality, a low-cost implementation is desirable.

There are many aspects to the design of microwave imaging for breast cancer detection: structural design, antenna design, electrical implementation, and post-processing/analysis. For mechanical design, groups have implemented rotating antennas, direct-contact antennas, antennas matched using dielectric coupling materials (such as ultrasound gel), as well as flexible antenna arrays. Some designs are compact, handheld, or wearable, while others are large, stationary imaging systems. Antenna design depends on the frequencies of operation, how the antenna makes contact, and the desired electromagnetic field patterns. Electrical implementation involves the transmitter, receiver, amplification, timing, and control mechanisms. Algorithms are designed to reconstruct the dielectric properties or determine if there is a tumor present, as well as calibrate and correct for environmental and measurement variations. There are many avenues of improvement for the microwave systems, and this thesis addresses a few components for the system described next.

2.3.1 System Overview

The focus of this thesis is work on a time-domain UWB breast-cancer detection system, developed at McGill University [19]. Comparable breast-cancer detection systems operating in the time-domain have been investigated by many groups [20] [21]. The system consists of a pulse generator, emitting wideband pulses at a certain pulse-repetition rate, transmitting through a switched antenna array, and receiving the response in the time-domain. The generated pulses use a frequency range of 2.0-4.0 GHz, which provides an optimal trade-off between resolution and penetration depth [22].

The current operational system is shown in Fig. 2.6. The system has been shown to successfully image and detect dielectric variation in tissue in phantom experiments. The pulse-generator consists of a Picosecond Pulse Labs Pulse Generator 3600, a microstrip filter with a 2-4 GHz passband, and a Minicircuit ZVE-3W-83+ power amplifier. The pulses when amplified will reach full saturation of the power amplifier, producing pulses of approximately 33dBm, or 12V peak amplitude. The pulses are passed through a 2x16 switching matrix, implemented on a multi-layer high-frequency PCB. The switches drive an array of 16 patch antennas described in [23]. The receiving end of the switching matrix is then acquired directly by a Picoscope 9200A equivalent time sampling oscilloscope. The system is clocked by a Tektronix GigaBERT 1400, which provides a coherent time-base for the pulse generator and the oscilloscope.

The antennas are arranged in direct contact with the tissue. This reduces the reflection caused by external air-to-skin transition. The antenna arrangement used in our system consists of two rings of eight patch antennas, or 16 total, as shown in Fig. 2.2. This arrangement has been shown to provide good coverage of the region and ability to produce high-contrast images in the region of interest [24].

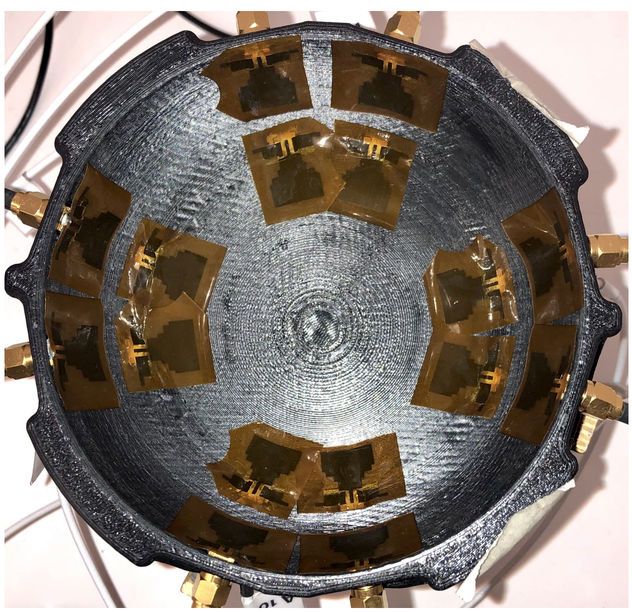

Fig. 2.2 Hemisphere layout used in the clinical system.

The system uses radar-based detection. When an incident pulse encounters a variation in tissue, it will cause reflection and scattering of the wave. The expectation is that a tumor will appear as a variation in dielectric at these frequencies. Therefore, we expect to receive a time-domain waveform consisting of the incident pulse scaled and delayed in time after the signal propagates through the breast. This linear transformation is an approximation of the realistically scattered pulse, but we expect it to be sufficiently accurate for initial experiments. The receiving antenna will also receive many other signals unrelated to the reflections inside the breast. A direct path through fast propagating and low attenuating air produces a strong response which will generally occur early in the received signal with high magnitude. There are also reflections which may occur outside of the breast, such as reflections from the other antennas in the array. To isolate the reflections which occur inside the breast, we must find a way to declutter the signals. A reliable method in phantom experiment is by simply using subtraction with a baseline signal. Decluttering is an ongoing challenge for microwave breast cancer detection. Many channels must be acquired to provide detection coverage of the entire breast tissue, with the current experimental system using 240 total channels.

The time delay of the reflection can be used to localize the dielectric discontinuity, using the speed of propagation and time of flight. This assumes we know the speed of propagation in the tissue which is related to ϵ_r by

$$c = \frac{c_0}{\sqrt{\epsilon_r}} \tag{2.1}$$

where c_0 is the speed of light in free space and c is the speed of light in the medium. This speed will vary between patients with different tissue density. Methods which to relate time-domain signals to spatial representation of waves are called beamforming methods. The simplest method is delay-and-sum beamforming (DAS), which delays the signals to align them spatially to a point of interest, and sums them all in time to produce a beamformed signal. This signal is then measured for total power to get a measure of reflection at that point. We use a variant of the delay-and-sum beamforming, called delay-multiply-and-sum (DMAS), to reconstruct spatial images from the reflected signals [25]. This method adds an additional multiplication step to the signals before summation, which improves contrast. Redundant information, obtained by acquiring more channels, helps to improve the image quality, detection capability, and with decluttering time-domain signals.

Representations of ultra-wideband signals in the frequency and time-domain are presented here. A narrow Gaussian pulse produces a wide, DC-centered bandwidth, as shown in Fig. 2.3. This can be identified from the Fourier transform of a Gaussian function:

$$\mathcal{F}\{e^{-\alpha x^2}\} = \sqrt{\frac{\pi}{\alpha}} \cdot e^{-\frac{(\pi f)^2}{\alpha}} \tag{2.2}$$

where $\alpha = \frac{1}{2\sigma^2}$ is the Gaussian parameter. We can derive a relationship between pulse width and frequency content of pulses, such that the spectrum of pulses can be quickly approximated. The FWHM, w, of a Gaussian is related to the parameter σ by $w = 2.355\sigma$. Using this relation in combination with the Fourier transform identity, the time-domain FWHM w is related to the frequency-domain FWHM W by:

$$W \approx \frac{0.883}{w} \tag{2.3}$$

where W is the FWHM in Hz, and w is the FWHM in seconds. This is illustrated in Fig. 2.3, where a 88 ps impulse produces a frequency-domain FWHM of 10 GHz centered at 0 Hz, and a 3 dB-cutoff at 5 GHz. Pulses generated with a center frequency offset from DC and some bandwidth, appear as sinusoidal envelopes of finite duration, as shown in Fig. 2.4 and Fig. 2.5. As previously mentioned, pulses of this type are used in the current clinical system.

In radar systems, pulses are generated at a certain pulse-repetition rate (PRR), which is repeated at a frequency much lower than the spectral content of the pulse. In the time-domain, this is a convolution of a low-frequency pulse with a narrow pulse. In the frequency-domain, this is a comb with spacing equal to the PRR, multiplied by the frequency response of the pulse. To produce such a pulse train, a sinusoidal or square clock will drive a *pulse generator* which produces the comb spectrum which contains many harmonics beyond its input. For this reason such a circuit is often called a *harmonic multiplier*. These circuits are discussed in more detail in Chapter 3. The frequency-domain spacing produced by harmonic multiplication allows us to compress the spectrum for down-conversion via mixing, which translates in the time-domain to equivalent time sampling. This concept is explored further in Chapter 4. This feature must be utilized in order to receive pulses at a lower frequency than the transmitted signal.

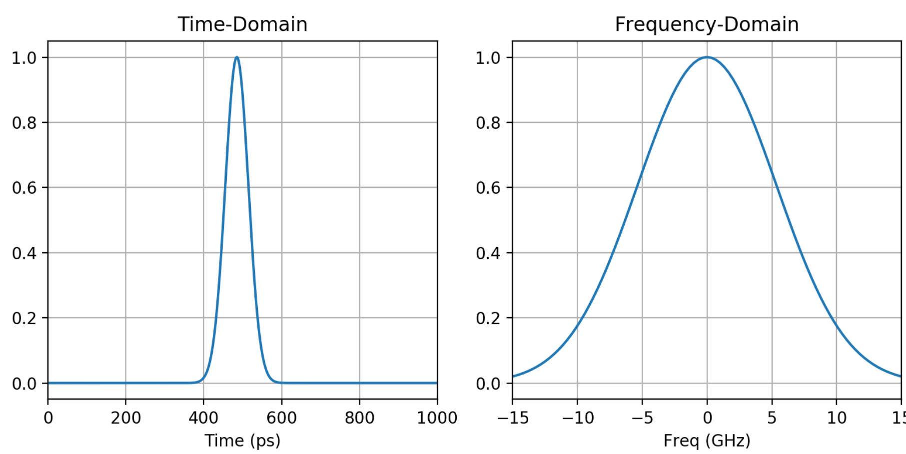

Fig. 2.3 Pulse of width 88 ps in the frequency and time-domain.

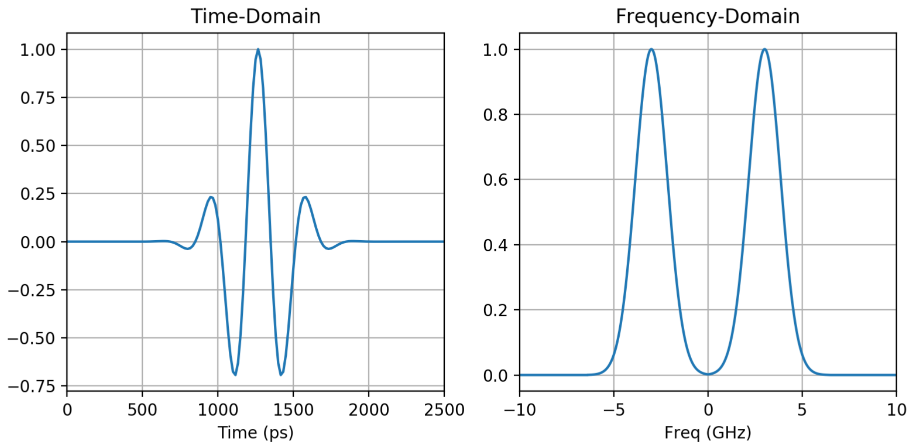

Fig. 2.4 A pulse defined by a 2-4 GHz Gaussian frequency response in the time and frequency-domain.

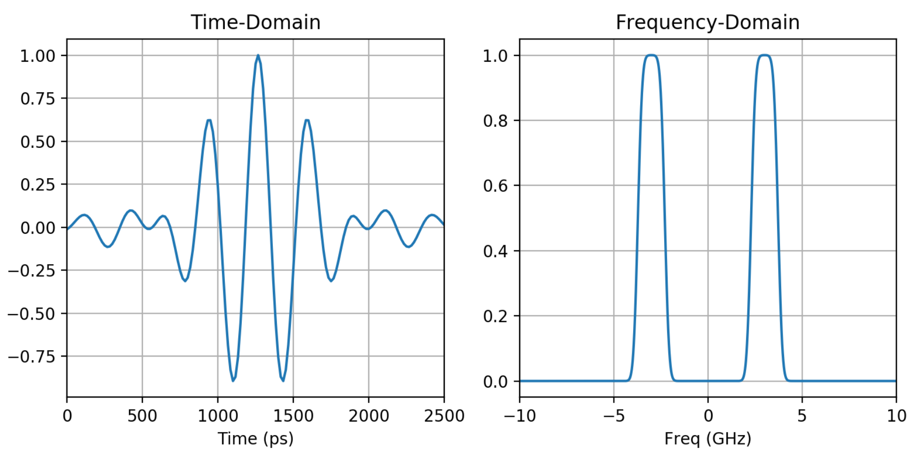

Fig. 2.5 A pulse with a 2-4 GHz Guassian-rectangular frequency response.

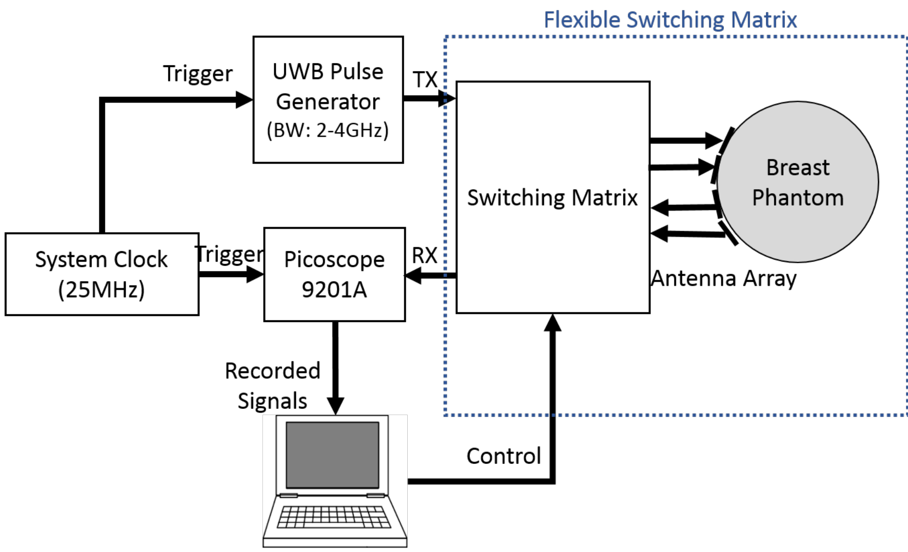

Fig. 2.6 System diagram of current clinical setup.

2.4 System Performance

The goal of this work is to replace and miniaturize the pulse generator, receiver, and the switching circuitry with lower-cost alternatives. First, we must identify the metrics we will use to evaluate the performance of a particular component. In designing an UWB radar system, the key factors affecting detection capability are the bandwidth, phase noise (also known as jitter), signal-to-noise ratio, and dynamic range. We also introduce qualitative and quantitative metrics that can be measured from the fully integrated system; namely, the mean-energy-difference (MED) and DMAS imaging results that can be measured using controlled phantom experiments.

2.4.1 Phase Noise

Phase noise is variation in frequency of a periodic signal. For a sinusoid, any deviation in the frequency-domain appears as a 'skirt' around its fundamental harmonic. Phase noise is measured by the spectral power occurring at some offset from the carrier. This power-spectral density around the fundamental indicates a small finite probability of the signal appearing as a different frequency. Jitter is the same phenomenon as phase noise, but refers to its time-domain representation. Jitter is measured as the probability distribution of the zero-crossings in the time-domain, resulting in an RMS-jitter in seconds.

Phase noise is of particular importance to pulsed radar systems. If there is uncertainty in the acquired signals, this corresponds directly to uncertainty in the position of the reflected target. Furthermore, we can easily find figures of acceptable jitter by considering the required positional accuracy and speed of propagation. Plane waves propagating through tissue with a relative permittivity of 8.0 (fat tissue) have a velocity of $1.0 \cdot 10^8$ m/s. An RMS jitter of 1 ns will introduce an uncertainty of 10 cm RMS. Targets of interest are on the order of 1 mm; which means an acceptable jitter will be approximately 10 ps RMS.

Any phase-locked loop (PLL) or oscillator will have an inherent phase noise. Commercially available clock sources come with a variety of jitter ranges, depending on the application. The clock jitter will represent the absolute minimum jitter in the system, as it drives all other components. Additional jitter can be introduced by any component in the system, through a few different mechanisms. Any additive noise on a periodic signal is converted to phase noise through the mechanism of amplitude-modulation to phase-modulation conversion (AM-PM conversion). This occurs for all passive and active devices where general additive noise can be introduced via loss in the system. Active devices additionally introduce phase noise through mixing of noise content into the fundamental frequency of operation. This can lead to large phase noise being introduced by pulse generator circuits, and this is a key measurement factor in those circuits. Receivers may also introduce phase noise through active mechanisms. It is important to characterize the phase noise in pulse-generating and in receiving circuits.

2.4.2 Bandwidth

The bandwidth of the system is the range of frequencies at which signals can be generated, transmitted, and received. The 3 dB bandwidth (often just called bandwidth with 3 dB implied) is specified as the frequency or range of frequencies, at which the power, gain, or some other parameter drops by 3 dB. Every component in the system (pulse-generators, filters, antenna, transmission lines, and receiver) has a frequency response. The combined frequency response aggregates to an overall frequency-dependent attenuation throughout the system. Our system currently operates using pulses filtered to 2-4 GHz. Because our system is still experimental and frequencies may change and to allow some performance margin, this work aims to achieve at least 6 GHz operation for most components.

Reaching the desired bandwidths of 2-4 GHz is challenging, because of need for specialized active and passive devices to handle high frequencies. Consider first the receiving element. Mass-produced commercially available integrated analog-to-digital converters (ADC) typically operate up to 100 MHz or so, with expensive high-performance ADCs available up to a few GHz. This requires rethinking our design to maintain low costs. Fortunately, reaching frequencies of 6 GHz is attainable using low-cost components by using equivalent time sampling. However, this still requires design of a sampling circuit able to acquire narrow pulses, a fundamentally microwave-oriented design.

2.4.3 Distortion

Distortion refers to non-linear effects in the system, which means they introduces new frequencies into the system. Distortion is measured by compression points (usually 1-dB compression) and the intercept points. The 1-dB compression point is measured by increasing the input signal, until the output signal drops from its linear trajectory by 1 dB. The

2nd order or 3rd order input intercept points (IIP2 and IIP3) are measured by injecting a single frequency or multiple frequencies, and measuring the resulting output frequencies that would be produced by non-linear intermodulation. The point of intercept is determined by projecting where the output signal would have an equal magnitude to these products. Ideally, we want the intercepts points to be very high, meaning that the distortion does not become problematic until the input signal is very large. Unfortunately, these measurements are typically taken in a narrow-band system, and we have to assume the performance will be similar in a wideband scenario. The 1-dB compression point is widely applicable to the selection of amplifiers and receivers in the radar system, as they will only operate effectively below the 1-dB compression point. To expand this measure into wideband systems, the amplitude of the input pulse is used in place of the narrowband input amplitude, which has shown to be a good assumption experimentally. The applicability of the IIP2, and IIP3 measurements to the radar system is less clear, beyond choosing designs with higher values whenever possible.

Overall, it is very undesirable for the pulses generated by the transmitter to experience distortion. It will cause the production of inter-modulation products, and because we are transmitting many frequencies simultaneously, these products will spread rapidly into the full frequency spectrum. These distortion measures are mostly a concern where there is high output swing, which would be the output path of the system. This is accounted for in the design of pulse generators in Chapter 3, by keeping the UWB pulse height inside the linear range of the power amplifier.

2.4.4 Signal-to-Noise Ratio and Noise Figure

Noise figure (NF) and signal-to-noise ratio (SNR) can be used to characterize the receiver and transmitter. Each point in the system has a signal-to-noise ratio, defined as:

$$SNR = \frac{P_{signal}}{P_{noise}} \tag{2.4}$$

where P_{signal} is the power of the signal and P_{noise} power of the noise. The noise factor is a metric that can be applied to a single component, or a series of components in a cascade. It is defined as the ratio of input signal SNR over the output SNR, given by:

$$F = \frac{SNR_{in}}{SNR_{out}} \tag{2.5}$$

The noise figure NF is simply the noise factor expressed in decibels:

$$NF = log_{10}F \tag{2.6}$$

It tells us how much noise is introduced by a block in the system; for example, an amplifier with a noise figure of 10dB will decrease the SNR by 10dB. The noise figure accounts for the gain of an amplifier; a high gain amplifier may have high output noise power, but a relatively low noise figure. An attenuator also has a noise figure equal to its amount of attenuation, where it is assumed the loss affects the signal but not the noise floor. Filters and transmission lines with insertion loss have a noise figure equal to their loss; any loss in the system corresponds to a decrease in SNR and the introduction of noise.

A cascade of stages will have an overall noise figure defined by Friis's formula:

$$F_{total} = F_1 + \frac{F_2 - 1}{G_1} + \frac{F_3 - 1}{G_1 G_2} + ... + \frac{F_n - 1}{G_1 G_2 ... G_{n-1}} \tag{2.7}$$

where F_i and G_i are the noise figure and power gain of the i-th stage of a total of n stages. This equation indicates that early gain stages will decrease noise introduced by subsequent stages. Similarly loss at the input of a cascade increases the noise introduced. For this reason, a low-noise amplifier (LNA) is often used at the beginning of a receiver chain.

If we try to apply this metric to the transmitter, we can only attempt to maximize the SNR at the input to the power amplifier. This is because we are designing around a specified power amplifier with a given saturation point. This amounts to simply designing a pulse generator with low noise at the amplifier saturation point.

The noise figure plays a more important role in the receiver, which is a combination of an LNA and the time-domain receiver. For low-power signals, a LNA may improve overall SNR, while for large signals, it may saturate, or even cause damage to the oscilloscope. This is not thoroughly investigated in this work. In the section on receivers, NF is considered where data from literature is available, however it is rarely available in a way that allows quantitative comparison between receivers.

2.4.5 Measures of Performance using Phantoms

While the previous performance metrics have some utility, we are interested mostly in tumor detection of the complete system. To evaluate the system, carbon rubber phantoms are used [26]. This allows us to test the system with the antennas matched to the medium (breast-tissue), instead of introducing reflections. The decluttering mechanism of choice in the lab is an alignment and subtraction technique. This consists of a baseline acquisition, which contains no target, followed by an acquisition containing an embedded tumor. By aligning and subtracting these, we can isolate a tumor response.

Once the tumor response is isolated, it can be used as a metric of system performance. One option is to simply measure the total energy of the tumor response, defined as the MED metric. This can tell us if a particular channel observes a reflection, assuming the decluttering is effective. It can also tell us the overall efficacy of the scan, system or scenario, for a baseline-tumor experiment. This requires an additional step of aggregating or omitting signals. Another option to measure performance is to use beamforming, and measure how strong the tumor response is, in relationship to the non-tumor portions of the image. Such a measure is called the signal-to-clutter ratio (SCR). Visualization of the images also provides useful qualitative results.

2.4.6 Summary of Metrics

The goal of this work is to replace components in the system, while ensuring the system performance is the same. Towards this goal, meaningful metrics for system components should be reported. Making incremental changes to the system, and evaluating images is often the most meaningful metric of performance. Unfortunately it doesn't tell exactly how the electrical performance relates to the image produced. The image quality is also impacted by many other variables unrelated to electrical performance. For this reason, both imaging as well as electrical measures, such as phase noise, bandwidth, and others, should be reported. In situations where the component or design cannot be integrated, our reporting reduces to the electrical parameters, without supporting imaging results.

2.5 Microwave Integrated Circuits

This section gives an overview of microwave electronics in the context of an ultra-wideband radar system. Because the system must transmit, amplify and process high frequencies, conventional circuit design and fabrication will lead to very unexpected results. The first discrepancy with respect to conventional design originates from the fact that traces are distributed transmission lines rather than simple connections. Without considering this, signals will simply not reach their destination as assumed. In microwave electronics, the circuit's classification as well as performance is based on the fabrication method used for interconnection [27]. Such devices are referred to as *microwave integrated circuits* (MICs). Modern microwave circuits typically consist of planar transmission lines such as microstrips, slot-lines, or coplanar waveguides. Broadly speaking, an MIC can be either *monolithic* or *hybrid*. A monolithic MIC has all active and passive components grown and laid out on a wafer. A hybrid MIC implements transmission lines via etching or printing, with active components soldered or wire-bonded on. With this naming convention, standard low-cost printed-circuit boards (PCB) which implement high-frequency electronics are referred to as hybrid MICs, although the use of the term *integrated* in this case is misleading.

The type of integration drastically affects both cost and performance. Reducing the size of transmission lines reduces the amount of attenuation in the interconnects, and the magnitude of parasitic inductances and capacitances. Gallium arsenide (GaAs) monolithic MICs can operate at frequencies up to 150 GHz or more, but are expensive. The design of such chips has intensive design overhead, requires licensed tools and software, as well as access to expensive fabrication. Other monolithic manufacturing processes used for millimeter wave designs are indium phosphide (InP), gallium nitride (GaN), silicon germanium (SiGe), and plain silicon (often complementary, CMOS). Discussion of each process in detail is beyond the scope of this work. In brief, these monolithic manufacturing processes offer transistors with high frequency of operation due to high electron mobility, and the fabrication of precise and tightly integrated passive devices. With less integration, we get less precision in our transmission lines, and more parasitics in the circuit. However, the design and manufacture of such circuits is much simpler and less expensive.

CMOS and SiGe fabrication are less expensive than GaAs due to the economy of scale of silicon manufacturing. Because of the large volume and prevalence of CMOS, and higher component density, the cost per run of a CMOS design is lower than RF-specific manufacturing processes such as InP or GaAs. CMOS designs have been presented for design of time-domain radar, including many biomedical applications [6]. Because of the potential to reduce cost and decrease circuit size, while also improving performance, SiGe and CMOS processes are potential options for low-cost implementation. However, the need for licensed tools and the design-time makes such tasks prohibitive for many researchers.

To meet the lowest possible cost, designing components using hybrid MICs on PCBs is proposed in this thesis. The most common material used in PCB manufacture is FR4, a glass-reinforced epoxy laminate that offers good electrical and mechanical properties. At a system bandwidth of approximately 6 GHz transmission lines on standard FR4 will cause undesirable attenuation, but are still viable with good design practice. Designs which need other passive microwave devices such as filters, baluns, and couplers have been successfully developed on FR4. Whenever possible FR4 is the preferred manufacturing substrate, as it is the absolute lowest cost. Higher-performing PCB substrates can be used, such as RT/Duriod. This is more expensive than standard PCB etching, but still a better value than monolithic integration.

Because all components implemented on printed circuit boards in this work are microstrips, the basic performance of a microstrip transmission line is reported here. We will discuss the performance of microstrip-based integration for pulse-generators, UWB receivers, and switching matrix implementation, in subsequent chapters.

The lumped-element model of a transmission line is shown in Fig. 2.7. In this model, attenuation is represented by the finite series resistance, R, and parallel conductance, G per unit length. The series resistance R is caused by the conductivity of the microstrip trace. For a microstrip, the finite-conductivity attenuation is approximated by

$$\alpha_c = \frac{R_s}{Z_0 W} \tag{2.8}$$

where $R_s = \sqrt{\omega\mu_0/2\sigma}$ is the surface resistivity. The dielectric loss corresponds to the conductance G per unit length, and is given approximately by

$$\alpha_d = \frac{k_0\epsilon_r(\epsilon_e - 1)\tan\delta}{2\sqrt{\epsilon_e}(\epsilon_r - 1)} \tag{2.9}$$

where k_0 is the wavenumber in free space, ϵ_e is the *effective* dielectric constant, and $\tan\delta$ is the loss tangent [2]. Characteristic curves for microstrip transmission lines are shown in 2.8.

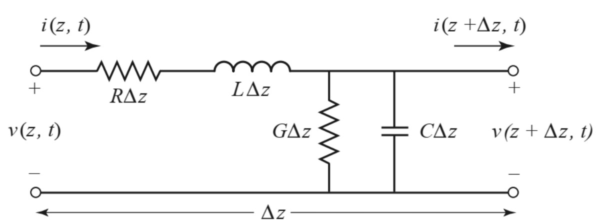

Fig. 2.7 Lumped element model for a transmission line adapted from [2]

The loss due to the conductor tends to dominate in microstrip traces. We reduce conductor loss through use of a thicker substrate (for the same Z_0). This comes at the cost of wider transmission lines and overall larger circuit size. The conductor loss can also be reduced by using smoother copper traces. This is highly manufacturer dependent, and many

PCB designers do not control for this factor. For dielectric loss, the best approach is to use a better quality PCB substrate, which simply increases the board cost. For both types of attenuation, we can reduce loss by reducing lengths of the traces. The effect of shorter traces alone is dominant across all MICs, which leads to the highest performance of monolithic MICs by allowing much higher frequencies to propagate.

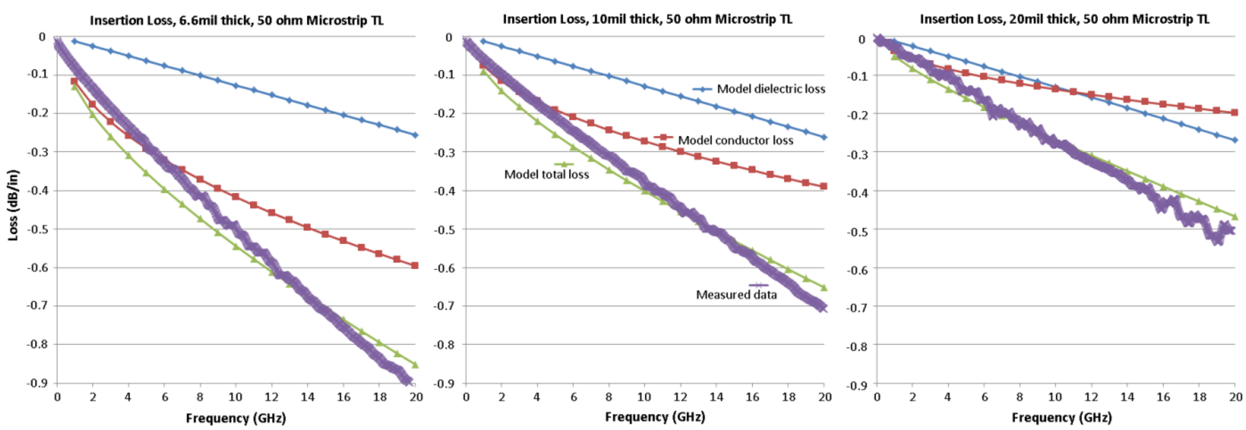

Fig. 2.8 Frequency characteristic of microstrip attenuation implemented on Rogers RO4350B substrate. Figure adapted from [3].

Summarizing, the use of FR4 substrates or a similar PCB material is viable for microwave components up to the 6 GHz range, which means our system for microwave breast cancer detection can be implemented using this low-cost technology. There are few systems taking this approach for designing an ultra-wideband imaging system. If the system is to be low-cost, however, it must be oriented toward the use of standard PCBs and commercially available integrated circuits, rather than custom integrated designs.

2.6 Conclusion

This chapter has presented the role of microwave breast cancer detection in the context of breast cancer screening and discussed hardware aspects of a microwave system. Our system uses time-domain radar in the frequency range of 2-4 GHz, to screen for tumors with skin-contact antenna using high-cost scientific instruments. We here investigate low-cost circuit implementations of the UWB hardware. This requires high-frequency design methods and components, beyond conventional electronics. For optimized cost, hybrid designs implemented using PCB technology are preferred. With these remarks in mind, the subsequent chapters will present proposed solutions.

Chapter 3

Pulse Generators for Time-Domain UWB Radar

The current clinical system, implemented as shown in [19], is a coherent time-domain radar system. This chapter presents both review and measurements of the pulse-generator component in the system, towards the goal of reducing cost and form factor. Measurements of commercially-available available and custom-designed components are measured and analyzed. Due to the lack of a suitable candidate from these, the chapter is concluded with design and fabrication of new impulse generators.

3.1 Review

In the time-domain system, the UWB pulse propagates through the forward path passing through the power amplifier (PA), switching matrix, antenna, breast-tissue, finally being received by the time-domain receiver. This signal chain, along with the approximate power and spectral content at each point, is shown in Fig. 3.1. We would like to reduce the cost by replacing the pulse generator, without compromising performance metrics. The key metrics are the power spectrum in the 0-6 GHz range (measured from the time-domain pulse FWHM and amplitude), jitter, additive noise, and overall cost.

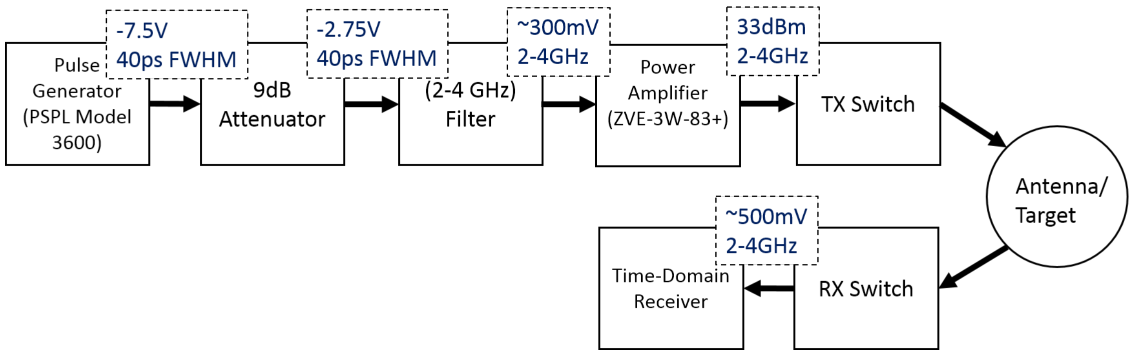

Fig. 3.1 Forward path, with the approximate voltage and spectral content at each point.

The power amplifier dictates the power requirement of the harmonic generator, because it must be high enough to reach full output power but sufficiently low as not to saturate and introduce distortion. To prevent amplifier saturation, the clinical system uses a 9 dB attenuator at the PSPL 3600 output, to reduce the -7.5 V amplitude pulse. With the additional attenuation due to cable loss and filter insertion loss, the input pulse at the PA is at most 0 dBm (300 mV amplitude, 600 mV peak-to-peak). Because target reflections are superimposed with other sources of clutter, we require a coherent and low-jitter signal to localize and declutter the received waveforms.

Using this background, the requirements for the pulse generator are: (i) harmonics in the range 2-4 GHz meaning a Gaussian with FWHM less than 200 ps, (ii) output amplitude in the range 1-2 V, (iii) coherency with system clock, and (iv) less than 100 ps overall phase noise to achieve millimeter accuracy.

There are many approaches to generating wideband pulses. In conventional radar, pulses are generated via multiplication of a high frequency carrier by a pulse [28]. Let a pulse $p(t)$

have a spectrum $P(\omega)$ and define the carrier by $x(t) = cos(\omega_0 t)$. Mixing these two signals will produce the output spectrum $Y(\omega)$:

$$Y(\omega) = P(\omega \pm \omega_0) \tag{3.1}$$

where $p(t)$ is called the *baseband pulse* and ω_0 is the *carrier frequency*. The bandwidth is given by the baseband pulse, and the center frequency is given by the carrier. This technique is not coherent unless the pulse generating circuit and carrier frequency are somehow phase locked. In some radar systems the pulse does not need to be coherent, because the received pulses occur after significant time-delay and only the energy of the returning pulse is measured [28]. To apply this design to our system we would need three discrete components: (1) a frequency synthesizer or PLL able to produce both the carrier and coherent pulse-repetition clock, (2) a baseband pulse generator, and (3) a wideband mixer to perform frequency translation. This approach is viable using integrated circuits as well as using discrete components, but was not pursued in this work to keep overall component count low.

Another approach is to create a wide-bandwidth pulse from a clock signal, and then filter the pulse into the desired frequency band. This approach is inherently coherent, but requires the generation of very narrow pulse-widths. These harmonics are typically generated by making a sharp rising or falling step, which is subsequently differentiated and shaped using passive transmission-line filters [4] [29] [30]. For this reason, pulse or harmonic generators are often characterized by their rise time. Compared to the previous style of pulse generation, much fewer active components are needed. It is less energy efficient as most of the energy produced in this scheme is filtered out, and to produce large harmonics we must drive the edge-sharpening circuit with high power. Common topologies for this approach are non-linear transmission lines (NLTLs), step recovery diodes (SRDs), and transistor topologies consisting of bipolar junction transistors (BJTs) and field-effect transistors (FETs) on both hybrid and integrated manufacturing.

3.1.1 NLTL Circuits

An NLTL consists of a series of transmission line segments, with periodic connections to non-linear capacitors, typically implemented with reverse-biased Schottky diodes [4]. This topology is the state-of-the-art for harmonic generation, with performance well into the 200 GHz range. The circuit, shown in Fig. 3.2, operates as follows. A nominal step input is applied to one end of the line, producing a travelling wavefront. The phase velocity of the propagating wave on the transmission line is given by [2]:

$$v_p = \frac{1}{\sqrt{LC}} \tag{3.2}$$

where L and C are the per unit length inductance (H/m) and capacitance (F/m). Thus, the phase velocity is faster for the the high-voltage portions of the wave than the low voltage portions, due to the lower capacitance induced by reverse biasing the Schottky junction. As the wave progresses each node further sharpens the pulse, reducing the fall time until it becomes less than zero, and it stabilizes to a shock wave no longer being sharpened [4]. At the end of the transmission line, the output is matched to the large-signal impedance of the line, and shaped into a pulse using a passive differentiation network. Like all edge-based harmonic generators, the power of output harmonics can be increased by increasing the power applied to the input. For the NLTL, the maximum output power and harmonic content is fundamentally limited by the reverse-breakdown of the diodes, where increasing input voltage causes them to cease to behaving as varactors.

To achieve multi-GHz range harmonic generation on a NLTL, we need transmission lines

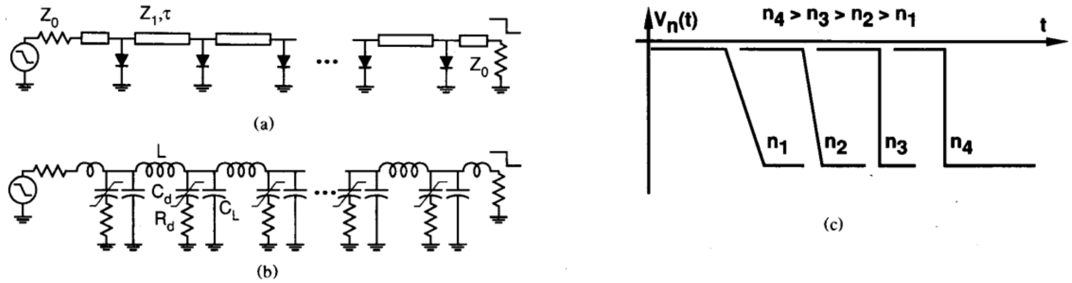

Fig. 3.2 Non-linear transmission line, image adapted from [4]. (a) Circuit schematic, (b) equivalent distributed model, (c) sharpening of the step as it progresses.

and components with very little parasitics. High-performance NLTL designs are typically implemented on GaAs MMICs [4]. NLTLs can also be fabricated using hybrid PCBs at a lower implementation cost. This requires the use of packaged diodes, which must be spaced much further apart than on an IC. In such a configuration there is a trade-off between the degree of non-linearity and the degree of attenuation, dependent on length of the transmission line. More elements in the line will produce high non-linearity but the wavefront will become highly attenuated by travelling long distances on hybrid transmission lines. Analysis and reports of NLTL transmission lines implemented on hybrid PCBs have reported risetimes on the order 800 ps [31], corresponding to a cut-off frequency of about 1 GHz. This indicates integrated MICs are necessary for harmonic generation in our frequency range. NLTL devices producing state-of-the-art impulses are expensive to manufacture although they produce the most powerful harmonics out of any device. To achieve better performance from a hybrid design, the harmonic multiplier must generate harmonics spatially at *one point*, to reduce attenuation due to lossy transmission lines. Fortunately, both SRD-based and BJT-based pulse generators are able to achieve this.

3.1.2 Step Recovery Diode Circuits

SRD pulse generators were first marketed by Hewlett-Packard in the 1960s, and design procedures and applications are clearly described in [32] and [5]. An SRD is a two-terminal device consisting of layers p-type, intrinsic, and n-type semiconductor, and is a particular type of PIN-diode. This specialized device produces a very rapid change in impedance when it is driven from forward to reverse. A typical SRD-based impulse generator is shown in Fig. 3.3.

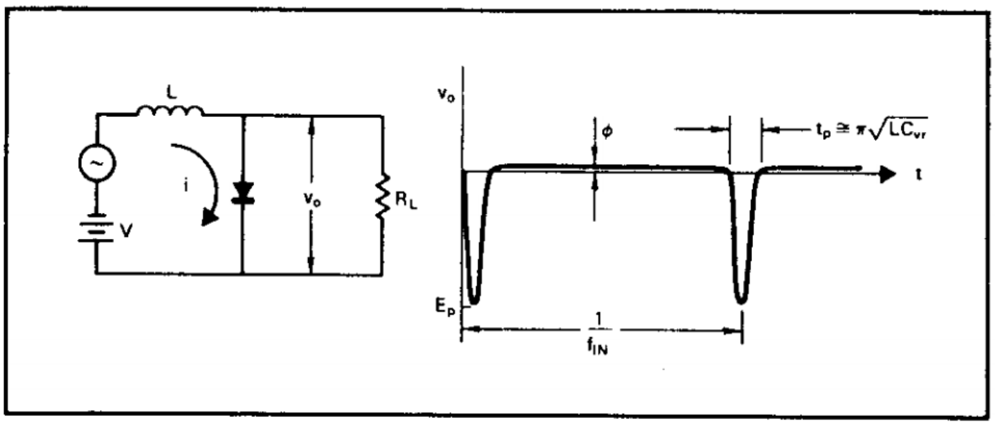

Fig. 3.3 A typical shunt-mode SRD impulse generator which generates a narrow output pulse once per input period. Adapted from [5].

During forward conduction, charge is stored in the minority carriers of the junction (electrons in p-type semiconductor, and holes in n-type semiconductor) because minority carriers have a non-zero recombination time. In the forward conducting state the SRD will have a low impedance, and will continue to have a low impedance until the charge stored in the device is depleted. When a reverse current is applied it will briefly conduct, until the charge is swept out of the junction. The diode will then suddenly switch to its reverse biased state, producing a step change in impedance. In [32], the recommended first-order modelling of the device is as a two-state capacitor: a large capacitance in the forward state, and a small capacitance in the reverse state. This step non-linearity allows for efficient harmonic generation.

To transform the step into an impulse, it can be differentiated through use of an inductive drive, or through a passive microstrip. Multiple SRDs can also be used to shape the pulse in various schemes. A thorough review of published SRD circuit configurations is presented in [33], including some operating in the 0-6 GHz range of interest. In [30], an impulse with 6 V amplitude and 150 ps FWHM was reported using one SRD in shunt-mode configuration. In [34] using three SRDs, an impulse with 6.2 V amplitude and 170 ps FWHM was presented. From these reported results, it is clear that SRD-based impulse generators can be used to generate impulses with suitable power spectrum for microwave breast cancer detection.

There are a few drawbacks with SRD pulse generators. SRDs are difficult to obtain, much more expensive than common diodes, and not held by most electronics vendors. Cost per unit is not openly available. There are not many publications of jitter measurements using SRDs, and they are often reported to have more jitter than NLTL-based impulse generators.

3.1.3 BJT Circuits

A BJT exhibits a step recovery response similar to that of an SRD [29] [11]. The transistor is first driven into the saturation mode by applying a positive voltage base-emitter junction and allowing the collector-emitter voltage to drop. In this state, the BJT presents a low impedance to ground, with both the base-emitter and base-collector junctions forward biased. When the base-emitter junction is reduced to zero, there is a recovery-period when the BJT still conducts. The transistor will then transition rapidly to the off state, producing a rapid step at the output.

This particular BJT property is not frequently documented or discussed in literature. A noteworthy paper demonstrating the use of this BJT property is given by [29], where a

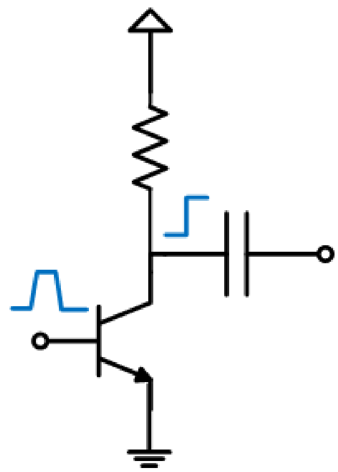

Fig. 3.4 Circuit configuration for generating step recovery effects using a BJT.

BFP540 and a BFR194 BJT are used. Pulses with amplitudes reaching 7 V are presented, and pulse widths as low a 90 ps. In [11] and the BJT-based impulse generator is applied to a time-domain radar system. For the publications cited, differentiation networks are used to shape the pulse.

The BJT-based impulse generation presents a major reduction in cost. Unlike SRDs, which are specialty devices not commonly available, the high frequency BJTs are widely available. Since harmonics are generated in a 'lumped' fashion, unlike NLTLs, harmonics can be produced on a hybrid MIC, rather than on a MMIC. For this reason, this design was chosen as a very attractive topology for replacing the pulse generator in the clinical prototype. There is a lack of publications on jitter introduced by these pulse generators, and would need to be determined experimentally.

3.1.4 CMOS Pulse Generating Circuits

Approaches using CMOS integrated circuits have been presented in numerous journals for UWB communication purposes [6]. The basic digital approach to harmonic generation is shown in Fig. 3.5. During the idle period of the clock, the AND-gate receives different logic levels, and the output is low. However, during positive-to-negative transition, the top path experiences an additional delay due to the 2nd inverter, which causes a brief instance where the AND-gate inputs are both high, thus differentiating the clock signal. The pulse width can be made adjustable by introducing delays (using varactors or digital capacitor banks). The polarity of the pulse can be altered by using different gate types (OR, NAND, etc.). The minimum pulse width achievable depends on the switching speed of the logic, which has been getting increasingly fast with the reduction of transistor scale.

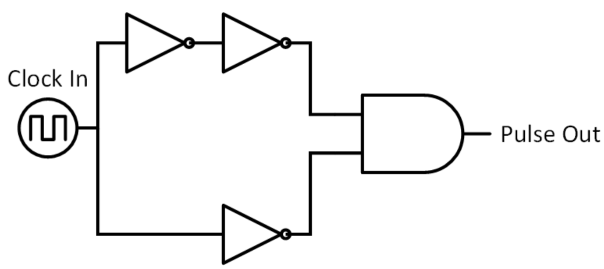

Fig. 3.5 Simple digital pulse generator.

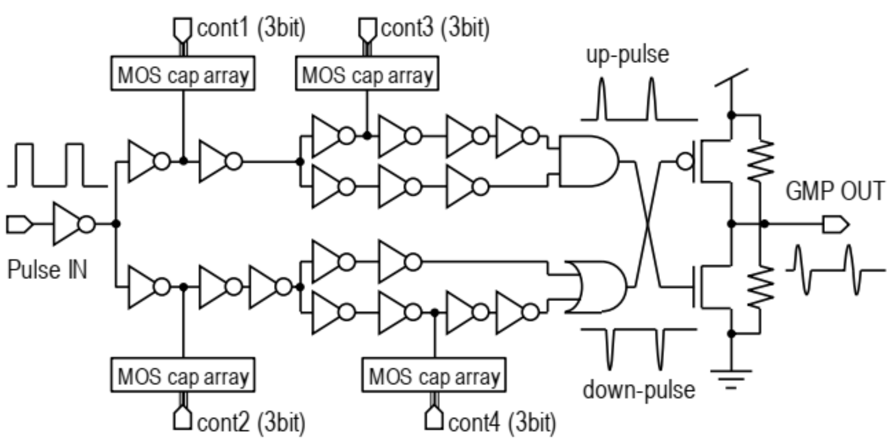

Fig. 3.6 Gaussian monocycle pulse generator as described in [6].

A more elaborate design is shown in Fig. 3.6. Both positive and negative pulses are generated using digital logic. The two output pulses feed the output stage. A small delay is introduced between the positive and negative pulses, which combine to form a Gaussian monocycle. These designs have successfully been adapted to the task of microwave breast cancer detection [6] [35] [21].

CMOS designs may come to offer very high performance at a low cost. They are applicable to time-domain imaging for breast-cancer detection, and offer competitive performance and exceptional control in the design. All components of the system can be implemented on the CMOS IC, offering compact size and good performance. As of now, they have not been produced on a large scale as an integrated time-domain radar product. They are available to labs and companies with the expertise and resources to manufacture integrated circuits. Since this thesis focused on COTS designs, they were not considered.

3.1.5 COTS IC-based Pulse Generators

Recently, commercial off-the-shelf (COTS) ICs which produce fast rising edges have been used to produce low-cost pulse-generators. In [36], an Analog Devices HMC675LP3E SiGe IC was used, which can produce rise and fall times less than 30 ps. Like SRDs, NLTLs, and BJT step outputs, this high-harmonic content can be shaped into a pulse waveform. Using these ICs allow us to take advantage of a high-performance process and professional design and testing, and can be easily manufactured onto a PCB. These components are also readily available from many vendors, at a low cost. A drawback to using these ICs is the low output power. Comparator outputs use low-voltage signalling and would need significant amplification..

3.2 Measurements

Two pulse-generating circuits were procured for the purpose of replacing the impulse generator in the clinical system. One is a SiGe MMIC designed by FURAXA [37], and the other a two-diode SRD circuit designed by our industrial collaborator, Analog Devices Inc. (ADI). For both circuits, the amplitude and pulse-width were measured driven by the AD9576 clock source. The harmonic output power for both designs were beneath what our existing system uses, so further measurements of jitter were not taken.

3.2.1 Clock Generator

As part of the pulse generating system, the clock influences the system performance and pulse-generator performance. Due to the large-scale production of the PLLs for communication and data transfer applications, low-jitter PLLs are available at low-cost. The AD9576 is an ultra-low jitter clock source for instrumentation applications. In all measurements reported it is used as the driving source. Each output is configurable to a number of modes, with both differential and single-ended output supported. We frequently use single-ended clocks for pulse-generators, so measurements of the single-ended performance were taken to ensure compatibility with our equipment and the Picoscope 9400. These measurements are presented in Table 3.5.

The four modes are High-Speed Transistor Logic (HSTL), Low-Voltage Differential Signalling (LVDS), CMOS, and High-Speed Current Steering Logic (HCSL). The HCSL outputs were not usable in our 50 Ω system. The CMOS output has two voltage levels, 3.3 V and 1.8 V. From the measurements, the LVDS mode showed the fastest rise times once the frequency reached around 50 MHz. The 3.3 V CMOS output has the highest peak-to-peak amplitudes. All clock modes showed very low jitter. Overall, all modes are safe to use with the Picoscope, which has a ± 2 V input voltage tolerance, and the CMOS output is the best candidate for driving SRD-based pulse generators which benefit from higher amplitudes.

Table 3.1 Measurements of AD9576.

Output Mode	Frequency	Rise Time	Jitter	V(peak-to-peak)
HSTL	10 MHz	237 ps	5 ps	715 mV
	25 MHz	245 ps	5 ps	715 mV
	50 MHz	193 ps	1.4 ps	715 mV
	100 MHz	472 ps	3.9 ps	674 mV
LVDS	10 MHz	472 ps	5.0 ps	370 mV
	25 MHz	601 ps	5.6 ps	372 mV
	50 MHz	97 ps	4.9 ps	371 mV
	100 MHz	93 ps	3.5 ps	371 mV
CMOS (1.8 V)	100 MHz	150 ps	4 ps	675 mV
CMOS (3.3 V)	100 MHz	215 ps	3.7 ps	1.16 V

3.2.2 FURAXA SAMPULSE20x2

The FURAXA SAMPULSE20x2 was previously integrated into the system, showing that despite the lower amplitude pulses we can reach the same pulse power by adding an additional LNA to the system [38]. This section does not extend that work. Rather, a time-domain measurement of the FURAXA is provided with the AD9576, as a reference performance metric for future pulse-generator designs.

The FURAXA SAMPULSE20x2 product specification lists the pulse amplitude as adjustable between 300 mV and 30 mV, with a pulse width of 16-22 ps. To validate this, the pulse was driven by the ADI9576. The rise-time and amplitude of the clock affects the pulse width and amplitude. LVDS output in differential mode was chosen as it provides the fastest rise-times, and a suitable 700 mV differential amplitude as specified by the FURAXA product datasheet.

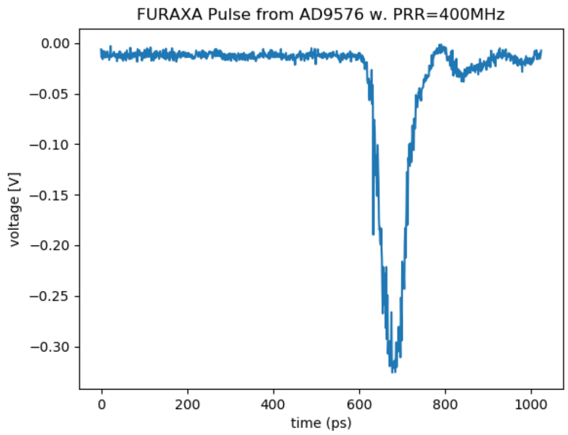

Fig. 3.7 Measured pulse from the FURAXA SAMPULSE20x2 when driven differentially by the AD9576.

The measured pulse is shown in Fig. 3.7. We observe a pulse amplitude of 300 mV, with a FWHM of 50 ps. The pulse width at the output may in fact be narrower and closer to the datasheet, due to bandwidth limitations in the cables and Picoscope (12 GHz). The pulses are lower amplitude than what is used in the existing system, but overall the device performs very well and matches the specifications of the datasheet. Because the circuit is also quite expensive, alternative pulse generators should be investigated.

3.2.3 ADI Pulse Generator

The pulse generator designed by our collaborator ADI is shown in Fig. 3.8. The full design and simulation details were not provided, so assumptions were made about the circuit from review of SRD-based circuits. The circuit uses two SRDs, one in shunt and one in series, and does not use inductive drive. Bias-tees are included to provide DC bias to the diodes. The passive elements connecting the SRDs were assumed to be for input and output matching. Since pulse amplitude and width are affected by input power and shape, the pulse generator was measured under a number of configurations: (1) fed by the AD9576 connected via coaxial, and (2) fed by a function generator, with increasing amplitude.

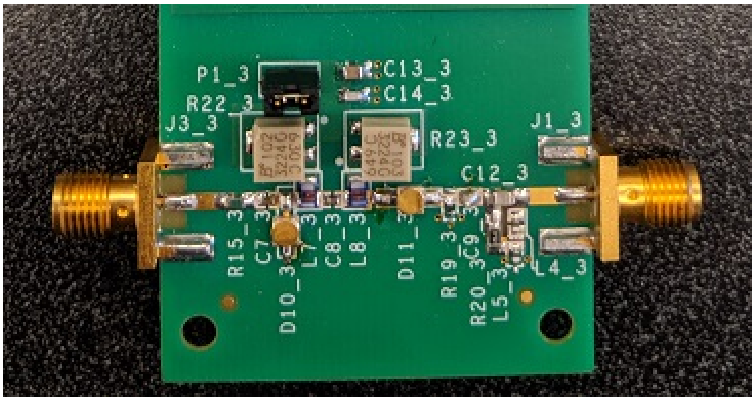

Fig. 3.8 Two-SRD Pulse generator designed by ADI.

The results of direct-clock feeding are provided in Table 3.5, where the 3.3 V CMOS output of the AD9576 is used. A time-domain plot of the measurement is shown in Fig. 3.9. We observe the pulse width is consistently narrow for different clock frequencies. We also observe a low pulse amplitude of 85 mV for the 3.3 V CMOS input. The 3.3 V output is the highest amplitude we can provide from the AD9576 clock generator. To increase the amplitude of the pulses produced, a function generator was used to provide higher input power. The resulting measured pulses are summarized in Table 3.3 with 3.10 showing the measured waveforms. Unlike the AD9576, the function generator is not output matched, which effectively doubles the voltage applied to the SRD circuit. However, the applied waveform is a single-cycle sinusoid, rather than a square-wave. This results in some inconsistencies between the two datasets, but they are still generally comparable. Ramping the input voltage results in higher amplitude pulses, but all voltages are still far below what we need for our application, and also below what is expected of SRD circuits [33].

There are a number of approaches we can take to improve this circuit performance. Replacing the coaxial cables with short-length connectors will reduce the attenuation, which improves the pulse amplitude and reduces noise. The pulse generator also provides bias

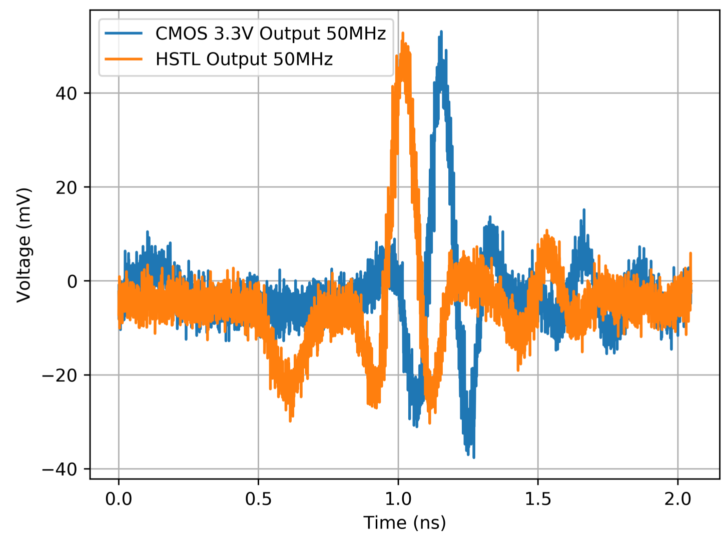

Fig. 3.9 Measured waveforms with ADI pulse generator directly fed by AD9576.

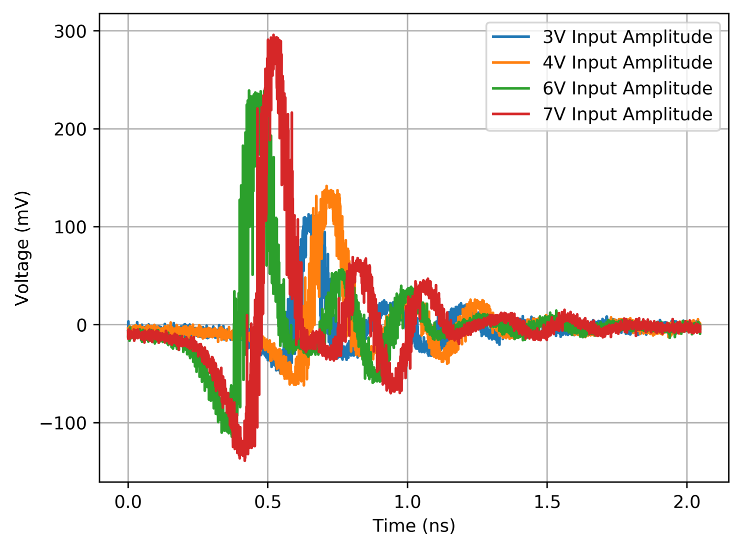

Fig. 3.10 Plot showing effect of ramping input power to ADI SRD pulse generator

Table 3.2 ADI Pulse Generator - Direct Feed from AD9576

Clock Frequency	Output Mode	Total Width	FWHM	Pulse peak-to-peak
25 MHz	CMOS 3.3 V	200 ps	102 ps	87.5 mV
50 MHz	CMOS 3.3 V	180 ps	85 ps	82 mV
100 MHz	CMOS 3.3 V	178.5 ps	89 ps	82.5 mV
100 MHz	HSTL	200 ps	107 ps	77.5 mV
100 MHz	LVDS	200 ps	107 ps	20 mV

Table 3.3 ADI pulse measurements driven by a function generator. Input column represents input amplitude of the function generator.

Clock Frequency	Input	FWHM	Pulse peak-to-peak
12.5 MHz	3 V	90 ps	162 mV
12.5 MHz	4 V	90 ps	204 mV
12.5 MHz	6 V	90 ps	353 mV
12.5 MHz	7 V	90 ps	435 mV

networks which may have a substantial effect on the pulse height, but will require trial and error to find the optimal point. With some adjustment and tuning, this pulse generator may be a viable replacement to the existing PSPL pulse-generator, but current performance is far from ideal.

This pulse generator has several shortcomings, enough to warrant a new design. Foremost, the use of SRDs in general is a challenge because they are difficult to obtain in small quantities, and often expensive. This design relies on two SRDs, effectively doubling the cost of the circuit. Single-SRD circuits have been demonstrated to produce pulses of widths approximately 140 ps or less, with harmonic content in the desired bands. This means a lower cost design is possible.

3.2.4 Discussion

We have shown some reference measurements from a SiGe MMIC and an SRD-based impulse generator. Both were capable of providing UWB pulses, producing harmonic content in the desired 2-4 GHz frequency bands. However, the measured amplitudes are below what we need for current instrumentation without additional amplification. Further study and design is needed to provide a compelling low-cost harmonic generator for our application. BJT-based harmonic generators have been applied successfully for time-domain radar applications, and are easier to obtain at lower cost than SRDs. The SRD-based impulse generator appears to perform below what is possible from a literature review of such circuits. The next sections cover the design of these lower-cost pulse generators: (1) a BJT-based impulse generator and (2) a single-SRD impulse generator.

To accommodate the measured pulse generators, reducing the output power in the system could be investigated. Using high-power allows for a very high SNR, but measurements in this section indicate that a lower system power would ease requirements on pulse-generating circuitry. A receiving LNA can be used to receive lower overall output power, with minimal changes elsewhere in the system. Such a change would be straightforward to evaluate with phantoms in imaging scenarios.

The FURAXA board also includes an RF sampler, which samples the two outputs and can also observe reflections. However, it does not allow one output to be used as output, while the other is used as a receive mode. To accommodate the transmission and receiving of reflections in the system, would require a circulator, and careful removal of the incident pulse on the line. In the product reference material, the circuit has been applied without the use of any external amplifiers as a time-domain radar for medical imaging. This is a deviation from our system design, as it uses S_{11} reflections rather than S_{21} transmissions for each antenna. This avenue may be worth investigation, as we are not using the full capabilities of the board, nor using it as it was intended.

3.3 Design

This section will cover three designs towards a low-cost pulse generator implemented on FR4; (1) a BJT-based impulse generator, (2) an SRD-based impulse generator, and (3) a tunable pre-amplification circuit for driving SRD circuits.

3.3.1 Design of BJT Impulse Generator

A BJT-based pulse generator was designed based on the transmitters described in [11] and [29]. The design consists of three stages: a clock driving circuit, the BJT in step recovery mode, and a differentiation network. The schematic is shown in Fig. 3.11. The clock driver is a D-latch which triggers a monocycle pulse on the clock edge. The rising edge of the latch output drives the base-emitter junction positive, while the falling edge sweeps it back to zero. This produces a sharp rising edge at the BJT output. Then a differentiation network is used to shape the edge into a pulse, followed by a diode to clip off negative transients. Beyond the passive elements, the circuit only requires a D-Latch, a BJT, and a Schottky diode. The list of components and cost are listed in Table 3.4.

To differentiate the pulse, we use a shorted microstrip stub connected in parallel. At the junction of the stub, the incident step will split between the two paths. The shorted step will cause a delayed and inverted reflection, which approximates differentiation through the relationship:

$$x'(t) \approx \alpha_1 x(t) - \alpha_2 x(t-d) \tag{3.3}$$

where α_0, α_1 and α_2 are arbitrary attenuation constants produced by the differentiating

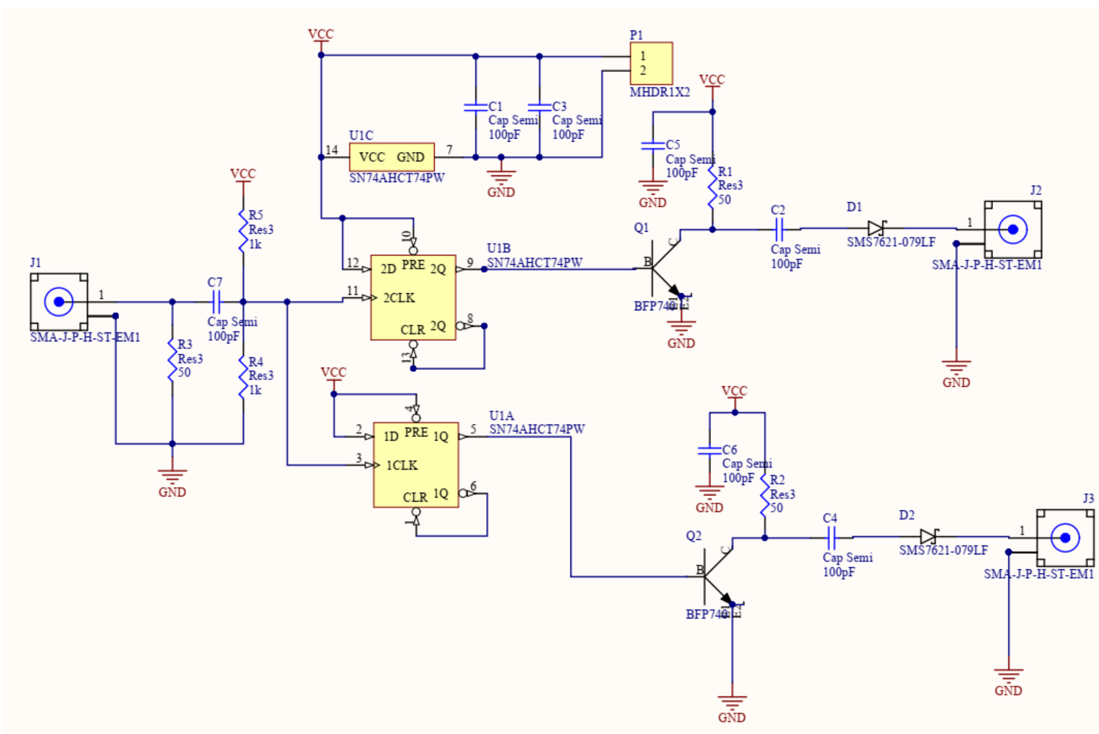

Fig. 3.11 Altium schematic for manufactured BJT impulse generator.

network. In terms of S-parameters, we want the network to equalize the decreasing square-wave harmonics into flat harmonics through the forward transfer function of S_{21}.

To determine an appropriate length, simulations were performed using Keysight-Agilent ADS. An exemplary differentiation network is shown in 3.12. The resulting S-parameters and time-domain waveforms are shown in Fig. 3.13. We observe a characteristic of differentiation in S_{21}, with the frequency monotonically increasing across the bandwidth of interest.

The network has a tradeoff between amplitude and width, where a longer delay line produces a higher amplitude pulse, but wider pulse width. To provide measurements of this effect, two different differentiator lines were implemented on the board. The fabricated pulse generator is shown in Fig. 3.14. The circuit was designed on FR4 material, which cannot maintain high frequency signals on long traces, so the microstrips were kept as short as possible in the transmit path.

Table 3.4 Discrete Parts for BJT-based pulse generator

Part	Description	Cost (CAD)/each
SMS7621-079LF	Schottky Diode	\$0.74
BFP740FH6327XTSA1	RF NPN BJT (42 GHz)	\$0.97
74AHCT74PW	D-Latch	\$0.47

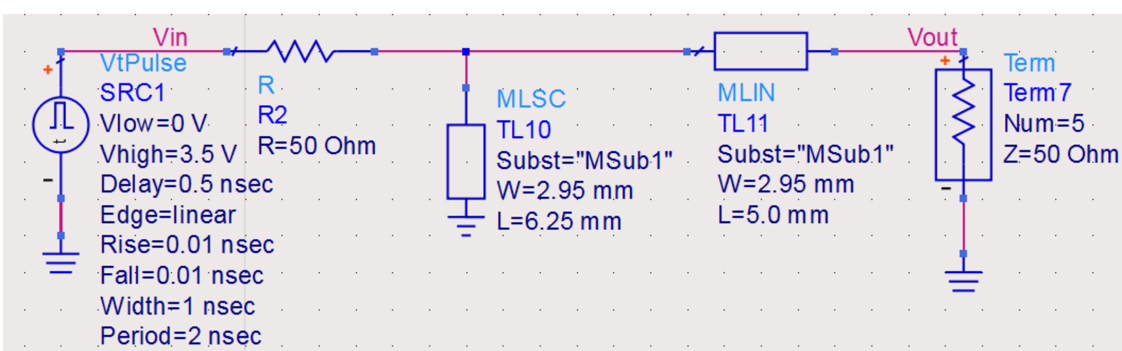

Fig. 3.12 ADS simulation of microstrip differentiator on FR4.

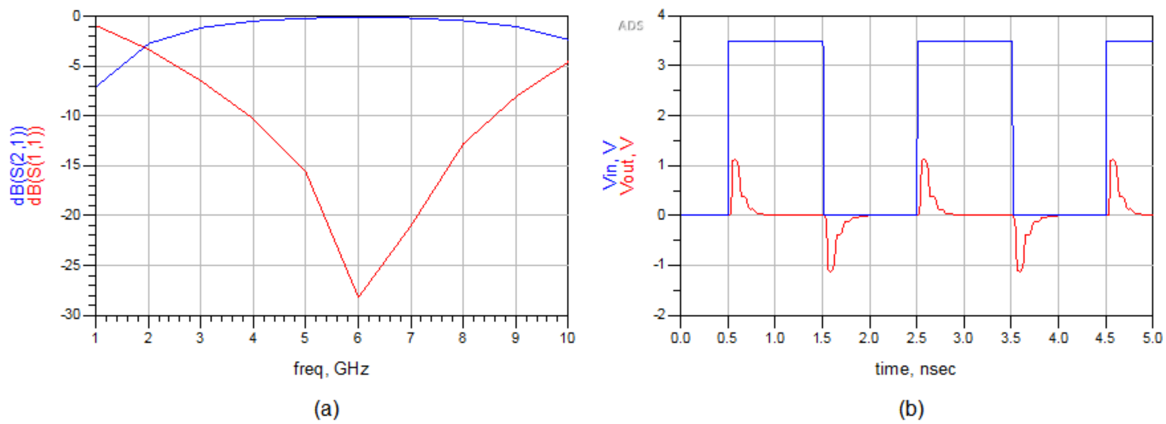

Fig. 3.13 Simulation results of microstrip differentiator. (a) S-parameters of differentiation network (b) time-domain simulation of input (blue) and output (red) for a square wave.

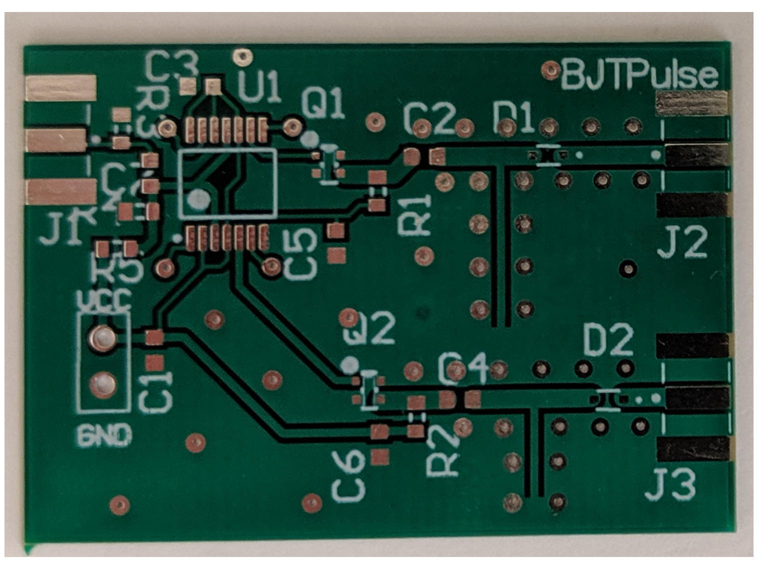

Fig. 3.14 Fabricated BJT impulse generator on FR4.

The manufactured boards have not yet been populated and evaluated. Measurements from the literature indicate that pulses can be produced as narrow as 90 ps and amplitudes as high as 7 V [29]. No references have yet reported jitter measurements, which is key for our time-domain coherent radar system. A set of measurements should be undertaken to see if this topology meets our requirements. If so, it would provide a great reduction in cost compared to all other types of pulse generators.

3.3.2 Design of Step Recovery Diode Pulse Generator

The design of a simple SRD based pulse generator is presented here. The pulse-generator was designed and simulated using ADS, then implemented on FR4 substrate using Altium and manufactured. Due to the limited availability of accurate models of SRD step recovery effects, the simulation results from ADS are not included, as they did not produce realistic output waveforms.

The topology chosen was an inductively driven shunt-mode SRD as shown in Fig. 3.15. This topology is very common and one of the earliest proposed circuit configurations of the SRD [32]. The impulse is generated by using an inductor. In [39], measurements of shunt-mode impulse generators indicate that an inductor in the range of 2-20 nH are appropriate. A simple shunt-mode SRD circuit layout was made in Altium, and manufactured using 0.6 mm FR4. The fabricated circuit is shown in Fig. 3.16.

A MACOM SMMD84RD was acquired for evaluation. This diode has a reverse recovery time of 70 ps. The boards are not yet populated and tested. After population, the circuit should be tested analogous to the previously measured SRD-based impulse generator. Driven directly by the PLL, the impulse amplitude, FWHM, and jitter should be measured with the Picoscope 9400. These measurements can be repeated driven by an amplitude ramp controlled by the function generator. Evaluation of the effect of the inductance should be

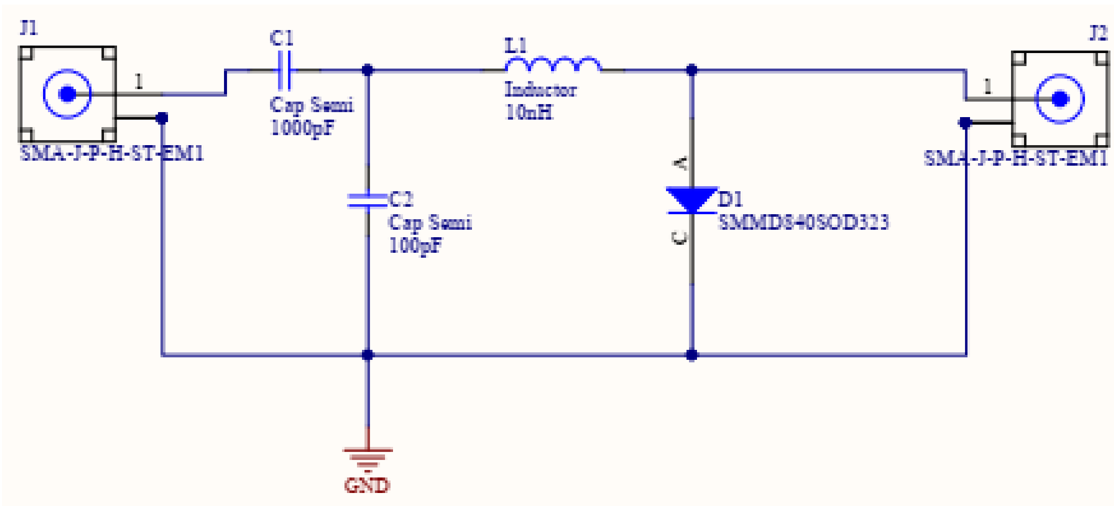

Fig. 3.15 Altium schematic of SRD based pulse generator.

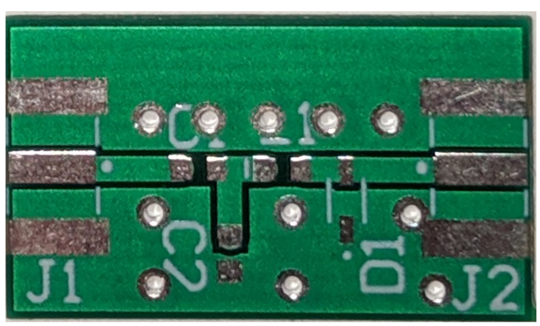

Fig. 3.16 Fabricated, unpopulated SRD diode impulse generator

reported, by testing several drive values.

3.3.3 Pre-amplification Circuit

Harmonic power produced by SRDs increases in proportion to the applied voltage. It is also important to drive the circuits with a sufficiently fast rise-time in order to sweep the charge out of the conducting diode faster than the storage time and induce the step recovery effect. This requires a fast and synchronous clock amplification circuit.

Toward this aim, a CFA-based clock amplification circuit was designed, as described by [30]. A 400 MHz bandwidth CFA (THS3001) is used in a non-inverting configuration. The circuit uses only a single DC supply, to reduce wiring. A trimpot allows adjusting the gain. The circuit can amplify a clock signal up to maximum of 10 V amplitude (20 V peak-to-peak). The schematic is shown in Fig. 3.17, and the final manufactured circuit under test is shown in Fig. 3.18. The resulting high-bandwidth preamplifier output is shown in Fig. 3.19.

Measurements of this circuit show functionality, but the circuit introduces some phase noise into the system. This is likely due to power-supply noise and electromagnetic interference. This problem must be addressed before using it with SRD impulse generators. Some approaches to fix this are shielding, ferrite beads, and/or additional bypass capacitors on the power-supply.

3.4 Conclusion

This section has provided a review and measurements of various pulse generators. The system could be adapted to use the FURAXA or ADI pulse generator, although the forward gain of the system would be reduced. The FURAXA is also too expensive to justify as a low-cost alternative. Steps toward more cost-effective impulse generation were presented with

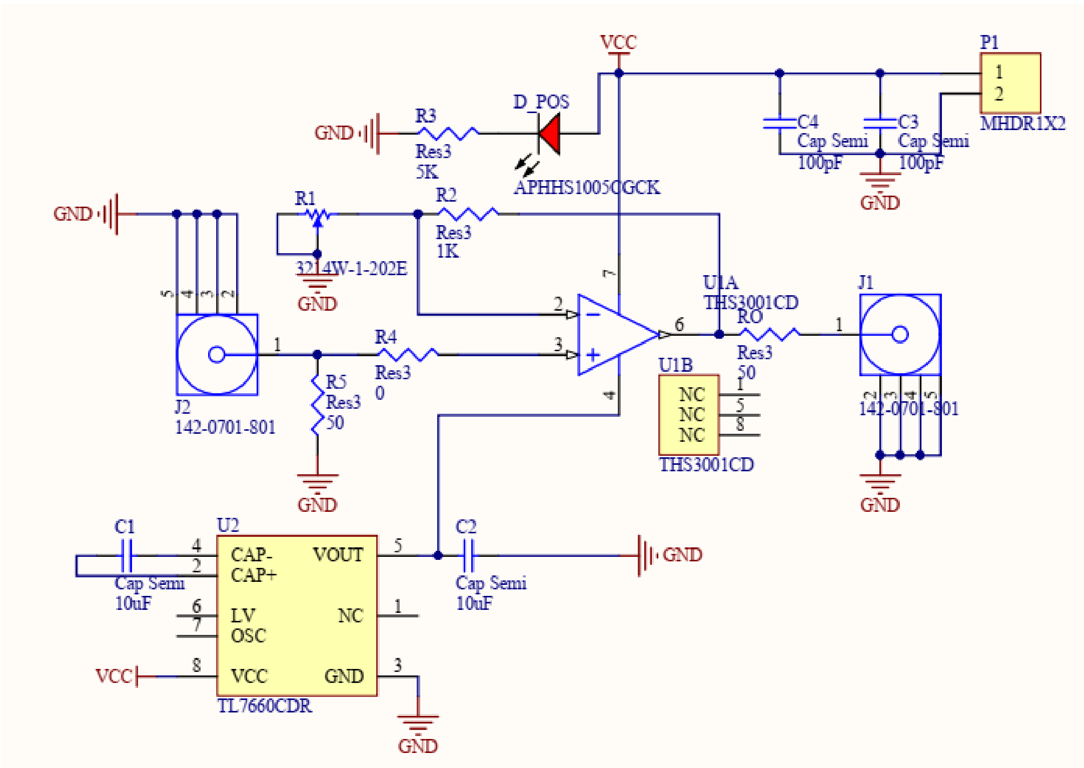

Fig. 3.17 Preamplier circuit schematic.

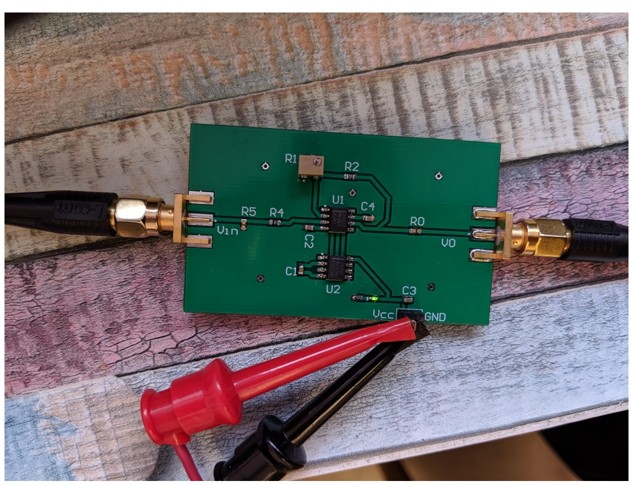

Fig. 3.18 Assembled preamplifier circuit under evaluation.

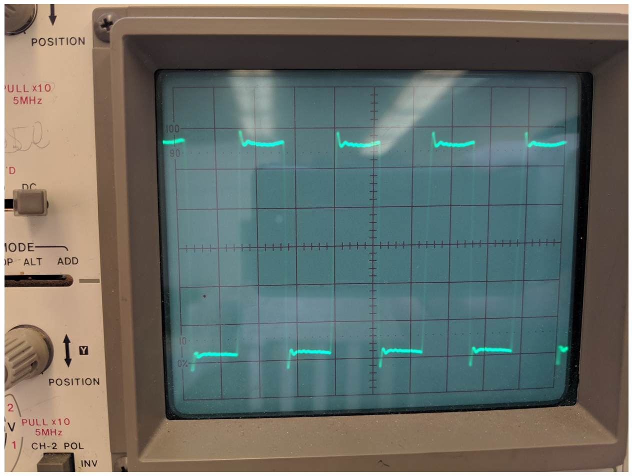

Fig. 3.19 Recorded preamplifier output. Preamplifier is driven by AD9576 and amplified to 10 V peak-to-peak.

BJT and SRD based impulse generators. Two designs were implemented on FR4 substrate, but require measurements to characterize them. Overall the cost of the system would be drastically lower, assuming the topologies chosen do not introduce phase noise and produce enough harmonic content.

To characterize the pulse generators, time-domain measurements with the phase noise, FWHM, and amplitude of the resulting pulses should be recorded. Driving circuitry should also be considered, as it may introduce phase noise, power-supply noise, temperature drift, and has a large effect on SRD-based pulse generators. The driving circuitry for the SRD-based pulse generator consists of a CFA amplifier, direct feed from the clock, or a trigger-able function generator. The BJT-impulse generator currently has only a D-latch based driver; this could be replaced with higher-voltage driving circuitry to produce stronger pulses.

Literature indicates that the new proposed and measured designs may drastically reduce the cost of the system, but require further development to integrate them into the breast cancer detection system.

Revision to Chapter 3

This revision consists of measurements planned for Winter 2020 that could not be completed with lab restrictions during the COVID-19 pandemic. It also includes new and previously unreported circuit simulations.

3.5 Revision: Introduction

Components previously investigated for our clinical system have been shown to be either too expensive, or below specifications. CMOS ICs have also been investigated, by our group and others [35], but are not affordable for small-scale designs. This thesis provided a review of hybrid designs, which can be implemented using conventional PCBs and discrete off-the-shelf components. The most promising circuits from this review were an SRD-based inductive pulse generator and a BJT-based design. Both circuits offer an exceptionally low cost, with an estimated bill of materials $40.00 CAD for the SRD circuit, and $20.00 CAD for the BJT circuit. From review of literature, these circuits have not yet been evaluated and applied to microwave breast cancer detection. To address this, the circuits are here simulated, prototyped, and measured.

Table 3.5 Cost comparison of pulse generating circuits

Previous Work	
Circuit	Estimated Cost (CAD$)
PSPL 3600 [40]	30,000
FURAXA Sampulse [37]	5,000
Custom MMICs [35] [4]	N/A (very high)
This Work	
Circuit	Estimated Cost (CAD$)
Inductively-driven SRD [30]	40
Step-recovery mode BJT [29]	20

Table 3.6 Desired performance of pulse generator.

Parameter	Design Goal
Output Bandwidth	>5 GHz
Jitter	<100 ps RMS
Pulse Repetition Rate	10-25 MHz

3.6 Revision: BJT-based Impulse Generator

During assembly the circuit was modified to accommodate a DC coupled clock source by replacing the AC capacitor and resistive divider with a short. Also, power-supply decoupling capacitors were increased to 10 uF, and the AC coupling capacitor between the BJT collector and the stub was increased to 100 nF. The finalized circuit is shown in Fig. 3.20, and the assembled circuit is shown in Fig. 3.21.

3.6.1 Simulation

The circuit was simulated in two-stages; (1) the BJT exhibiting the step-recovery effect, (2) and the differentiation network. The simulation for demonstrating the step-recovery effect of the BJT is shown in Fig. 3.22. The BJT was modelled using the manufacturer provided BFP740 SPICE model. The simulated 10% to 90% rise-time at the collector is ap-

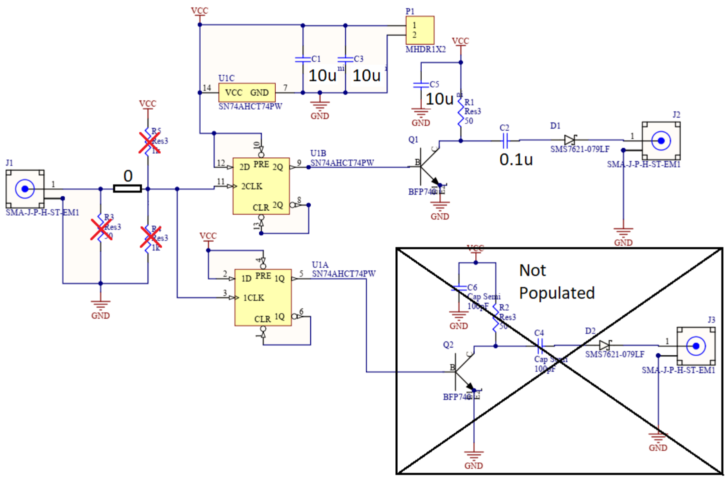

Fig. 3.20 Modifications made during assembly to accommodate DC coupling, increase power supply decoupling, and widen output bandwidth.

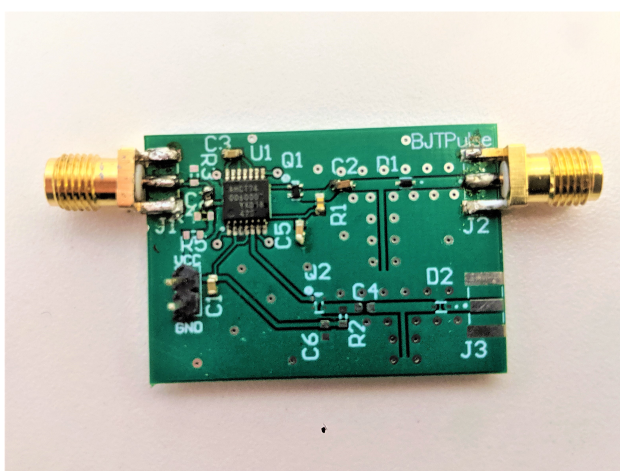

Fig. 3.21 Assembled BJT pulse generator.

proximately 70 ps in this simulation. Using the results of this simulation, and with reference to measurements provided in [29], we simulated the input to the second stage as an ideal square wave with a rise-time of 70 ps.

Two stubs with different length were included in the prototype, to provide a margin of error in the realized microstrip stubs. The two stubs are defined in Table 3.8. Only the upper stub was populated and evaluated in this work. Fig. 3.23 provides a SPICE simulation using the two stub lengths. They are modelled as lossless transmission lines under drive of a 70 ps rise-time square wave. We observe a trade-off between pulse-width and amplitude, with the longer stub producing a wider width, higher amplitude pulse. Modelling of the Schottky as an ideal rectifier, we predict pulses of 180 ps FWHM and 1.25 V amplitude from the 8.9 mm stub output, and 90 ps FWHM and 1.05 V amplitude from the 4.7 mm stub.

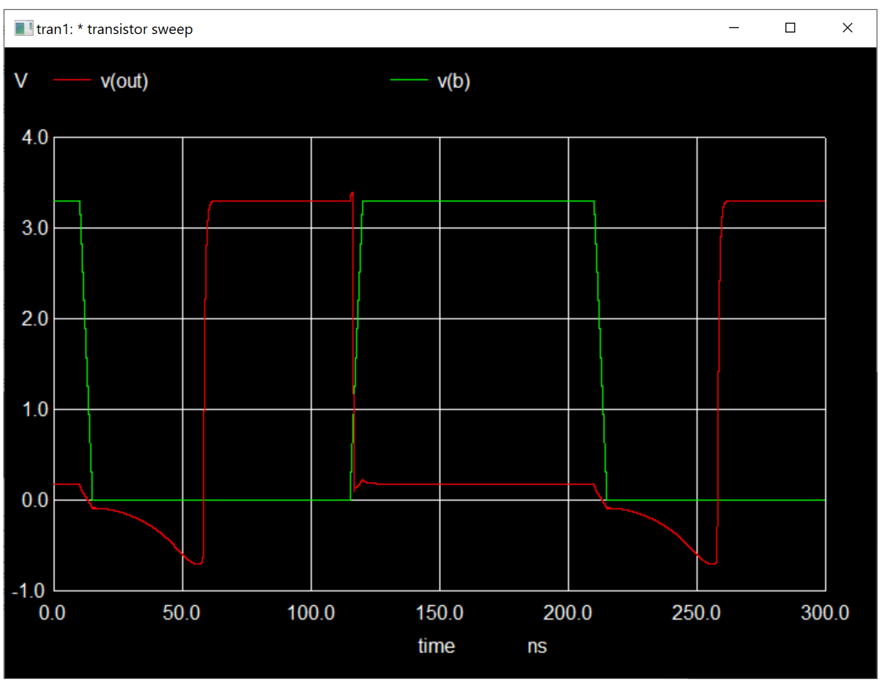

Fig. 3.22 SPICE simulation of the step recovery effect of unloaded BJT circuit (collector output). V(b) denotes the waveform applied to the base of the BJT, which is provided by the D-latch in the realized circuit.

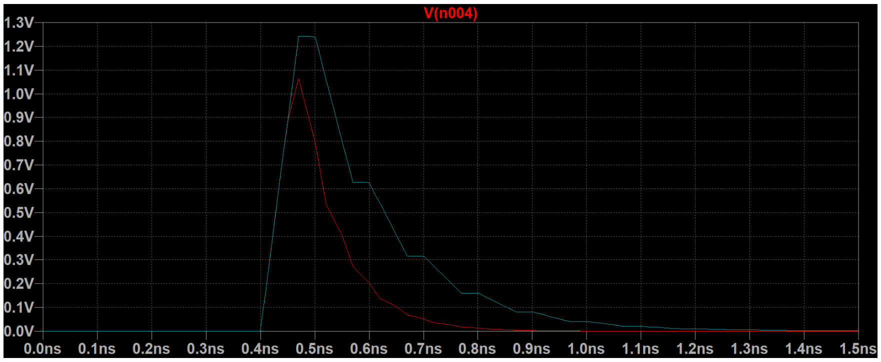

Fig. 3.23 SPICE simulation of the two manufactured stubs, a 8.9 mm stub (teal) and a 4.7 mm stub (red). Only the 8.9 mm stub was measured in this work.

Table 3.7 Parameters of differentiating stubs used in BJT impulse generator.

Parameter	Upper Stub	Lower Stub
Depth	0.6 mm	0.6 mm
ϵ_r	4.5	4.5
Width	0.5 mm	0.5 mm
Length	8.9 mm	4.7 mm
Time Delay	50.7 ps	25.4 ps

3.6.2 Measurements

The BJT pulse generator was driven by a low-jitter 10 MHz DC-coupled square wave produced by an Agilent 81180A. The output is observed by a Keysight/Agilent DSOX91604A. The resulting output pulse is shown in Fig. 3.25. The pulse has an amplitude of 1.1 V and a FWHM of 150 ps. This confirms the BJT is exhibiting the step-recovery effect, and the differentiating stub is effective in shaping the step into a comb. The Schottky diode is also functioning properly by removing trailing negative-going pulses.

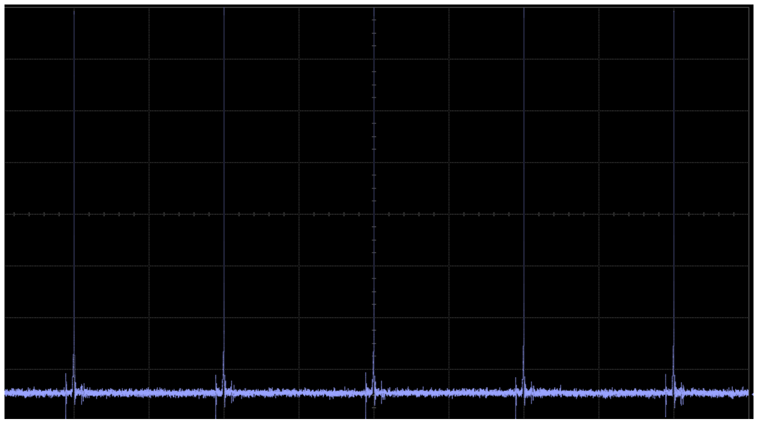

Fig. 3.24 Measured BJT output pulse sequence at 10 MHz.

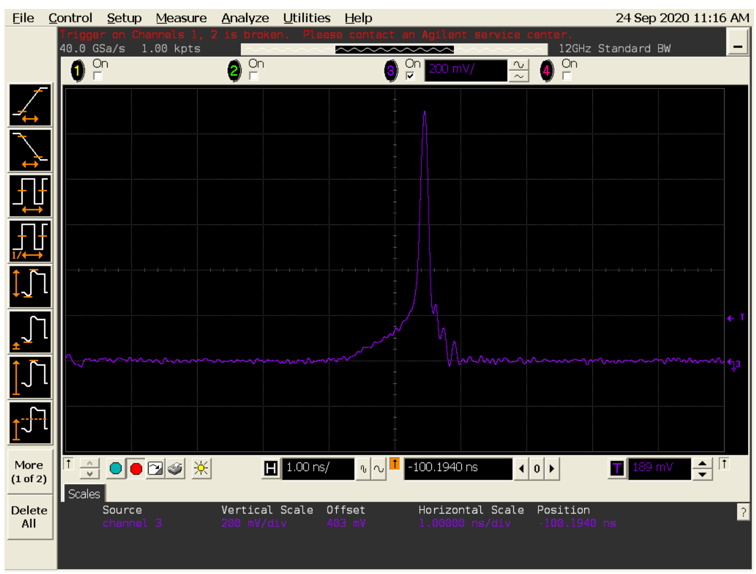

Fig. 3.25 Measured BJT output pulse on a 1 ns/div scale.

From these measurements, the BJT pulse generator provides exceptional performance in producing narrow output pulses. Approximating the pulse as a Gaussian, the spectrum will have 5.89 GHz FWHM, a 2.44 GHz 3 dB cutoff and a 4.17 GHz 6dB cutoff. The amplitude is sufficiently high and the width is sufficiently narrow for filtering into a 2-4 GHz coherent ultra-wideband pulse. The final metric of performance to be evaluated is jitter, which will determine the ranging accuracy and overall viability of this circuit.

3.7 Revision: Inductively-Driven SRD

The SRD circuit uses an inductively-driven topology. From [5], the unloaded pulse amplitude E_p and pulse width t_p are

$$E_p = I_p\sqrt{\frac{L}{C_{VR}}} \tag{3.4}$$

and

$$t_p = \pi\sqrt{LC_{VR}} \tag{3.5}$$

where C_{VR} is the capacitance during reverse drive, I_p is the current stored in the inductor just before transition, and L is the drive inductance. Higher inductances produce higher voltage but wider widths. The C_{VR} includes the reverse capacitance of the diode, as well as parasitic capacitances at the output. In the simulations that follow we show that a value of 10 nH provides a simulated pulse-width of 200 ps, and was used as a starting point for the prototype circuit. The circuit was integrated using 50 Ω microstrips on an FR4 substrate of 0.6 mm dielectric thickness. The input was configured for DC-coupling and a 10 pF capacitor was added to the output to block the input signal feed-through and isolate the pulse. The finalized schematic and assembled circuit are presented in Fig. 3.26 and Fig. 3.27.

3.7.1 Simulation

A simulation of the circuit in the finalized configuration was undertaken using SPICE, shown in Fig. 3.28. The signal source is configured as a 2 V peak-to-peak 50 Ω equivalent, zero DC-offset square wave with 10 ps rise time at 20 MHz with 50 Ω output impedance. We

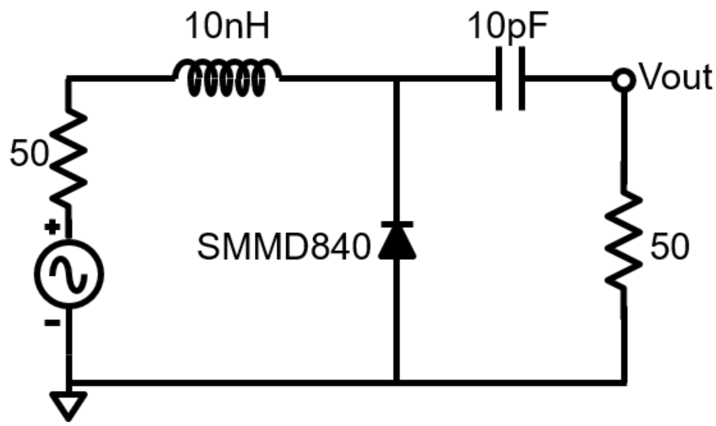

Fig. 3.26 Schematic of SRD circuit before measurement, after final modifications during assembly.

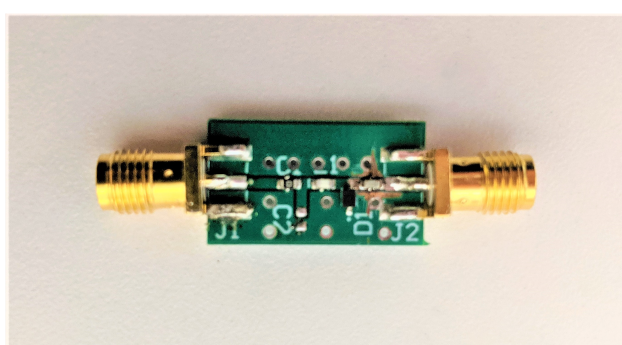

Fig. 3.27 Assembled SRD impulse generator.

observe both positive and negative going pulses, with the positive ones being generated by the step recovery change in current, and the negative pulse being generated by the inductor differentiating the falling clock edge.

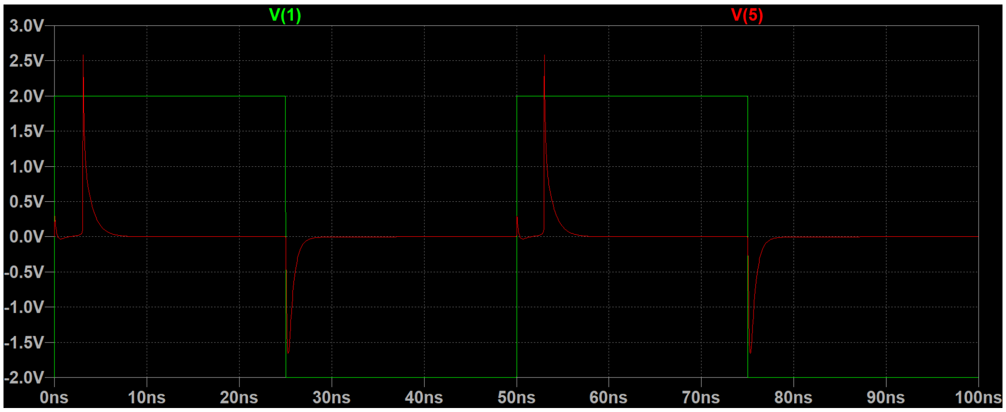

Fig. 3.28 Simulation of finalized circuit design, driven a 2 V peak-to-peak 50Ω 10 ps rise-time square wave.

Additional simulations were performed to characterize the effects of input rise-time and amplitude. A simulation with a slower rise-time is shown in Fig. 3.29. Reducing rise-time reduces the negative-going pulse amplitude, while preserving the positive pulse. There is also a minimum rise time to fully deplete the carriers in the SRD and induce the step-recovery effect. For increasing input voltage, the output pulses simply increase in amplitude. In Fig. 3.30, square waves of 1 V, 2 V, and 3 V amplitude are simulated, and we observe 1.6 V, 2.6 V, and 3.6 V output pulses each with a 200 ps FWHM.

3.7.2 Measurements

The circuit was driven using a Keysight/Agilent 33250a and observed with a Keysight/Agilent DSOX91604A 12 GHz real-time oscilloscope. The output pulse sequence from a 10 MHz and 1 V peak-to-peak source is shown in Fig. 3.31. The circuit was measured under similar conditions to the previous simulations, with 1 V, 2 V, and 3 V peak-to-peak square waves.

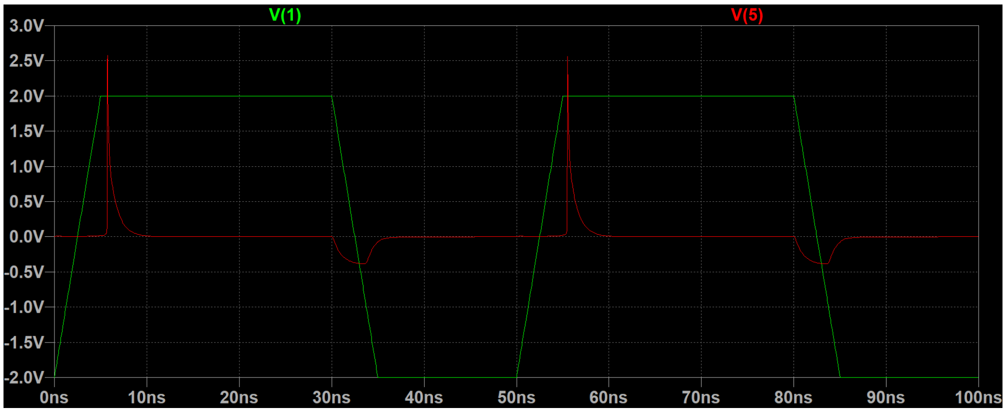

Fig. 3.29 SPICE simulation using vendor-provided SMMD840 device models. Output pulses (red) of finalized SRD circuit, with a 2 V peak-to-peak 50 Ω 5 ns rise-time square wave input (green).

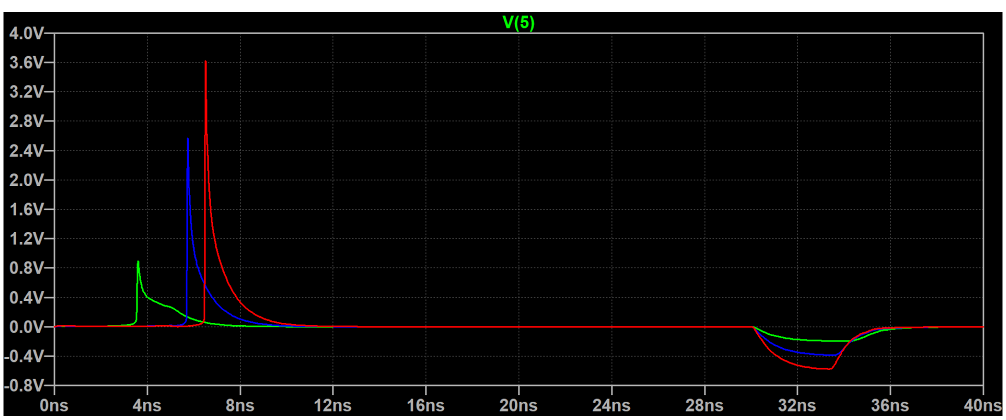

Fig. 3.30 Simulation of SRD circuit for varying input amplitude. Driven by a 5 ns rise-time square wave with 1 V (green), 2 V (blue), and 3 V (red) peak-to-peak amplitude at 50 Ω.

The waveforms were extracted from the oscilloscope to produce the image in Fig. 3.33. The pulses have amplitude of 0.9 V, 1.8 V, and 2.4 V with a FWHM of 400 ps, somewhat lower in amplitude and wider than what was simulated. One factor is that in simulation, the SRD transitions from low to high impedance instantaneously rather than the 70 ps of the real diode. Another factor may be the underestimation of the parasitics at the inductor-SRD node, which reduce the width as shown in 3.5.

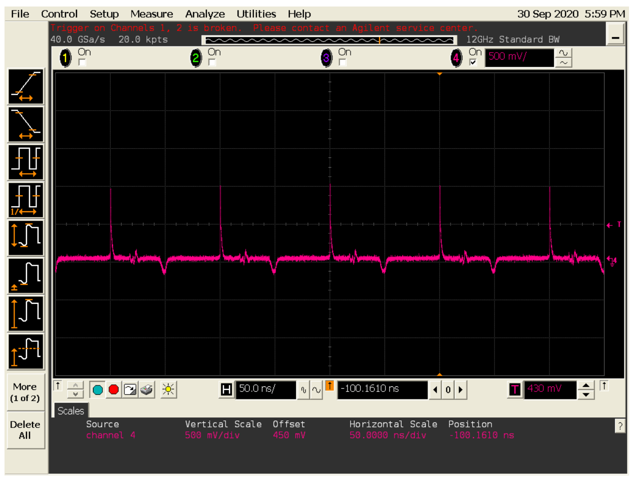

Fig. 3.31 Measured output of SRD circuit, driven by a 1 V peak-to-peak 50 Ω square wave.

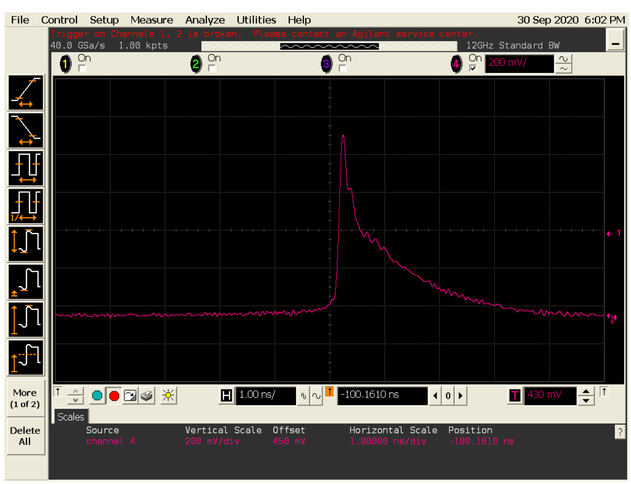

Fig. 3.32 Measured SRD output pulse at a 1 ns/div scale.

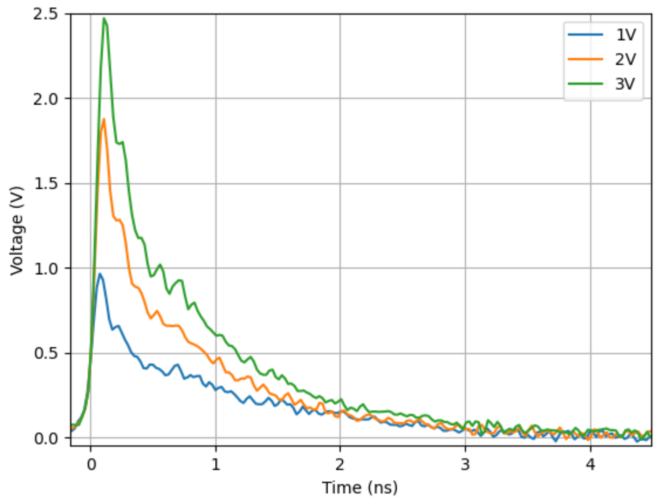

Fig. 3.33 Measured pulses, showing effect of ramping input peak-to-peak voltage. Plot created using waveforms extracted from oscilloscope.

Using the previously derived formula for harmonic content of a Gaussian, the 400 ps pulses will have a FWHM of 2.2 GHz and a 3 dB cutoff of approximately 1.1 GHz, below our desired range of 2-4 GHz. To improve the suitability of this pulse generator, evaluation with lower inductance could be pursued. The manufactured board is easily adjustable to accommodate such modifications. This concludes initial measurement and analysis of the SRD-based pulse generator.

3.8 Revision: Jitter Measurement of SRD and BJT Pulse Generators

The most challenging performance metric is jitter; it is difficult to model, and predict. NLTL-based comb generators are competitive despite their high cost, due to their very low additive jitter. The BJT and SRD experience similar noise generation mechanisms, both using the forward-negative transition of a p-n junction which suffers from shot-noise. The

BJT additionally uses a clock buffer (D-Latch) to drive the base. The latch has finite rise-time and is a potential entry-point for supply noise and EMI. These environmental and layout-dependent aspects cannot be fully captured by a standard SPICE simulator, and ultimately we must test the manufactured circuits.

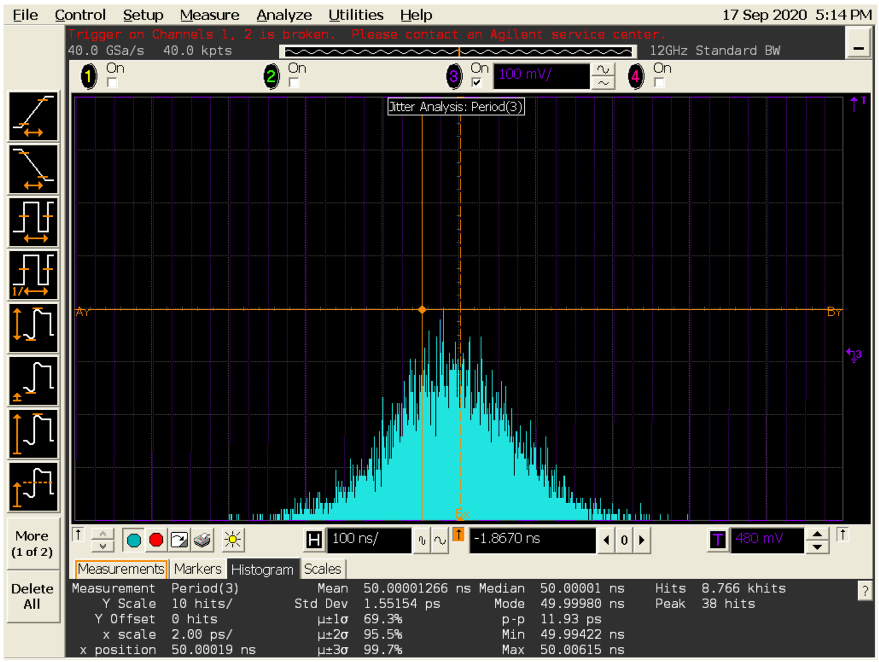

Fig. 3.34 Period measurement and histogram of input clock source.

To make measurements consistent between the two circuits, all measurements were made using an Agilent 81180A as the clock source. No clock pre-amplification is used with the SRD, which somewhat idealizes the results of the SRD. The jitter was measured using the period measurement feature of the Keysight/Agilent DSOX91604A. For the clock, SRD, and BJT circuits, we observe a jitter standard deviation of 1.55 ps, 2.04 ps, and 1.92 ps respectively, as shown in Fig. 3.34, 3.35, and 3.36. System jitter tolerance is limited to 100 ps, to allow sufficient time-domain resolution of a tumor on the order of a centimeter in size. These initial measurements show added jitter well below this budget, although there

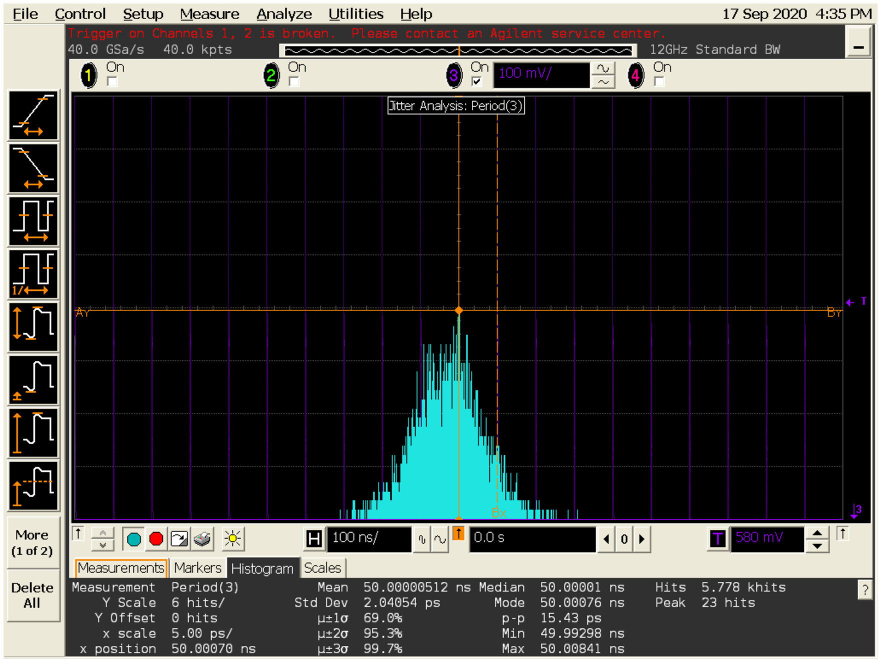

Fig. 3.35 Period measurement and histogram of SRD pulse generator.

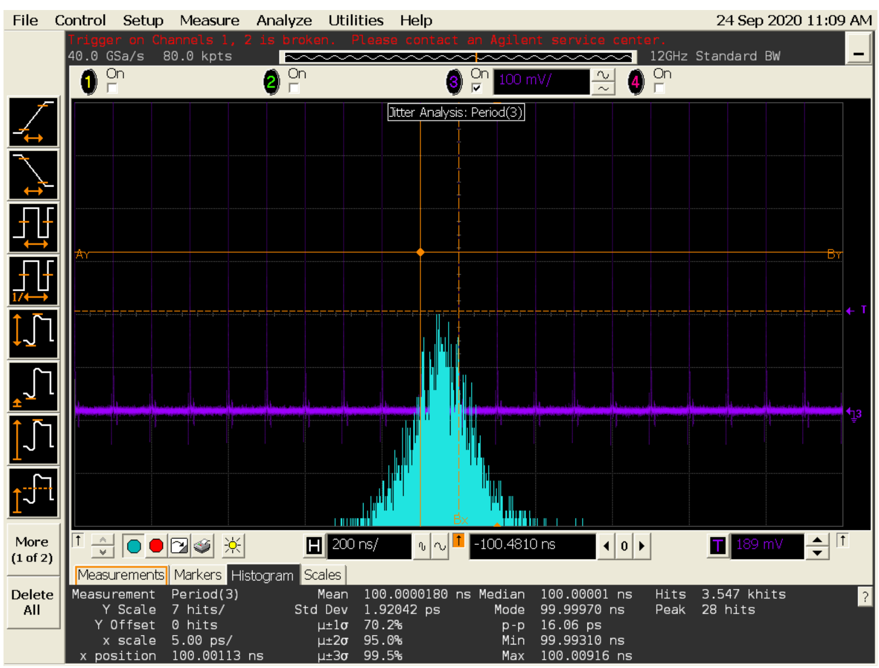

Fig. 3.36 Period measurement and histogram of BJT pulse generator.

are some reservations about these measurements.

Foremost, the oscilloscope used has a bandwidth of 12 GHz and 25 ps (40 GSPS) real-time resolution. We cannot expect this oscilloscope to provide definitive measurements more accurate than its own time-base. During measurement, the vertical scale of the oscilloscope was also observed to have a large effect on the measured period. By adjusting the vertical resolution, the period measurement can vary on the order of 10-20 ps. For consistency of measurements, the scale was adjusted for the minimum jitter for each circuit at measurement time, resulting in the poor waveform visibility in these reported jitter captures. For a definitive high-resolution measure of jitter for comparison with other comb generators, we require the higher sampling rate of an equivalent-time oscilloscope. However we can conclude that the jitter is tolerable for our application, and near the limit of what can be measured with this oscilloscope.

3.9 Revision: Concluding Remarks on Pulse Generator Design

Table 3.8 Measurement summary of the two pulse generators.

Circuit	Amplitude	FWHM	Jitter (period σ)
Clock	-	-	1.55 ps
SRD	0.9 V, 1.8 V, and 2.4 V[1]	400 ps	2.04 ps
BJT	1.1 V	150 ps	1.92 ps

[1] Values for 1 V, 2 V, and 3 V peak-to-peak input.

The designed pulse generators have demonstrated their applicability to coherent time-domain radar for breast-cancer detection systems. The BJT-based circuit presents the lowest cost, and is immediately manufacturable on FR4 substrates using readily available components. It also exhibited narrower pulse widths than the SRD-based circuit, although this comparison is limited. The SRD uses an inductor for differentiation while the BJT uses a shorted stub, and the clock-buffering stages are not consistent. The SRD circuit as implemented is below specification, and may warrant further experimentation with stub-based pulse shaping, varying inductor values, as well as with a controlled pre-amplification scheme to remove the rise-time and amplitude dependence discussed in the simulation section. The BJT-based circuit is already well-optimized for our system. For future work, the BJT-based circuit should be integrated as part of the clinical time-domain system, including testing with the current system clock, filter network, and power amplifier. These circuits offer drastically lower cost, with performance within specification for time-domain UWB breast-cancer detection.

3.10 Revision: CFA-based Pre-amplifier Simulation Results

3.10.1 Circuit Description

The goal of this circuit is to amplify the clock signal enough to drive the step-recovery diode circuit, without introducing jitter. The pre-amplifier uses a CFA in non-inverting feedback topology, with voltage gain of $A_v = 1 + \frac{R_f}{R_1}$. The feedback resistor R_f determines the stability of the circuit [41]. R_f is set to 1000 Ω based on recommendations from the manufacturer's datasheet. The trimming resistor can be adjusted from 0 Ω to 2k Ω, providing gain in the range of 1.5 to A_{CFA} (the maximum gain of the CFA). A_{CFA} corresponds to $R_1 = 0$, with the circuit acting as a comparator fully saturating the output range of the CFA.

3.10.2 Simulation

A simulation was undertaken using SPICE and manufacturer-provided THS3001 models. The simulation in Fig. 3.38 uses a 50 Ω source and input matching resistor, driving the

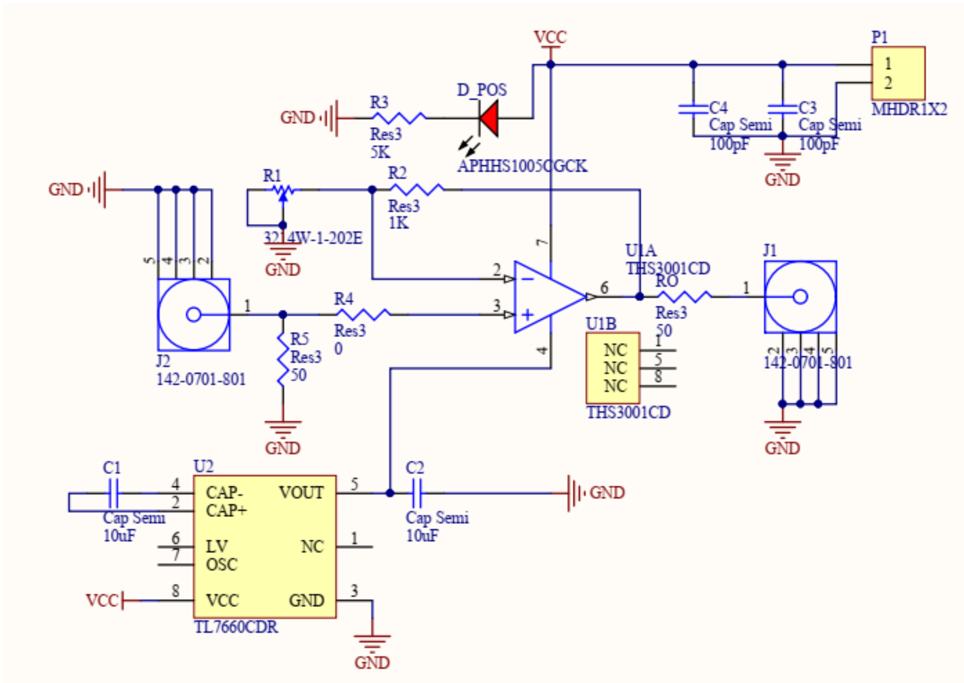

Fig. 3.37 Pre-amp schematic used in SPICE simulation.

circuit with a 1 V peak-to-peak square wave. The effect of sweeping R_1 is shown. Foremost, we see the CFA doesn't fully saturate to the $\pm$ 10 V supply, and only reaches $\pm$ 7.1 V. The slew-rate matches the expected 6.5 V/ns, and voltage gain at each R_1 value is as expected.

Active components and other additive noise sources in the circuit produce phase-noise through AM-PM conversion, proportional to the added noise and inversely proportional to the rise-time. The simulated output noise of the circuit with $R_1 = 0$ is shown in Fig. 3.39, and the corresponding integrated noise is 4.176 mV RMS. With this rise-time and noise voltage, we expect a zero-crossing variation of 0.642 ps RMS.

From the measurements shown in Fig. 3.40 and 3.41 it clear why this clock buffer introduces jitter to the step-recovery diode circuit. This period jitter is 100 ps RMS, but the buffer also introduces duty-cycle variation of 500 ps RMS. The step-recovery diode switching point occurs at the forward-reverse transition, which will vary widely with duty-

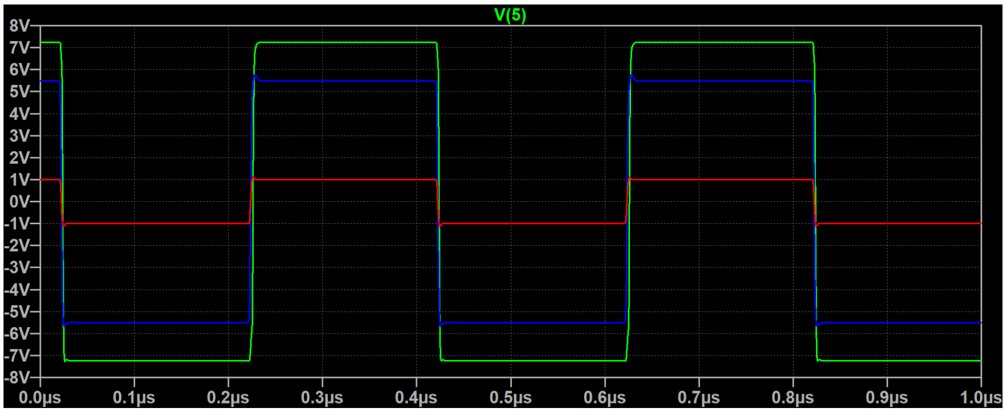

Fig. 3.38 SPICE simulation of CFA-based pre-amplifier circuit with trimpot R_1 set to 0 (green), 100 (blue), and 1000 (red).

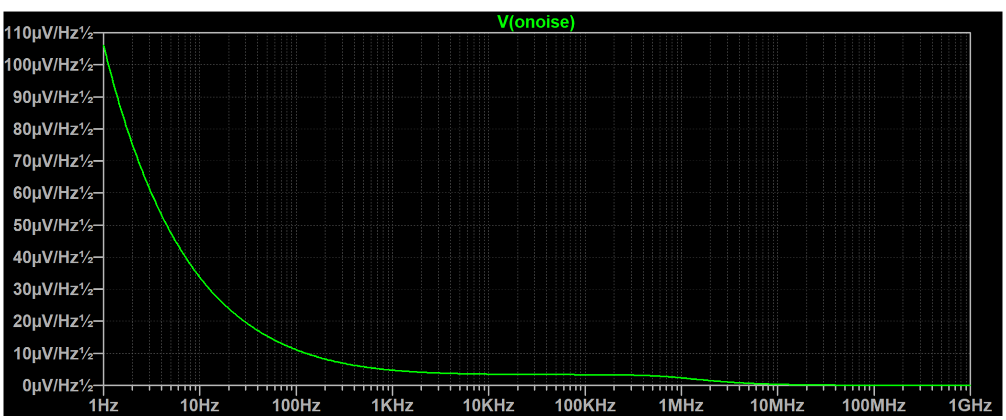

Fig. 3.39 Simulated output noise of the populated CFA circuit, with the trimpot set for maximum gain.

cycle variation. We conclude the additional phase-noise must have been introduced by layout, supply noise, and other environmental factors. An inverter IC was used in the design, which allows the use of a single supply, but it may be poorly regulated and modulating the power terminals of the CFA. To confirm this, measurements of the CFA buffer were taken, this time directly powering the negative terminal rather than using the inverter IC. With a reliable negative power supply, the CFA no longer exhibits the wide variation in duty cycle.

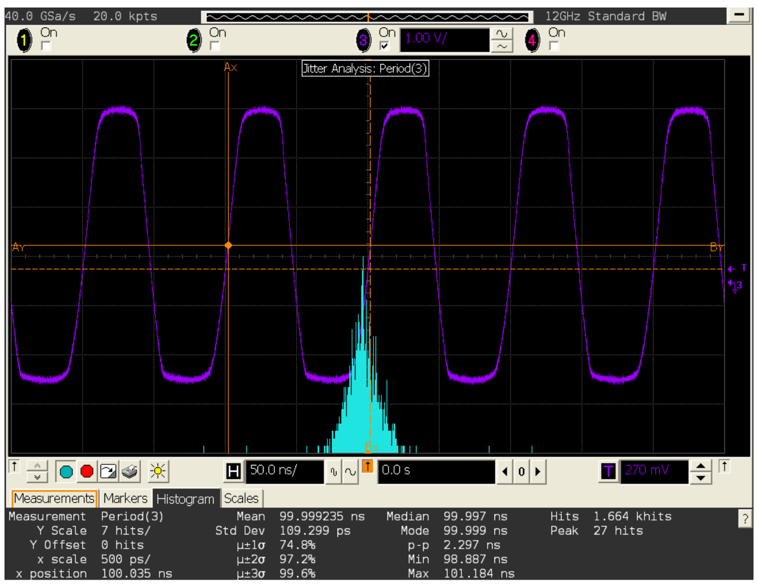

Fig. 3.40 Measured period jitter of the CFA pre-amplifier.

3.10.3 Conclusion

The simulation of this circuit demonstrates its applicability as a high-performance fast-rise clock buffer, but the use of an inverter as a power supply introduced excessive jitter. This CFA circuit is functional in principle and in practice, as long as regulated dual-power supplies are used. For a low-phase noise SRD impulse generator, an alternative power-supply scheme or driving circuit would be needed. A single-supply feedback amplifier, or a latch circuit could provide the needed driving amplitudes. This was explored during design of

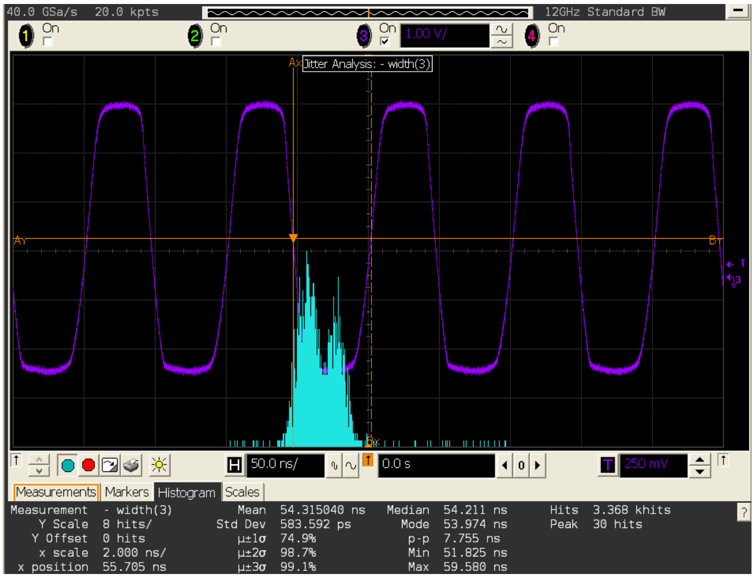

Fig. 3.41 Measured clock pulse-width, showing 500 ps RMS variation between the rising and falling edges.

the BJT pulse-generating circuit, which uses a simple D-latch to provide 3.3 V steps with a rise-time of a few nanoseconds.

Chapter 4

Receivers for Time-Domain UWB Radar

4.1 Introduction

In this chapter, we address the choice of a suitable receiver to digitize UWB time-domain pulses. An overview of the desired performance is presented in Table 4.1. First we briefly discuss analog-to-digital converter (ADC) topologies that can operate at high speeds. Since real-time ADCs are expensive at 6 GHz a better approach is to use an equivalent-time sampling (ETS) scheme. This allows sampling at the system clock rate, on the order of 10 megasamples per second (MSPS) to 100 MSPS, rather than the Nyquist rate of at least 8 GSPS. To implement ETS, we need a wide-bandwidth sampler and precise timing circuits. We will discuss some of the approaches here in a literature review. The final section provides two recommended designs for implementing time-domain radar at low-cost and with good performance; (1) a comparator-based sampling circuit and a (2) Schottky diode-based sampler, both using standard PCB manufacturing.

Parameter	Design Goal
Input Bandwidth	>6 GHz
Input 1 dB Compression Point	>10 dBm
Jitter	<100 ps RMS
Input Voltage Range	-30 to 10 dBm
Clock Source	50Ω AC Coupled CMOS Clock
Output Signal Bandwidth	<100 MHz

Table 4.1 Desired performance of sampling circuit.

4.2 Equivalent Time Sampling Approach

To observe high-frequency repetitive signals, an ETS approach is used. This type of receiver is already used in the system, as the Picoscope 9200 operates in this manner. It has an input bandwidth of 14 GHz, above our needs, and can operate at equivalent-time sample rates up to 2.5 TSPS. The goal is to reduce the cost by implementing it discretely at a lower bandwidth of 6 GHz.

An UWB radar output signal in the time domain is a series of wide-band pulses defined by:

$$x(t) = p(t) * \delta_{PRR}(t) \tag{4.1}$$

where $p(t)$ is the pulse shape, $\delta_{PRR}(t)$ is the comb function at the pulse-repetition rate, and $*$ is the convolution operator. We can use the periodic nature of the overall signal, to reconstruct $p(t)$. Rather than digitize in real-time, we sample only a piece of the waveform on each pulse. By offsetting the sample point very slightly, we can reconstruct the shape of the fast changing envelope. This known as equivalent time sampling, and is depicted in Fig. 4.1. The resulting sampled waveform is:

$$y(t) = [p(t) * \delta_{PRR}(t)] \cdot \delta_S(t) = p(t\frac{\tau_S - \tau_{PRR}}{\tau_S}) \cdot \delta_S(t) \tag{4.2}$$

where δ_S is a comb function at the sampling rate, τ_{PRR} is the pulse repetition period, and τ_S is the sampling period. The quantity $\Delta\tau = (\tau_S - \tau_{PRR})$ is the equivalent time sampling rate, which relates the actual sampling rate τ_S, to the envelope of the sampled waveform by $y(N\tau_S) = p(N\Delta\tau)$. This can also be interpreted as a mixing process, where the harmonics of the pulse series are down-converted by the sampling comb. Because the spectrum of the signal in 4.1 is sparse, we can compress it by mixing it with another comb. Essentially, a sampler is using down-conversion mixing, sometimes called *subsampling*.

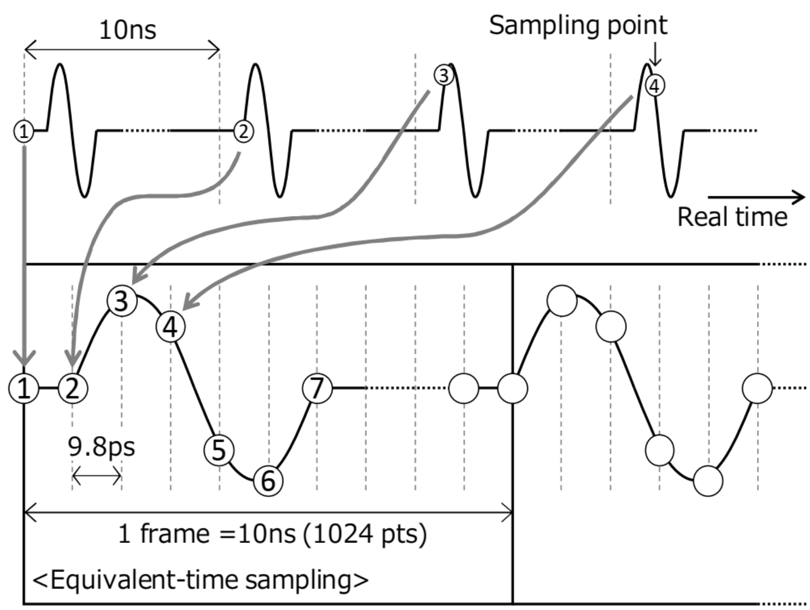

Fig. 4.1 Depiction of an equivalent-time sampling scheme, adapted from [7].

Physically realized combs have some finite duration, which limits the highest harmonic content they can sample. Realizing the narrow sampling aperture needed for ETS can be a challenge. Further, we need low jitter in the pulse clock and sample clock. Jitter will cause a variation in the amplitude of the down-converted signal. This reduces the SNR of the receiver. Ideally, jitter would be smaller than or on the same order as $\Delta\tau$, which would be roughly 100 ps at a Nyquist rate of 10 GSPS.

4.3 Generation of a Time-base

A conventional method of generating a time-base in microwave sampling is using a precise reference phase-locked loop, providing two frequencies. One clock drives the pulse producing circuit, while the other at a slight offset drives the sampler clock. Fortunately, phase-locked loops with fractional division and multiple outputs are readily available on IC as commercial products at a low cost. This can also be implemented using programmable delay-lines, another readily available integrated circuit. The delay line can share the same clock as the pulse-repetition clock, which allows fully synchronous control of the sampling location.

4.4 Conventional ADCs

In addition to sampling the signal, we must also digitize it. The ADCs most relevant for high-speed applications are flash ADCs, successive-approximation register (SAR) ADCs, and pipelined ADCs [8]. A flash ADC uses an array of comparators, with each comparator fed by the signal and a reference level as shown in Fig. 4.2. The signal is instantaneously digitized when the comparators are latched. This topology provides the fastest conversion. In a SAR ADC, a single comparator is used, with the reference fed back by a DAC as shown in Fig. 4.3. The DAC is set by a register which stores the current approximation of the input, gradually determining the input voltage through a number of comparisons. This circuit requires multiple clock cycles to finish conversion, and needs a sample-and-hold (S&H) circuit to keep the sampled voltage constant. A S&H circuit has a wide input bandwidth, and will hold a high-frequency signal for some duration, allowing it to be sampled and converted by a slower ADC. A pipelined ADC converts the incoming signal in a series of stages. The first stage will digitize the higher bits, with the remainder being subtracted and amplified. Subsequent stages will repeat this process of quantization, subtraction and amplification.

This is a popular fast topology in high-performace fast ADCs, able to reach over 100 MHz.

Unfortunately, none of these topologies offer inherently wide bandwidths, as it is generally determined by the input S&H stage. In general, they are not designed for wide-input bandwidth, with a bandwidth typically ranging from half to twice the sampling rate. However, wide input bandwidth comparators are available, providing effectively a 1-bit Flash ADC. Another option is adding an external S&H or track-and-hold amplifier (THA) circuit at the input of an ADC. Some sample-and-hold circuits are available off-the-shelf. Sampling-heads, implemented with sampling diodes on a hybrid MIC, can also be used.

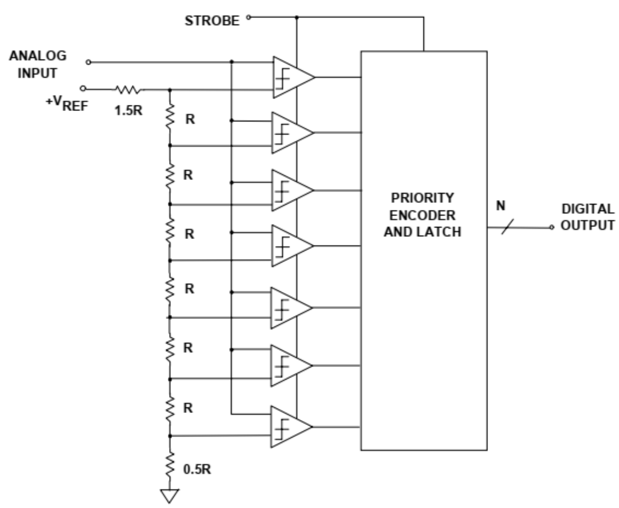

Fig. 4.2 Flash ADC [8]

4.5 Review of ETS Sampling Receivers

The main approaches used to implement time-domain receiving and sampling for radar systems are, in brief:

1. Schottky-based sampling heads on hybrid [9] [42] [11] [10];

2. Custom integrated circuits [4] [7];

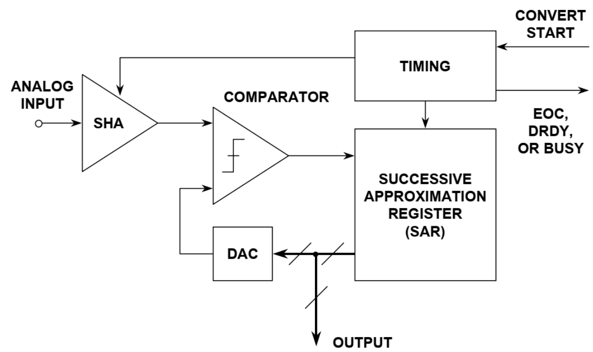

Fig. 4.3 SAR ADC [8]

3. COTS Comparator-based sampling [12];

4. COTS RF ADCs (with options for external THA) [43] [44].

While custom ICs are mentioned, they are not applicable for our low-cost hybrid design unless they are available as a COTS product. These approaches will be elaborated in the following subsections.

4.5.1 Schottky diode sampling

An RF sampling circuit utilizing the fast switching time of the Schottky diode junction is shown in Fig. 4.4. This circuit was presented in 1966, when the state-of-the art for microwave sampling was only at 4 GHz [9]. Currently, approaches using integrated Schottky diodes have achieved sampling rates over 200 GHz [4]. In this section we will discuss the design of such circuits, and a few low-cost implementations that have shown good performance up to 6 GHz.

Schottky diodes are able to switch quickly from forward to reverse bias, allowing their application as high frequency mixers and samplers. In a PN-junction, during forward conduction charge is stored due to minority carrier diffusion. In the Schottky metal-semiconductor junction there are no minority carriers to prevent instantaneous changes in current. Depletion capacitance is still present under reverse-bias, but is much weaker than diffusion,

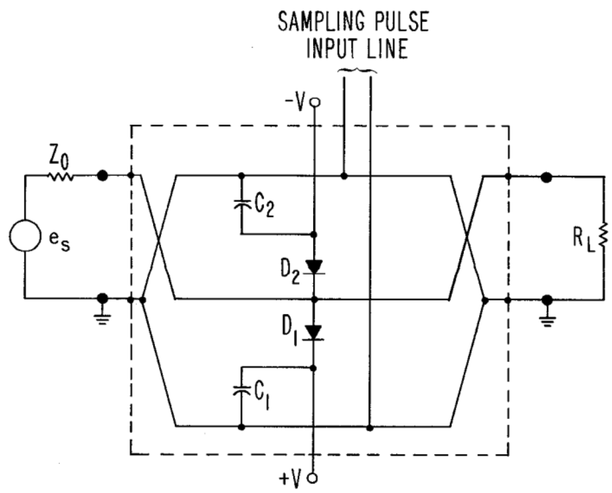

Fig. 4.4 Diode-based RF sampling as described in [9]. The sampled pulse is observed across -V amd +V.

and can be mitigated by reducing the junction area. This leaves package capacitance as the largest source of parasitic capacitance. This feature allows the Schottky junction to switch very rapidly. The diode is a two-port device, so an additional port must be introduced to operate as a switch. For a sampler, this can be achieved by having the output and strobing pulse share one port, with the output taken differentially, as in [9].

The circuit operates as follows. Two Schottky junctions are connected in series to a point on a transmission line. A balanced pair of sampling pulses (equal and opposite sign) drive the diodes through an RF sampling capacitor. Both diodes are momentarily forward biased. The input signal will briefly charge the RF sampling capacitors. The output pulse can then be observed across capacitors C_1 and C_2 at the points marked -V and +V in Fig. 4.4. The sampled output is effectively baseband, and can be measured with conventional circuitry. The strobe applied to these samplers may be rising steps rather than pulses, which are differentiated using a balun. The performance is sensitive to this balun, as it must operate at high-frequencies and provide a balanced output.

Grove's design, [9], achieved a 12.4 GHz bandwidth implemented using a biconical cavity. More modern approaches using planar circuits have been designed subsequently. In [42], a 20 GHz planar sampler is implemented on a quartz thin-film hybrid MIC. This design implements the balanced differentiating balun by a slotline coupled to the microstrip which receives the strobe input. The cost of this implementation is somewhat high due to the use of thin-film manufacturing. Lower cost designs have been proposed in [11] and [10].

In [10], the balun is implemented using a magic-T microstrip on FR-4 substrate. The design uses an SRD driven by the local-oscillator to drive the magic-T which switches the sampling bridge, as shown in Fig. 4.5. The design is able to receive pulses of 500 ps in width, although the receiver bandwidth, jitter, or dynamic range is not reported. In [11] the need for the balun is removed by using a single-ended diode rather than a pair, as shown in Fig. 4.6. They report an input dynamic range of -43dBm to -1 dBm and a bandwidth of 6.4 GHz. Although jitter measurements are not provided, the system achieves millimeter accuracy in a 2-D imaging scenario.

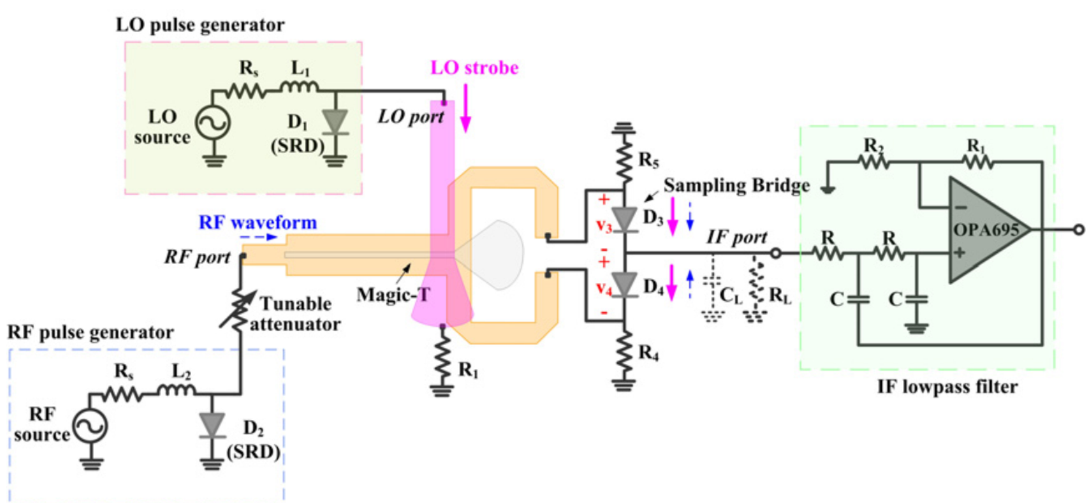

Fig. 4.5 Sampler implemented on PCB from [10]. Design features a magic-T balun which drives a balanced pair of sampling diodes. Implemented on PCB.

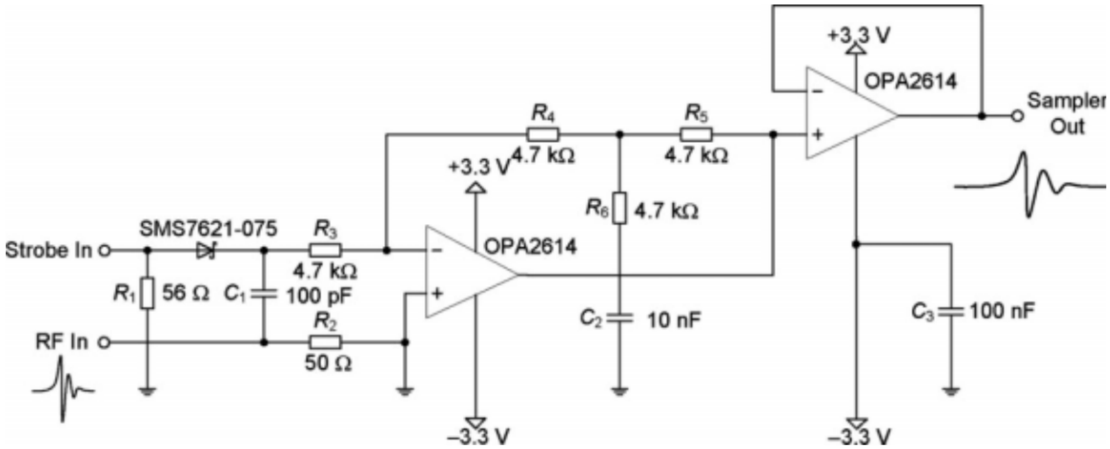

Fig. 4.6 Sampler implemented on PCB from [11]. Design uses a single-ended Schottky diode to eliminate the need for a balun. Implemented on PCB.

4.5.2 Comparator-based Sampling Receivers

Designs for RF sampling based on high-performance comparators have been implemented [12]. In [12], a wideband latched comparator is designed on IC for what the authors call a *sampling waveform analyzer* (SWA), which is effectively a microwave sampling oscilloscope. A schematic of the circuit is shown in Fig. 4.7. The conversion approach is similar to that of a SAR ADC, but using an ETS timebase. The output of the comparator is latched, which allows a low speed readout of the comparison. The comparator determines the critical RF performance such as dynamic-range, bandwidth, jitter, and noise. In this case, a 5 GHz comparator was used. The timebase can be provided by a digitally controlled delay-line, with the successive approximation from DAC fed into the comparator also being digitally controlled. This design was successfully applied to the measurement of pulses, with rise-times as low as 63 ps.

Fortunately, many RF comparators are available as COTS components. The HMC675 series features a 10 GHz input bandwidth, and is available at low cost [45]. Designing around such a comparator would allow sampling of high-frequency signals, using only standard PCB processes and components. One drawback to this design is the slow conversion time because it requires a number of comparisons to acquire a full sample. The trade-off between conversion time and accuracy could be explored further, and optimized for our application.

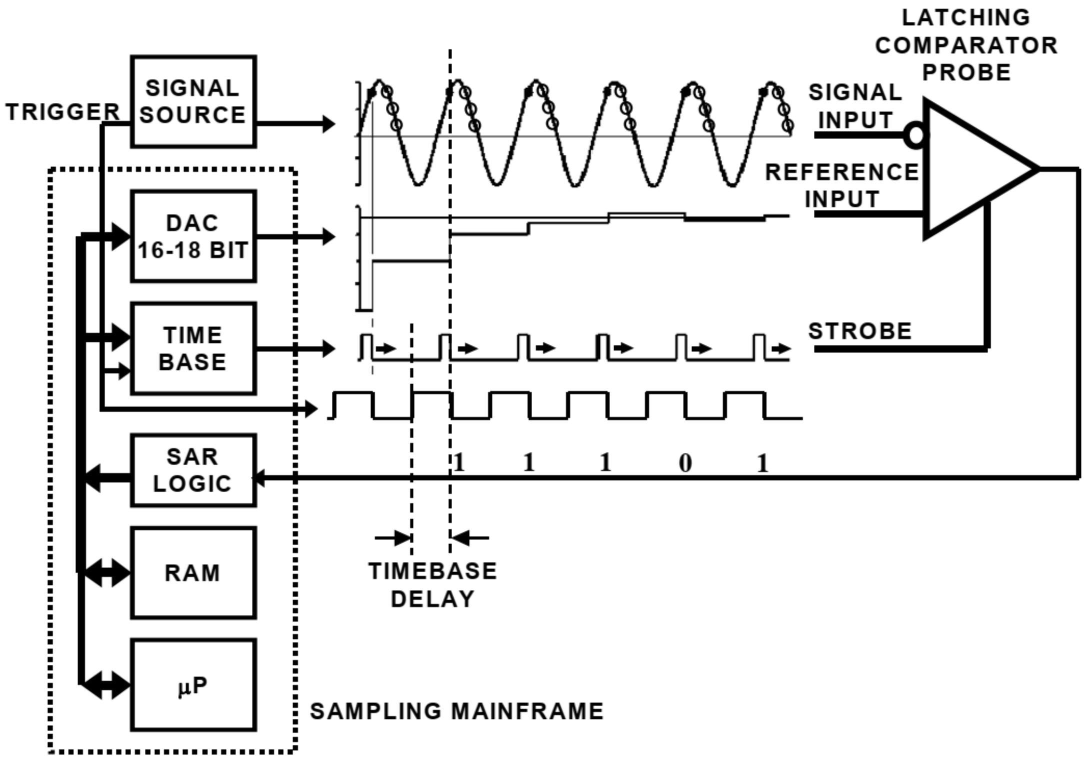

Fig. 4.7 NIST sampler using wideband comparator [12]. Implemented on PCB.

4.5.3 COTS RF ADC Implementations

Another COTS solution to ETS is the use of high-frequency ADCs and potentially a track-and-hold (THA) amplifier. In [43] an UWB system is realized using a single ADC as a receiver in an equivalent-time sampling scheme. The radar system uses a 300 ps pulse, which is mixed to a 8 GHz center frequency. The receiver downconverts the pulse back to baseband, and then samples it using a 1.4 GHz bandwidth COTS ADC (ADC16DV160) in

ETS mode. The input pulse has content beyond this bandwidth limitation, but the system is able to resolve the pulses. Using a single COTS ADCs in ETS mode is expensive beyond a few GHz, and this design shows a very cost-effective use of an RF ADC. Since our system bandwidth is somewhat higher, the attenuation due to the ADC bandwidth is likely to reduce performance below our required specification. It would also require additional components, if we attempt to lower the bandwidth by downconverting around our center frequency of 3 GHz.

To expand the bandwidth of a COTS ADC, there are THAs designed on MMIC. In [44], time-domain a microwave breast cancer detection system is designed, using a HMC660 THA and ADS41B29 ADC. The timebase for ETS is provided by a multi-phase frequency synthesizer. The system demonstrated effective imaging results comparable to VNA measurements. The system depends on several high-cost products in the system, including the THA, but the overall system is less expensive than a VNA or COTS time-domain instruments such as the Picoscope 9200.

4.6 Discussion

Based on this review, there are low cost options for implementing time-domain radar systems up to the range of 6 GHz. The most promising options are (1) a Schottky diode based sampling head, and (2) an RF comparator based sampler. Schottky diodes offer the lowest cost, while the RF comparator offers the reliable performance of a COTS comparator. Neither design has been applied to the problem of low-cost microwave breast cancer detection, with both offering unprecedented value.

It remains to be seen how well they will perform in a low-jitter coherent system, as decluttering signals may be more challenging without use of the high-performance Picoscope

9200. Calibration and reliability of measurement is also a factor in custom-designed solutions. Overall, the designs promise to reduce cost by many orders of magnitude but application to breast cancer detection has not been attempted.

4.7 Conclusion

This chapter has presented several approaches to receiving UWB signals, with emphasis on low-cost methods. While implementing these receivers on ICs has been proposed, it increases the cost of the system. Using COTS components provides many options for operating at microwave frequencies, but require further work in implementation, calibration, and test. Developing these receivers would reduce the cost of the system substantially and allow smaller form factor.

Chapter 5

A Flexible Switching Matrix and Antenna Array

5.1 Introduction

This chapter describes the analysis and testing of a flexible printed-circuit board containing switching and antenna elements integrated onto a single board. The board under evaluation was designed and manufactured under supervision of Dr. Josh Schwartz at Trinity University. The hardware development project was undertaken with knowledge of the project requirements, but without active consultation and testing for its intended use. This work presents that testing. Due to the lack of insertable test points, the design was tested directly in a breast-cancer detection scenario.

This type of board was previously evaluated in [16], but suffered some drawbacks, notably a large amount of control lines.The next iteration of the board introduced a shift-register to control the switch settings, a new flexible substrate (Pyralux), and a new antenna design. This board integrates both the antenna and switching elements, allowing an overall 2x16 (2-

pole, 16-throw) switching functionality for a total of 240 unique S_{21} channels. Measurements are presented in this chapter, documenting the incremental testing of the board for clinical use in microwave-based breast cancer detection. First, initial testing of the DC control and connectivity of the board was performed. The RF performance was evaluated using phantoms mimicking breast tissue in the range of 2-4 GHz. Tumor reflections in the time-domain were successfully measured using the new prototype. Further testing with DMAS was unsuccessful, indicating that many of the channels are defective and need correction to produce images comparable to the existing clinical system. Recommendations to improve the design in a future iteration are presented in the conclusion.

The design rationale for the array is to integrate the switches and antenna into a single substrate which reduces the overall cost. The material used in the new prototype is Pyralux AP8545R, rather than Rogers UltraLAM 3850 in [16]. This material has similar RF performance, but has has more flexibility and can be incorporated into a 4-layer design. The number of layers in the board was reduced from 6 to 4, to improve board flexibility. The design incorporates a shift-register to reduce the number of control lines. The board needs only a single DC port to control the shift-register controls, and provide DC power; this allows a reduction in form factor and number of control lines. The RF connection is provided by 2 SMA-connectors, one for transmit and one for receive. The board must provide transmission UWB pulses in the range of 2-6 GHz at approximately 33 dBm on 50 Ω matched lines. The rationale for integration is reducing the costs by omitting connectors and SMA cables which raise cost and lower performance. The shift-register is controlled via an STM32 MCU, and synchronized with the time-domain oscilloscope with a Python library. The device under test is shown in Fig. 5.1.

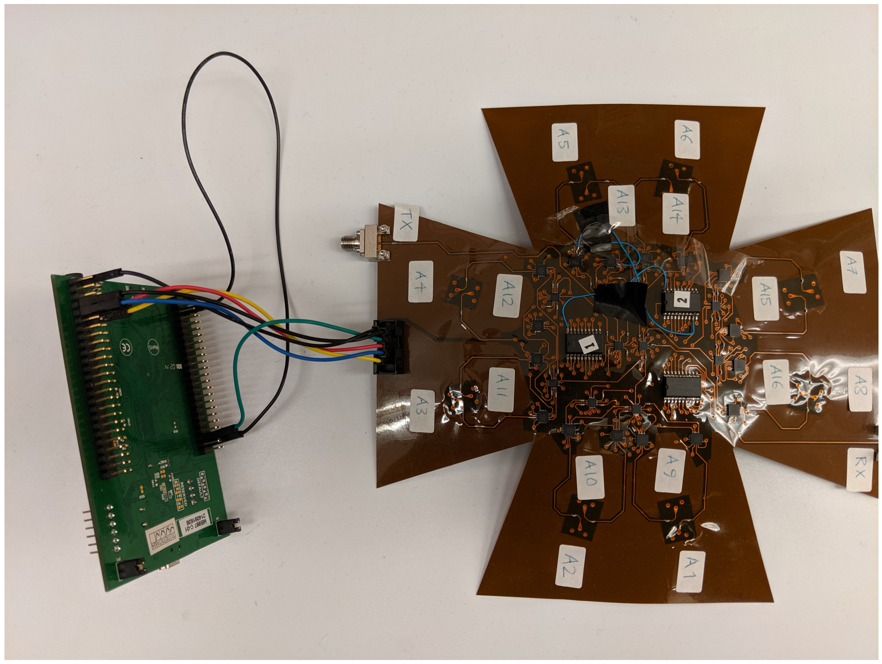

Fig. 5.1 The flattened flexible antenna array showing to the MCU and antenna numbering. The Maltese cross shape allows the array to better conform to curved surfaces.

5.2 Initial Testing

Initial testing consisted of validating the correct DC power and control. Due to the lack of LED indication on the board this is a manual process. There are a total of ten 1x4 switches (2 bits each) and 16 1x2 switches, leading to a total of 36 DC control lines. The control lines are provided by a shift-register, implemented using three Nexperia HEF4894B in a daisy-chain. After transmitting a serial command to the MCU via a Python library, the MCU will shift in the data to the correct control word. The settings were manually tested for a number of control words, proving to be accurate, and assumed to be correct for all 240 possible settings. Each integrated circuit on the board was also tested to have secure connections to DC and power.

The next step was to validate RF performance. The antennas embedded in the array are microstrip patch antennas, as described in [23]. These are designed for a 50 Ω impedance match when in contact with breast tissue, which consists mostly of fat tissue with dielectric permittivity ranging from 7 to 11 ϵ_r. The system must for that reason be evaluated in contact with a tissue volume, rather than open air. The initial phantom testing proceeded as follows. The flexible switching matrix was secured in contact with a carbon rubber phantom, with the prototype folder around the phantom. The phantom has a cylindrical hole where rubber plugs can be placed. This allows observation of varying the dielectric materials in the plug area. First, a rubber plug is placed such that the antennas observe a homogeneous medium. In this configuration, each channel is measured in the time-domain, leading to a total of 240 signals. The system used to transmit and receive UWB signals is shown in Fig. 2.6. The time-domain waveforms are acquired at 200 GSPS through a 14 GHz bandwidth oscilloscope, and an average of 16 time-domain samples are used during acquisition. This process is repeated with the introduction of a plug with a 1 cm diameter tumor, as well as a metallic plug. The three phantom and plug combinations are depicted in Fig. 5.2. By aligning and subtracting the null baseline scan from the scans with a target present, we can isolate the target response. This simple test allows us to evaluate whether the antenna can receive a response due to the reflection from the internal target.

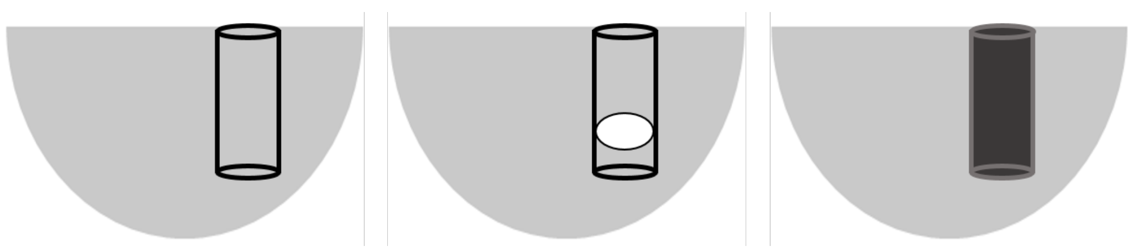

Fig. 5.2 Three phantom and plug combinations used for initial testing. (Left) The baseline case consisting of consistent dielectric permittivity. (Center) A plug with a 1 cm tumor with ϵ_r of 40. (Right) A fully metallic plug.

Three baselines scans (B1, B2, and B3) and three tumor scans (T1, T2, T3) as well as one metal plug scan were acquired. The overall mean-energy difference (MED) metric

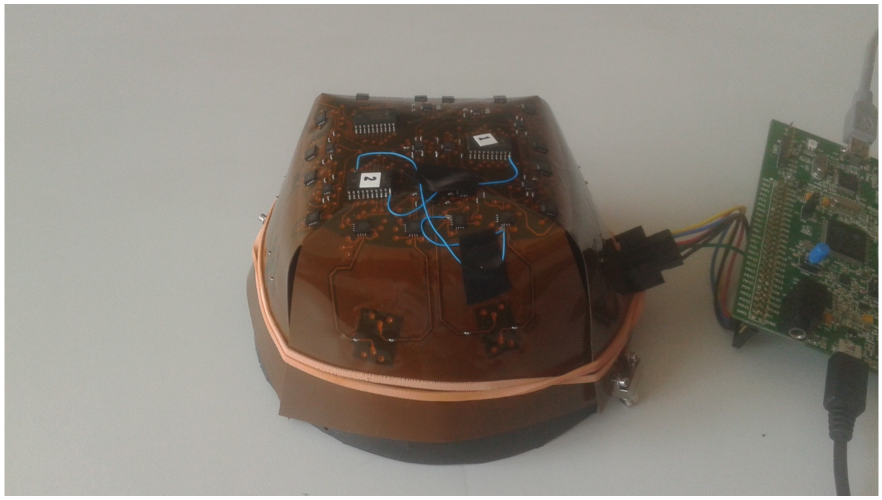

Fig. 5.3 Flexible antenna array in direct contact with carbon-rubber phantoms.

was applied using each combination of these datasets. In this case, after alignment and subtraction, the MED is computed as simply the sum of the voltage magnitude:

$$MED = \sum_{i}^{N} |x_i|^2 \tag{5.1}$$

where x_i is the decluttered, sampled, time-domain signal. The ten highest channels out of the 240 total were averaged to quantify the overall energy difference of the scan compared to the baseline. This is summarized in Table. 5.1. Further, these high-energy difference signals can be plotted to visualize the reflections.

The isolated reflections are shown in Fig 5.4 and Fig. 5.5. These demonstrate the successful detection of our target within the received signals. The shape of the reflected pulse appears as a linear reflection of the transmitted envelope. Not all channels are able to detect the reflection. This may be due to a defect in the transmission lines, or due to the channel position causing high attenuation due to the phantom tissue, which is expected behavior. The worst-case false-positive reflection created by subtracting all combinations of baseline-baseline pairs and finding the largest amplitude is shown in Fig 5.6. This shows the worst case signal in terms of power caused by motion artifacts in the system. Unlike the tumor reflections, the shape is not a linear transformation of our transmitted pulse. This is promising performance, as the reflections are discernible from motion artefacts.

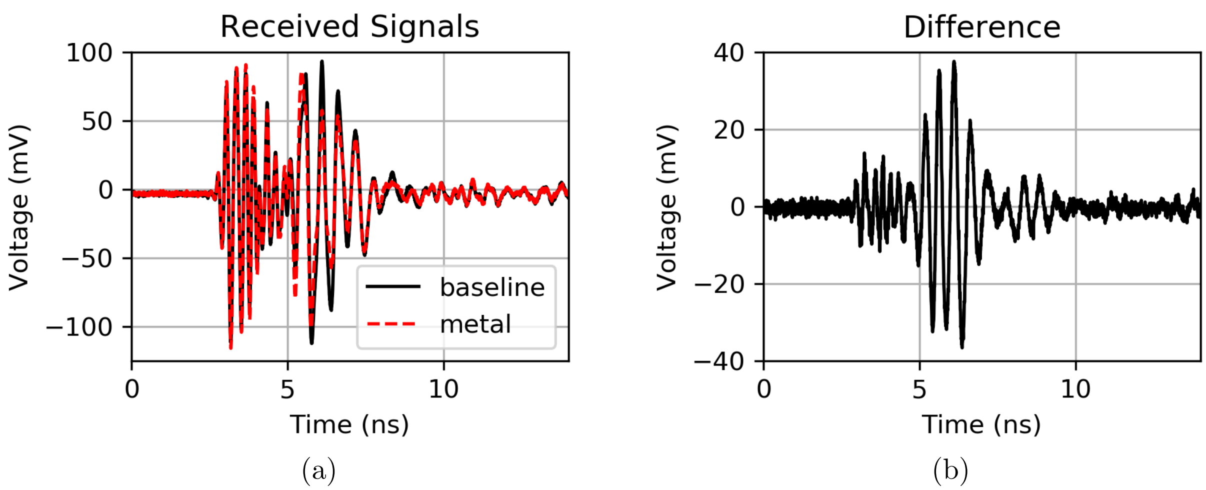

Fig. 5.4 Time-domain signals of sample antenna pair of (a) baseline and metallic object and (b) response due to object.

This testing was successful in demonstrating the transmission and receiving of UWB pulses through the flexible switching matrix. It also revealed a number of problems with the board. We note a variation in the reciprocal pairs; transmission between antenna A to B should produce an identical response from B to A. Ideally, there would be no variation, because the antenna-channels, transmission-lines, and switches are reciprocal. This presents a challenge as we need to correct for each channel individually in terms of delay, magnitude, and crosstalk. It is suspected that some transmission lines between switching elements are defective, causing crosstalk, mismatch, and attenuation. The integrated nature of the board makes it difficult to identify the defective traces.

The dataset also shows crosstalk. In Figures 5.5 5.4 and 5.6, there is an early portion of

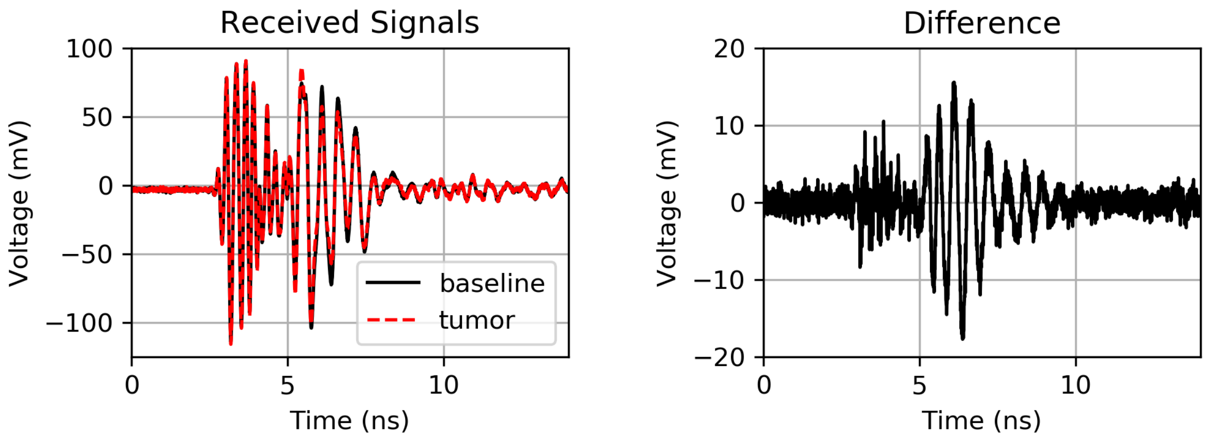

(a) (b)

Fig. 5.5 Time-domain signals of sample antenna pair of (a) baseline and tumor and (b) tumor response.

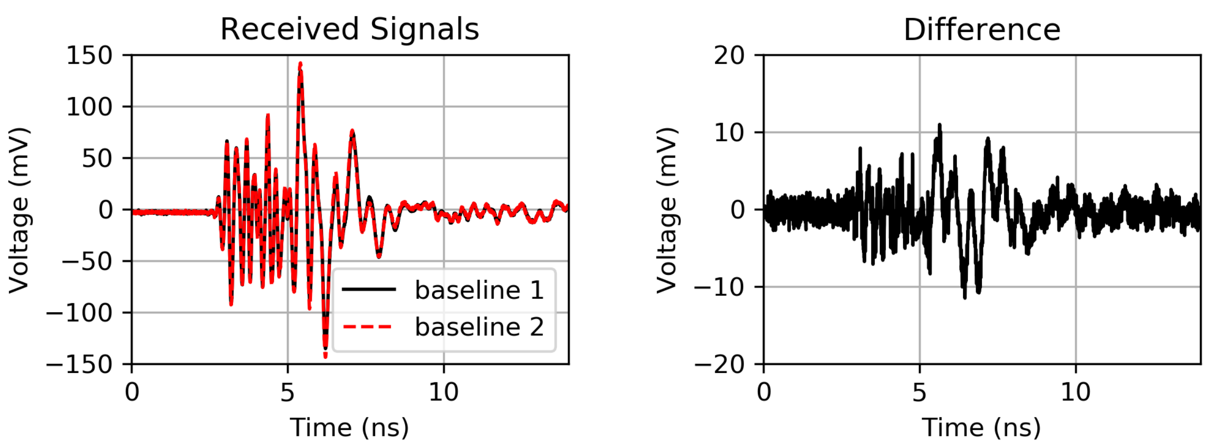

(a) (b)

Fig. 5.6 Time-domain signals of sample antenna pair of (a) B1 and B2 and (b) difference between both baseline scans. This channel was the worst-case of the baseline-baseline test, which should ideally have no power after subtraction.

Table 5.1 Mean Energy of Difference of Top 10 Highest Energy Difference Channels

Scan 1	Scan 2	MED
B1	B2	1.2
B1	B3	2.0
B2	B3	0.95
B1	T1	4.5
B1	T2	4.9
B1	T3	5.0
B2	T1	3.9
B2	T2	4.1
B2	T3	4.4
B3	T1	3.6
B3	T2	3.7
B3	T3	3.7

the signal that does not vary in time between channels, but does vary in shape and amplitude. This signal does not radiate through the antenna, and provides no useful information about the target. Crosstalk is caused by radiative elements in the switching network, such as the fields produced by the microstrip traces. Variation in manufacturing can cause the microstrip to be more radiative than it was predicted to be. Since no preceding study of transmission lines printed on Pyralux substrate was reported, we have no measurements for EM performance of the microstrip. Some of this crosstalk can be removed by decluttering with subtraction or some other signal processing technique. It can also be removed by time-gating out the crosstalk portion. Unfortunately the crosstalk persists into the time-window of interest. This problem impedes our detection capability. Due to the lack of test points, it is difficult to determine where the crosstalk is occurring in the multi-segment board.

Another design issue is the variability in channel gain, each channel presents a unique S_{21} path. This can be observed from channels of similar orientation and observing direct signal transmission. In terms of detection, this means any normalization scheme would need to be applied on a per-channel basis. It also complicates imaging as different regions have different delay and varying signal power.

5.3 Imaging Testing and Comparison with Present System

Following the simple metal target-testing with the flexible board, a comparison between the existing rigid board, and the flexible board was performed. The phantom used is again a no-skin uniformly homogeneous tissue phantom representing fat with removable plug, with a relative permittivity of 8.0. A series of baseline and tumor scans was performed with replacement of the plug each time to get a sample of motion artefacts. This was repeated with the flexible switching matrix and the static antenna radome. The static switching matrix provides comparison for the new prototype. The two antenna arrays can be oriented with the phantom so that the antennas are approximately in the same position, and directly comparable in the time-domain.

From this experiment the two systems produce very different response for the same channel. This is due to the variability in S_{21} and crosstalk in the flexible board. Several example channels are displayed in Figs. 5.7, 5.8, and 5.9. Due to the reduction in total wiring, the flexible board signals are received earlier in time. In some channels, such as in Fig. 5.8, the flexible board reads a higher amplitude signal than the non-integrated system. Less attenuation is desirable. However in other cases, such as in Fig. 5.9, there is more attenuation.

The MED and DMAS images were used as performance metrics. For both systems, MED baseline-baseline subtraction is higher or comparable to the baseline-tumor cases. This is problematic for both systems; the purpose is to evaluate how well the flexible board works for detection. Since this metric showed similar performance, DMAS imaging was performed.

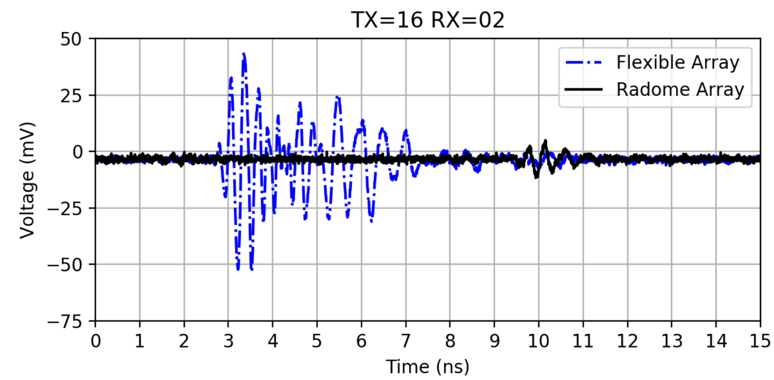

Fig. 5.7 Comparison in the time-domain of sample signal showing high crosstalk in the flexible board.

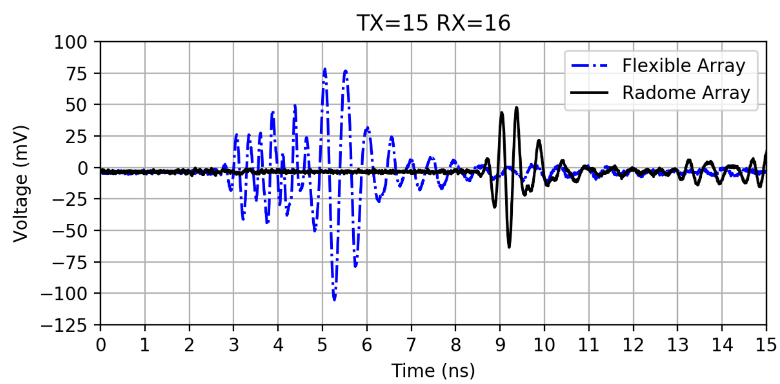

Fig. 5.8 Comparison in the time-domain of sample signal showing higher amplitude transmission received by the flexible board.

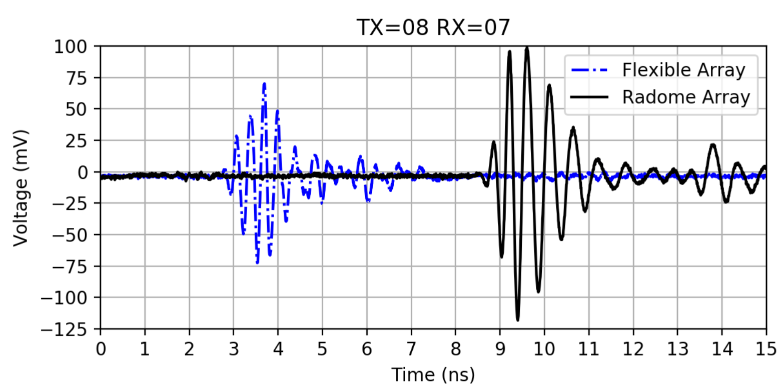

Fig. 5.9 Comparison in the time-domain of sample signal showing lower amplitude transmission received by the flexible board.

The images are shown in Figs. 5.10 and 5.11. These images show the magnitude in dB of a single cross-section of the overall 14 cm x 14 cm x 7 cm volume, where the tumor target was expected. Specifically the cross-sections shown are 4.6 cm away from the flat portion of the hemispherical phantom. In the radome switching matrix, it is clearly delineated. For the flexible board, the image is blurry with no target distinction from the background. The results do not show anything meaningful about the tumor reflection. This process was repeated for each combination of baseline and tumor, resulting in images of similar quality for both the flexible board and the radome. This demonstrates the difficulty in interpreting MED metrics as an indication of a functional system. It also indicates superior performance of the radome for producing coherent target images.

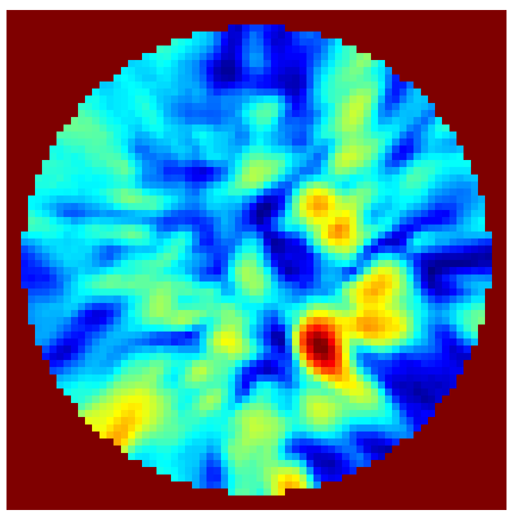

Fig. 5.10 DMAS image created using the clinical radome configuration. Cross-sectional view at a depth of 4.6 cm where the tumor is present.

To gain insight into the imaging performance, an antenna-wise partial DMAS imaging algorithm was developed. Each point in the DMAS image is formed by a delay corresponding to the distance, and a summation across each channel. Therefore, each antenna can be evaluated by measuring only channels involved in its contribution to the final DMAS result. This lets us discern which antennas contribute to good quality (i.e. high SCR) DMAS images.

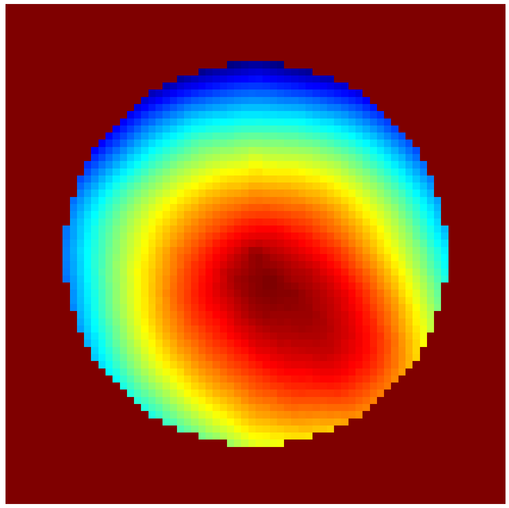

Fig. 5.11 DMAS image created using the flexible board configuration. Cross-sectional view at a depth of 4.6 cm where the tumor is present.

Further, it can identify channels and signal properties which cause undesirable clutter.

The partial DMAS imaging results for the radome and flexible board are shown in Figs. 5.12 and 5.13. The are nomalized to the maximum value in the overall set of partial images, and displayed in dB. For the radome, antennas 1, 2, 3, 10, and 11 produce strong response at the location of the tumor. We also observe some antenna are far do not contribute much to the image, and antenna 16 does not produce any useful imaging information. Repeating the partial DMAS imaging for the flexible board reveals that no individual antenna channel produces a delineated target. Unfortunately, this imaging technique doesn't help us localize the problem for the flexible board.

5.4 Discussion

There are many factors which may be causing the imaging problem. The imaging method uses known locations about antennas, and our assumptions about the antenna locations may be off by a few centimeters. Initial testing of the board didn't identify which channels

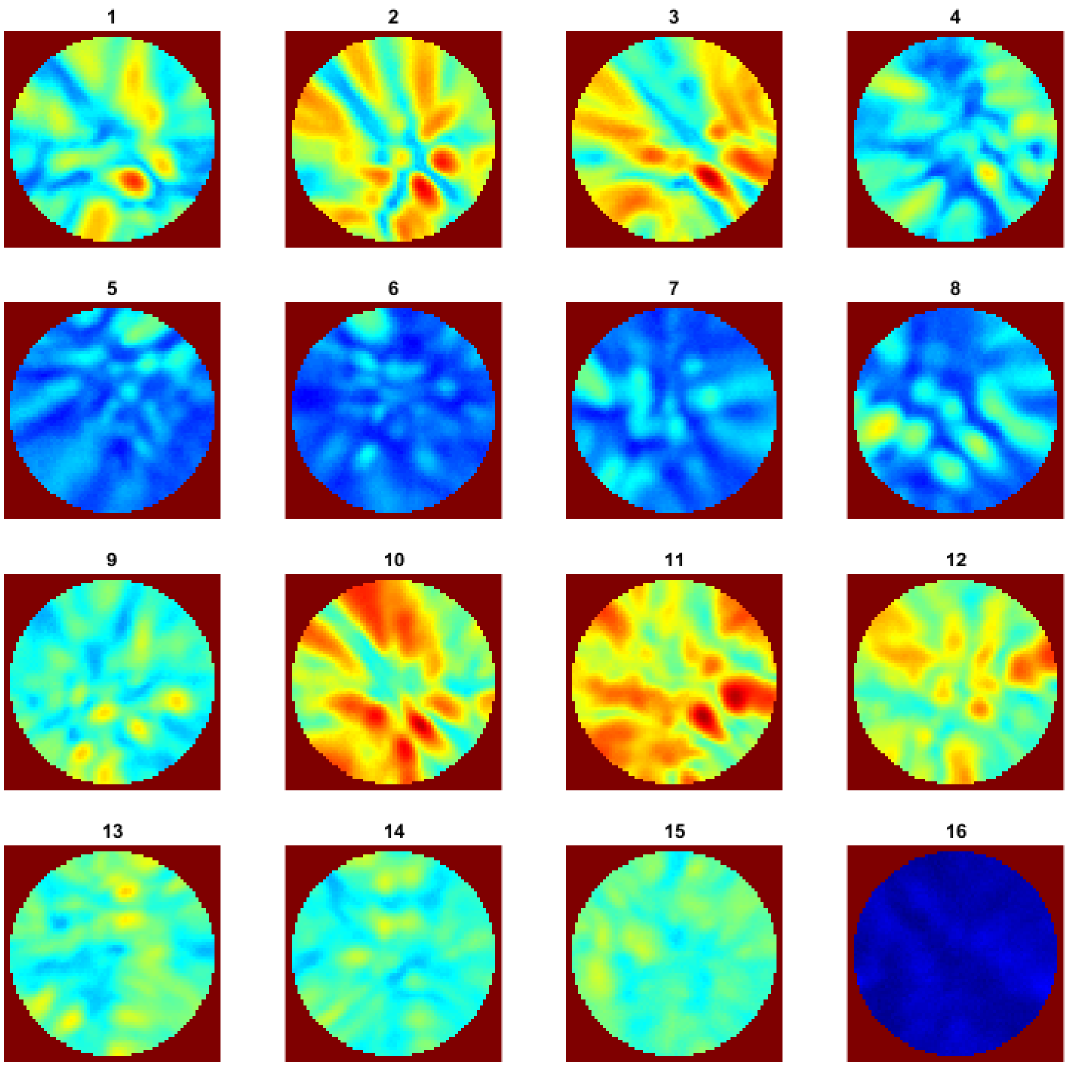

Fig. 5.12 Partial DMAS image for radome. Cross-sectional view at a depth of 4.6 cm where the tumor is present.

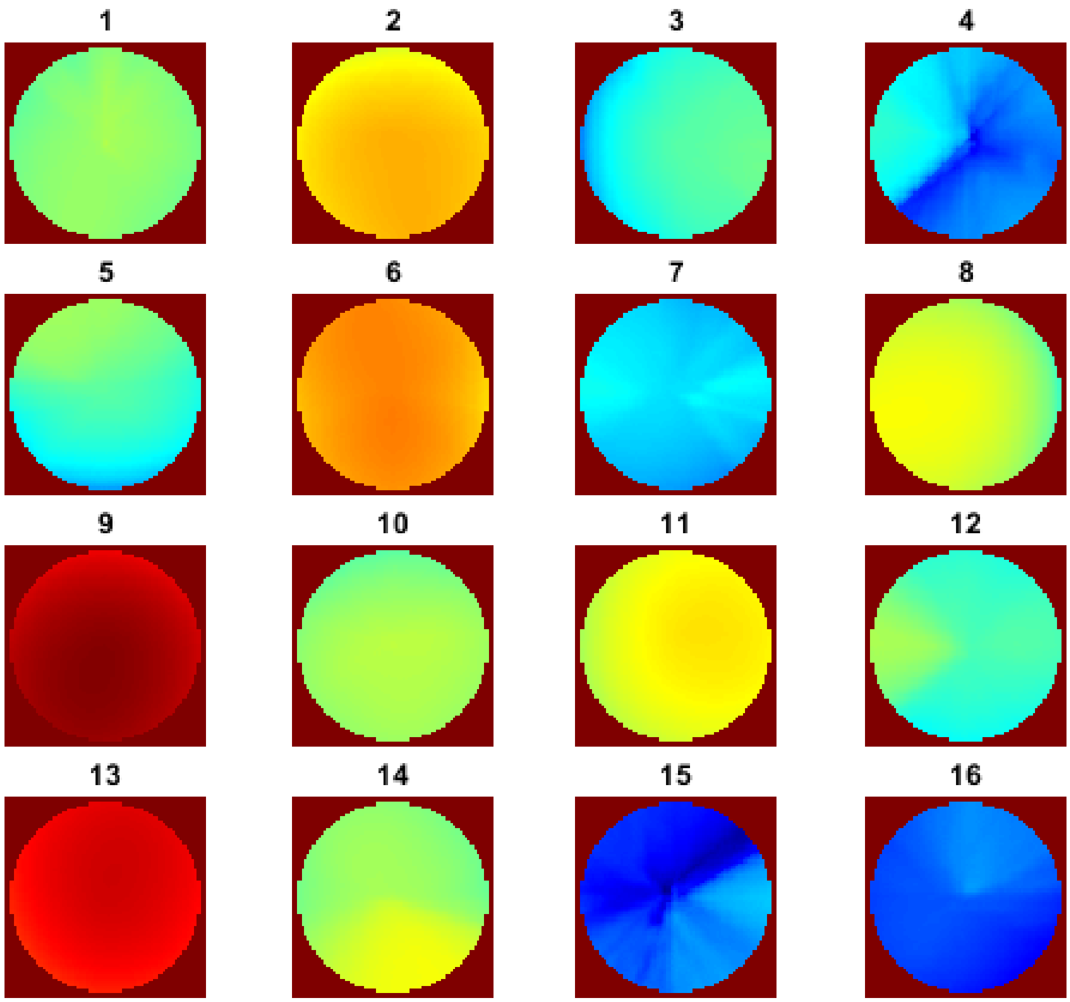

Fig. 5.13 Partial DMAS image for the flexible board. Cross-sectional view at a depth of 4.6 cm where the tumor is present.

were functional and which were problematic. It would be a better approach to assume all channels were non-functional and omit the defective ones early on. Crosstalk on the board is not removed, and varies between acquisitions. This is likely producing many artefacts during the decluttering process. There is also a variable time-delay between channels, with a worst-case distance between the shortest and longest trace being 5.4 cm. Using a velocity estimate of 18.8cm/ns on the manufactured Pyralux microstrips [2], we calculate a worst-case time-delay error of 288 ps. This time-error would translate to a localization error on the order of 3 cm in fat tissue with $\epsilon_r = 8.0$. It is also possible that traces became detached during acquisition or flexion of the board. Overall, only a subset of the 240 channels are functioning, perhaps intermittently, and need to be carefully characterized before imaging is viable.

Given the poor performance of the board, a number of suggestions for future improvements are presented here. First, LED indication should be used to allow a visual test of DC functionality. It is clear there is crosstalk in the board, but there is uncertainty as to where the cross talk is produced in the board. For this, I recommend a smaller scale study of crosstalk on microstrips implemented on the substrate, perhaps consisting of a 2x4 switching matrix implemented on the same material. The array configuration is highly symmetric, and this should be exploited in its testing in construction. General design-for-test practices could be applied, such as the introduction of test-traces to validate impedance matching and loss of transmission lines. Grounded coplanar waveguides (GCPW) have a lower tendency to emit crosstalk, and could be implemented instead of microstrip traces. The flexibility of the board is still low, due to the use of four layers rather than one layer where flexion is required. There are manufacturers who offer a rigid-flex PCB circuit, where portions of the board are flexible, while others are rigid. This could be investigated to allow flexion where needed.

5.5 Conclusion

The next-generation prototype implemented as an integrated solution on a flexible board did not perform as well as the rigid switching matrix. While the responses of reflections were successfully isolated, the combined channels were unable to beamform a target. A number of reasons are suspect, and would require a new iteration with better testability and characterization of traces.

Chapter 6

Conclusion

6.1 Conclusion and Future Work

This thesis has presented several new results and new directions for implementation of time domain microwave imaging system for breast cancer detection. The current system has relied on expensive scientific products, without PCB level consideration for implementation details of the transmission or receiving of UWB pulses. Many groups have reported systems using expensive VNAs, expensive time-domain test equipment, or custom integrated circuits on CMOS. The PCB or hybrid circuit design presents a number of unique low-cost designs. Further, new results of a flexible antenna array are presented. The following paragraphs present concluding remarks and future work for each system component.

Chapter 2 presented background for the time-domain breast cancer detection system as well as the electrical requirements. The system must support both transmitting and receiving UWB pulses in the range of 2-4 GHz. The detection and decluttering of tumors requires coherent system, where the phase of the received signal is consistent. The system uses a Minicircuits ZVE-3W-83+ power amplifier, which determines the power requirements of the

UWB pulse generator and shaper. Aiming for 6 GHz bandwidth was proposed to provide some design margin, especially in the receiver. Manufacturing of high-frequency components was discussed, with impedance-matched PCBs being the lowest cost option for operating at microwave wavelengths.

Chapter 3 reported measurements of step-recovery diodes and an MMIC based harmonic generator. The SRD impulse generator produced insufficient output power, while the FURAXA MMIC uses a high-cost integrated circuit. To improve this, a simpler single-SRD circuit, and a BJT-based impulse generator were designed. The BJT exhibits a step-recovery effect able to produce harmonics, offering an exceptionally low-cost pulse generator up to 6 GHz. Overall, these solutions offer a lower cost UWB pulse generator, on the order of the cost of an SRD or a BJT on an impedance-matched PCB. The remaining work is to finalize the realization of these pulse generators and evaluate if the suggested circuits meet the requirements for output harmonic power, phase-noise, and amplitude-noise. So far, the PCBs for SRD and BJT based impulse generators have been manufactured, based on previously reported designs. Measurement of jitter, amplitude and frequency content should be performed to validate these designs.

Chapter 4 considered receiving UWB pulses in the time-domain. Sampling into the GHz range has been historically accomplished through the use of Schottky diodes. Using Schottky diodes, implementations have reported bandwidths as high as 6 GHz implemented on FR-4 substrate. High-performance comparators have also been used to make high quality sampling analyzers, and are widely available at low cost. These approaches have been applied in other time-domain radar systems successfully, showing promising results. Of course, measurement of the designs are necessary, in order to evaluate real performance and proceed with careful implementation of the physical design.

Chapter 5 evaluates a flexible switching matrix with embedded antenna. The circuit is tested in simple tumor detection scenarios. The work demonstrates successful isolation of a tumor response signal. Further testing with the flexible circuit demonstrates inability to form images using beamforming. Overall the signals need significant correction before being applied for breast cancer detection. To accommodate this, a smaller design consisting of four transmit-receive channels (4x2 switching) is proposed for a future iteration. Due to the symmetry of the system, a full 16x2 matrix can be made by replicating a well-tested and functional (4x2), while reducing prototyping cost.

This work has presented a close look at the implementation details of an UWB radar system for breast cancer detection. The design of each sub-component here discussed presents unique challenges, and circuit parasitics are a concern at microwave frequency ranges. With the growing availability of low cost RF components and PCB fabrication the system can be designed at an exceptionally low cost. This work suggests that high performance can be obtained from PCB-based circuits, with further work needed in test and calibration.

References

[1] E. Zastrow, S. Davis, M. Lazebnik, F. Kelcz, B. Van Veen, and S. Hagness, "Development of anatomically realistic numerical breast phantoms with accurate dielectric properties for modeling microwave interactions with the human breast," *IEEE transactions on bio-medical engineering*, vol. 55, pp. 2792–800, 01 2009.

[2] D. M. Pozar, *Microwave engineering; 3rd ed.* Hoboken, NJ: Wiley, 2005.

[3] J. Coonrod, "Insertion loss comparisons of common high frequency PCB constructions," *IPC APEX EXPO Conference and Exhibition 2013, APEX EXPO 2013*, vol. 2, pp. 870–884, 01 2013.

[4] M. J. W. Rodwell, M. Kamegawa, R. Yu, M. Case, E. Carman, and K. S. Giboney, "GaAs nonlinear transmission lines for picosecond pulse generation and millimeter-wave sampling," *IEEE Transactions on Microwave Theory and Techniques*, vol. 39, pp. 1194–1204, July 1991.

[5] Hewlett-Packard, "Harmonic generation using step recovery diodes and SRD modules," Tech. Rep. AN920, Hewlett-Packard, 1984.

[6] T. Kikkawa, P. K. Saha, N. Sasaki, and K. Kimoto, "Gaussian monocycle pulse transmitter using 0.18 μm CMOS technology with on-chip integrated antennas for inter-chip UWB communication," *IEEE Journal of Solid-State Circuits*, vol. 43, pp. 1303–1312, May 2008.

[7] Y. Masui, A. Toya, M. Sugawara, T. Maeda, M. Ono, Y. Murasaka, A. Iwata, and T. Kikkawa, "Differential equivalent time sampling receiver for breast cancer detection," in *2017 IEEE Biomedical Circuits and Systems Conference (BioCAS)*, pp. 1–4, 2017.

[8] W. Kester and J. Bryant, "Section 3 - ADCs for DSP applications," in *Mixed-signal and DSP Design Techniques* (W. Kester, ed.), pp. 61 – 95, Burlington: Newnes, 2003.

[9] W. M. Grove, "Sampling for oscilloscopes and other RF systems: DC through X-Band," in *G-MTT International Symposium Digest*, vol. 66, pp. 191–196, May 1966.

[10] T.-G. Ma, C.-J. Wu, and C.-F. Chou, "An impulse-radio-based ultrawideband RF front-end module with a new multilayered microwave sampler," 2008.

[11] S. Hantscher, A. Reisenzahn, H. Kainmüller, and C. G. Diskus, "Hardware concepts for the sequential sampling of repetitive pulse radar echoes in cost-efficient ultra-wideband transceivers," *Microwave and Optical Technology Letters*, vol. 52, no. 3, pp. 585–591, 2010.

[12] O. B. Laug, D. I. Bergman, T. M. Souders, and B. C. Waltrip, "A next generation sampling comparator probe for the NIST sampling waveform analyzer," Tech. Rep. Technical Note 1496, NIST, 2008.

[13] American Cancer Society, "Facts Figures 2020." Available at https://www.cancer.org/content/dam/cancer-org/research/cancer-facts-and-statistics/annual-cancer-facts-and-figures/2020/cancer-facts-and-figures-2020.pdf, 2020.

[14] A. Karellas and S. Vedantham, "Breast cancer imaging: A perspective for the next decade," *Medical physics*, vol. 35, pp. 4878–97, 12 2008.

[15] M. Lazebnik, D. Popovic, L. McCartney, C. B. Watkins, M. J. Lindstrom, J. Harter, S. Sewall, T. Ogilvie, A. Magliocco, T. M. Breslin, W. Temple, D. Mew, J. H. Booske, M. Okoniewski, and S. C. Hagness, "A large-scale study of the ultrawideband microwave dielectric properties of normal, benign and malignant breast tissues obtained from cancer surgeries," *Physics in Medicine and Biology*, vol. 52, pp. 6093–6115, oct 2007.

[16] A. Santorelli, E. Porter, E. Kang, T. Piske, M. Popović, and J. D. Schwartz, "A time-domain microwave system for breast cancer detection using a flexible circuit board," *IEEE Transactions on Instrumentation and Measurement*, vol. 64, pp. 2986–2994, Nov 2015.

[17] N. Biller-Andorno and P. Juni, "Abolishing mammography screening programs a view from the Swiss Medical Board.," *Obstetrical and Gynecological Survey*, vol. 69, pp. 474–475, 08 2014.

[18] T. Barrett, "History of ultrawideband (UWB) communications radar," *Microwave Journal*, 2001.

[19] E. Porter, M. Coates, and M. Popović, "An early clinical study of time-domain microwave radar for breast health monitoring," *IEEE Transactions on Biomedical Engineering*, vol. 63, pp. 530–539, March 2016.

[20] X. Zeng, A. Fhager, P. Linner, M. Persson, and H. Zirath, "Experimental investigation of the accuracy of an ultrawideband time-domain microwave-tomographic system," *IEEE Transactions on Instrumentation and Measurement*, vol. 60, pp. 3939–3949, Dec 2011.

[21] H. Song, H. Kono, Y. Seo, A. Azhari, J. Somei, E. Suematsu, Y. Watarai, T. Ota, H. Watanabe, Y. Hiramatsu, A. Toya, X. Xiao, and T. Kikkawa, "A radar-based breast cancer detection system using CMOS integrated circuits," *IEEE Access*, vol. 3, pp. 2111–2121, 2015.

[22] A. Santorelli, M. Chudzik, E. Kirshin, E. Porter, A. Lujambio, I. Arnedo, M. Popovic, and J. Schwartz, "Experimental demonstration of pulse shaping for time-domain microwave breast imaging," *Progress In Electromagnetics Research*, vol. 133, pp. 309–329, 01 2013.

[23] H. Bahramiabarghouei, E. Porter, A. Santorelli, B. Gosselin, M. Popović, and L. A. Rusch, "Flexible 16 antenna array for microwave breast cancer detection," *IEEE Transactions on Biomedical Engineering*, vol. 62, pp. 2516–2525, Oct 2015.

[24] L. Kranold, P. Hazarika, and M. Popović, "Investigation of antenna array configurations for dispersive breast models," in *2017 11th European Conference on Antennas and Propagation (EUCAP)*, pp. 2737–2741, March 2017.

[25] G. Matrone, A. S. Savoia, G. Caliano, and G. Magenes, "The delay multiply and sum beamforming algorithm in ultrasound B-mode medical imaging," *IEEE Transactions on Medical Imaging*, vol. 34, no. 4, pp. 940–949, 2015.

[26] J. Garrett and E. Fear, "Stable and flexible materials to mimic the dielectric properties of human soft tissues," *IEEE Antennas and Wireless Propagation Letters*, vol. 13, pp. 599–602, 2014.

[27] K.-W. Yeom, *Microwave Circuit Design: A Practical Approach Using ADS.* USA: Prentice Hall Press, 1st ed., 2015.

[28] J. Ender, "Introduction to radar - Part I," *Ruhr-Universität Bochum*, 2011.

[29] M. Gerding, T. Musch, and B. Schiek, "Generation of short electric pulses based on bipolar transistors," *Advances in Radio Science - Kleinheubacher Berichte*, vol. 2, 01 2004.

[30] J. Han and C. Nguyen, "Coupled-slotline-hybrid sampling mixer integrated with step-recovery-diode pulse generator for uwb applications," *IEEE Transactions on Microwave Theory and Techniques*, vol. 53, pp. 1875–1882, June 2005.

[31] Z. Fu, H. Wang, and J. Huan, "Research on a ps fast edge generating method based on NLTL," *Jiliang Xuebao/Acta Metrologica Sinica*, vol. 32, pp. 539–543, 11 2011.

[32] Hewlett-Packard, "Pulse and waveform generation with step recovery diodes," Tech. Rep. AN918, Hewlett-Packard, 1984.

[33] A. Kamal, A. Bhattacharya, M. Tamrakar, and C. Roy, "Low-ringing and reduced-cost step recovery diode based UWB pulse generators for GPR applications," *Microwave and Optical Technology Letters*, vol. 56, 10 2014.

[34] G. Wong Choi, J. Joo Choi, and S. Hoon Han, "Note: Picosecond impulse generator driven by cascaded step recovery diode pulse shaping circuit," *Review of Scientific Instruments*, vol. 82, no. 1, p. 016106, 2011.

[35] Y. Masui, A. Toya, M. Sugawara, T. Maeda, M. Ono, Y. Murasaka, A. Iwata, and T. Kikkawa, "Gaussian monocycle pulse generator with calibration circuit for breast cancer detection," in *2018 IEEE Biomedical Circuits and Systems Conference (BioCAS)*, pp. 1–4, Oct 2018.

[36] M. Garbati, E. Perret, R. Siragusa, and C. Halopé, "Ultra-low-jitter fully tunable baseband pulse generator for UWB applications," *IEEE Transactions on Microwave Theory and Techniques*, vol. 66, pp. 420–430, Jan 2018.

[37] FURAXA, "Sampulse20x2 dual pulser/sampler demo board." Available at http://www.furaxa.com/Documents/SamPulse20x2_122715.pdf, 2015.

[38] K. El Hallaoui, A. Santorelli, M. Popović, and M. Coates, "Signal analysis and phantom experiments for a miniaturized time-domain microwave breast health monitoring device," in *2017 11th European Conference on Antennas and Propagation (EUCAP)*, pp. 1828–1832, 2017.

[39] D. Oloumi and E. Fear, "A picosecond pulse generator using SRD diodes: Design, analysis, and measurements," in *2018 USNC-URSI Radio Science Meeting (Joint with AP-S Symposium)*, pp. 159–160, 2018.

[40] J. R. Andrews, "Picosecond pulse generation techniques and pulser capabilities." Picosecond Pulse Labs Application Note AN-19, 2015.

[41] Texas Instruments, "420-MHz High-Speed Current-Feedback Amplifiers datasheet (Rev. H)." Available at https://www.ti.com/lit/gpn/ths3001, 2009.

[42] J. Merkelo and R. D. Hall, "Broad-band thin-film signal sampler," *IEEE Journal of Solid-State Circuits*, vol. 7, no. 1, pp. 50–54, 1972.

[43] E. Elkhouly, A. E. Fathy, and M. R. Mahfouz, "Signal detection and noise modeling of a 1-D pulse-based ultra-wideband ranging system and its accuracy assessment," *IEEE Transactions on Microwave Theory and Techniques*, vol. 63, pp. 1746–1757, May 2015.

[44] X. Zeng, A. Fhager, Z. He, M. Persson, P. Linner, and H. Zirath, "Development of a time domain microwave system for medical diagnostics," *IEEE Transactions on Instrumentation and Measurement*, vol. 63, no. 12, pp. 2931–2939, 2014.

[45] Analog Devices, “10 GHz latched comparator.” Available at https://www.analog.com/media/en/technical-documentation/data-sheets/hmc675lc3c.pdf, 2020.